CEFET/RJ
DIRETORIA DE PESQUISA E PÓS-GRADUAÇÃO

NUMERICAL AND EXPERIMENTAL ANALYSIS OF STRESS AND STRAIN CONCENTRATION IN PSEUDOELASTIC SHAPE MEMORY ALLOYS

Bruno Felippe Silva

Doctoral thesis presented to the Post-Graduation Program of Mechanical Engineering and Materials Technology, Centro Federal de Educação Tecnológica Celso Suckow da Fonseca, CEFET/RJ, as a requirement to obtain doctor degree in Mechanical Engineering and Materials Technology.

Advisor: Pedro Manuel Calas Lopes Pacheco, D.Sc.

Advisor: Ricardo Alexandre Amar de Aguiar, D.Sc.

Rio de Janeiro

December 2025

NUMERICAL AND EXPERIMENTAL ANALYSIS OF STRESS AND STRAIN CONCENTRATION IN PSEUDOELASTIC SHAPE MEMORY ALLOYS

Doctoral thesis presented to the Post-Graduation Program of Mechanical Engineering and Materials Technology, Centro Federal de Educação Tecnológica Celso Suckow da Fonseca, CEFET/RJ, as a requirement to obtain doctor degree in Mechanical Engineering and Materials Technology.

Bruno Felippe Silva

Examiners:

President, Professor Pedro Manuel Calas Lopes Pacheco, D. Sc. (CEFET/RJ)
(advisor)

Professor Ricardo Alexandre Amar de Aguiar, D. Sc. (CEFET/RJ)

(advisor)

Professor Luciana Loureiro da Silva Monteiro, D. Sc. (CEFET/RJ)

Professor Marcelo Amorim Savi, D. Sc. (COPPE/UFRJ)

Professor Aline Souza de Paula, D. Sc. (UnB)

Professor Carlos José de Araújo, Ph. D. (UFCG)

Rio de Janeiro

December 2025

Ficha catalográfica elaborada pela Biblioteca Central do CEFET/RJ

S586 Silva, Bruno Felippe
Numerical and experimental analysis of stress and strain concentration in pseudoelastic shape memory alloys / Bruno Felippe Silva. – 2025.
119f. il. (algumas color.) + apêndice ; enc.

Tese (Doutorado). Centro Federal de Educação Tecnológica Celso Suckow da Fonseca, 2025.
Bibliografia : f. 108-119.
Orientador: Pedro Manuel Calas Lopes Pacheco.
Coorientador: Ricardo Alexandre Amar de Aguiar.

1. Ligas com memória de forma. 2. Ligas – Propriedades termomecânicas. 3. Métodos dos elementos finitos. 4. Elasticidade. I. Pacheco, Pedro Manuel Calas Lopes (Orient.). II. Aguiar, Ricardo Alexandre Amar de (Coorient.). III. Título.

CDD 620.16

Elaborada pelo bibliotecário Leandro Mota de Menezes – CRB/7 nº 5281

Para a minha querida filha Camila, a quem dedico meus esforços e o meu coração.

ACKNOWLEDGEMENT

First, I would like to express my sincere gratitude to my family — Suelen Silva, Camila Silva, Sueli Regina Felippe, João de Deus Silva (*in memoriam*), Fábio Silva, and Antonietta Felippe (*in memoriam*) — for their unconditional love, constant support, and the life foundation that allowed me to reach this milestone.

I am deeply thankful to my advisors, Pedro Pacheco and Ricardo Aguiar, for their dedication and precise guidance, which were fundamental to the development of this work.

My sincere thanks to the Brazilian National Agency for Petroleum, Natural Gas and Biofuels (ANP), particularly the Superintendence of Infrastructure and Movement, for their support throughout this journey. I especially thank Priscila Raquel Kazmierczak, Caroline Morais, and Pedro Prudêncio for the many valuable exchanges during this period.

I also extend my appreciation to the team at CEFET/RJ, especially Professor Luiz Felipe Souza, as well as Brenno Duarte, Rogério Azevedo, Rodolpho da Hora and Hiron Magalhães, for their academic support and encouragement.

I sincerely thank the examination committee: professors Luciana Monteiro, Marcelo Savi, Aline de Paula and Carlos Araújo for the insightful contributions that enriched this work.

I am grateful to the Mecanon Laboratory at UFRJ, in particular to Vanderson Dornellas, for his technical assistance and collaboration.

Finally, I would like to thank CAPES for the financial support.

“Every failure is a step to success.”

William Whewell

ABSTRACT

NUMERICAL AND EXPERIMENTAL ANALYSIS OF STRESS AND STRAIN CONCENTRATION IN PSEUDOELASTIC SHAPE MEMORY ALLOYS

Shape memory alloys (SMA – Shape Memory Alloys) are materials that have a strong thermomechanical coupling associated with phase transformation processes. These alloys have special characteristics in terms of their stress-strain-temperature behavior, making them attractive for use in several applications of interest in engineering, such as actuators, intelligent structures and mechanical vibration absorbers. SMAs, when subjected to thermomechanical loads, present a complex non-linear behavior and require the use of specific tools and methodologies to assess their performance and integrity. The traditional design of mechanical components with complex geometries, involving geometric discontinuities such as notches and holes, has been treated through simplified mechanical design approaches involving stress concentration factors, both for monotonic and cyclic mechanical and/or thermal loadings. The presence of plastic strains increases the complexity of the analysis due to stress redistribution and non-linearities present, and mechanical design approaches involving elastoplastic stress concentration factors have also been used. Similarly, strains associated with the phase transformation process in shape memory alloys promote a stress field redistribution effect. This thesis aims to investigate, both experimentally and numerically, the stress concentration effect in pseudoelastic thin NiTi sheets, considering phase transformation and plasticity. Initially, the study includes training and heat treatment procedures established to stabilize and improve pseudoelastic behavior. Subsequently, Differential Scanning Calorimetry (DSC) analysis and standard ASTM E8 tensile tests are developed to characterize the pseudoelastic response and the coupling between stress-induced phase transformation and plastic deformation. In the next stage, thin NiTi plates containing holes of different diameters are tested to study the stress concentration effect. The strain fields around the holes are evaluated through the Digital Image Correlation (DIC) method, while temperature evolution is simultaneously monitored using infrared thermography, providing insight into the thermomechanical coupling mechanisms. A finite element numerical study is then developed and calibrated using the experimental data obtained from both the standard tensile specimens and the plates with holes. The results show good agreement between the simulations and experimental observations. Finally, a numerical study is performed to analyze stress and strain concentration under load levels considering different training and heat treatment conditions. DSC results revealed a clear dependence of phase transformation temperatures on heat treatment

parameters. Mechanical tests showed that the energy dissipation associated with the stabilized hysteresis loop observed for cyclic loadings could be quantified, with the highest value (5.8 MJ/m³) observed under the 530 °C/10-minute heat treatment combined with a 6.5% training strain. The influence of training and stabilized stress–strain response on K_σ is also analyzed using a finite element model considering phase transformation and plasticity. Numerical results show that the 6.5% strain training condition presents lower K_σ values at the end of loading compared to the 10% strain training condition. The proposed methodology provides a promising framework for studying stress concentration effects in pseudoelastic SMAs, contributing to the design of SMA-based components and to the broader understanding of their coupled thermomechanical behavior.

Keywords: Shape memory alloys, pseudoelasticity; Stress concentration factor; Finite element method

RESUMO

ANÁLISE NUMÉRICA E EXPERIMENTAL DA CONCENTRAÇÃO DE TENSÃO EM LIGAS COM MEMÓRIA DE FORMA PSEUDOELÁSTICAS

Ligas com memória de forma (SMA – Shape Memory Alloys) são materiais que apresentam um forte acoplamento termomecânico associado a processos de transformação de fase. Essas ligas possuem características especiais em relação ao comportamento tensão-deformação-temperatura, o que as torna atrativas para diversas aplicações de interesse na engenharia, como atuadores, estruturas inteligentes e absorvedores de vibrações mecânicas. Quando submetidas a carregamentos termomecânicos, as SMAs apresentam um comportamento não linear complexo, exigindo o uso de ferramentas e metodologias específicas para avaliar seu desempenho e integridade. O projeto tradicional de componentes mecânicos com geometrias complexas, envolvendo descontinuidades geométricas como entalhes e furos, tem sido tratado por meio de abordagens simplificadas de projeto mecânico que consideram fatores de concentração de tensão, tanto para carregamentos mecânicos e/ou térmicos monotônicos ou cíclicos. A presença de deformações plásticas aumenta a complexidade da análise devido à redistribuição de tensões e às não linearidades envolvidas, e abordagens de projeto que envolvem fatores de concentração de tensão elastoplásticos também têm sido utilizadas. De forma semelhante, deformações associadas ao processo de transformação de fase em ligas com memória de forma promovem um efeito de redistribuição do campo de tensões. Esta tese tem como objetivo investigar, experimental e numericamente, o efeito da concentração de tensões em chapas finas pseudoelásticas de NiTi, considerando a transformação de fase e a plasticidade. Inicialmente, o estudo inclui procedimentos de treinamento e tratamento térmico estabelecidos para estabilizar e melhorar o comportamento pseudoelástico. Em seguida, análises de Calorimetria de Varredura Diferencial (DSC) e ensaios de tração padrão ASTM E8 são realizados para caracterizar a resposta pseudoelástica e o acoplamento entre transformação de fase induzida por tensão e deformação plástica. Na etapa seguinte, chapas finas de NiTi contendo furos de diferentes diâmetros são ensaiadas para estudar o efeito da concentração de tensões. Os campos de deformação ao redor dos furos são avaliados por meio do método de Correlação Digital de Imagens (DIC), enquanto a evolução da temperatura é monitorada simultaneamente com o uso de termografia infravermelha, fornecendo informações sobre os mecanismos de

acoplamento termomecânico. Um estudo numérico por elementos finitos é então desenvolvido e calibrado com base nos dados experimentais obtidos tanto dos corpos de prova padrão quanto das chapas com furos. Os resultados mostram boa concordância entre as simulações e as observações experimentais. Por fim, é realizado um estudo numérico para analisar a concentração de tensões e deformações sob diferentes níveis de carregamento e condições de tratamento térmico. Os resultados de DSC revelaram uma clara dependência das temperaturas de transformação em relação aos parâmetros de tratamento térmico. Os ensaios mecânicos mostraram que a dissipação de energia associada ao ciclo de histerese estabilizado pôde ser quantificada, sendo o maior valor (5,8 MJ/m³) obtido para a condição de tratamento térmico a 530 °C por 10 minutos combinada com uma deformação de treinamento de 6,5%. A influência do treinamento mecânico e da resposta tensão–deformação estabilizada sobre o fator de concentração de tensões nominal K_σ também foi analisada. Os resultados indicam que, para a condição de treinamento com 6,5% de deformação, o caso que considera transformação de fase e plasticidade resulta em valores finais de K_σ inferiores aos observados para a condição de 10% de deformação. A metodologia proposta fornece uma estrutura promissora para o estudo dos efeitos de concentração de tensões em SMAs pseudoelásticos, contribuindo para o projeto de componentes baseados em SMA e para a compreensão mais ampla de seu comportamento termomecânico acoplado.

Palavras-chave: ligas com memória de forma, pseudoelasticidade; concentração de tensões; método dos elementos finitos

LIST OF FIGURES

Figure 1 - Actuation energy density (PHILLIPS, 2018) 23
Figure 2 – Schematics of crystal structures and microstructures in NiTi SMA (SHAW *et al.*, 2008) 24
Figure 3 - Schematic SMA Differential scanning calorimetry of SMA material (LAGOUDAS, 2008). 25
Figure 4- Typical stress-strain-temperature relationship of a shape memory alloy (LECCE, 2015) 26
Figure 5– Typical pseudoelastic effect of a shape memory alloy (LECCE, 2015) 26
Figure 6– Cyclic loading (training) (LAGOUDAS, 2008) 27
Figure 7– Cyclic pseudoelastic effect of a shape memory alloy. (a) experimental, (b) numerical (LECCE, 2015) 28
Figure 8- Effect of thermomechanical coupling at different loading rates (ARMATTOE, 2014) 29
Figure 9- Temperature x deformation curves at different loading rates (ARMATTOE, 2014) 29
Figure 10 -Domain front of the Lüders bands of the stress-induced austenite - martensite phase transformation (HE, 2023) 30
Figure 11 - Experimental and numerical stress-strain response and axial strain contours obtained (XIAO, JIANG, 2020) 32
Figure 12- Cyclic loading of a SMA wire where the functional fatigue affects the behavior of stress strain curve (DORNELAS, 2021a) 33
Figure 13 - ε x N_f curves, (a) equivalent strain x number of cycles, (b) equivalent transformation strain x number of cycles (CISSÉ *et al.,* 2016) 34
Figure 14 – Evolution of internal damage in a notched plate over 5 actuation cycles (PHILLIPS, 2018) 35
Figure 15 – Description of the regions at the crack tip and the stress–strain curve (SGAMBITERRA *et al.*, 2021) 36
Figure 16- Schematic representation of the phase diagram with material properties (adapted from LAGOUDAS, 2008) 38
Figure 17- Schematic representation of differential scanning calorimetry (DSC) for SMAs (LECCE, 2015) 39
Figure 18 – Electromechanical system Instron 5985. Specimen assembly 40
Figure 19 - DIC measurement setup (SUTTON *et al.*, 2009) 41
Figure 20 - Specimen with detail of speckle pattern (LOUCHE *et al*., 2012) 41
Figure 21 - Illustration of a reference subset before and after deformation (BÁRNIK *et al*., 2020) 42
Figure 22 - Temperature measurement by thermography (PIECZYSKA *et al.*, 2012) 44
Figure 23 – Experimental stress and temperature evolution as a function of strain for a pseudoelastic plate (PIECZYSKA et al., 2012) 45
Figure 24 - Samples before and after test and temperature fields (GU *et al*., 2020) 46
Figure 25 - Experimental setup scheme of the combined DIC and IR measurements (ZHANG *et al*., 2022) 47
Figure 26- Elastoplastic stress and strain concentration factors (GONZÁLES, 2014) 49
Figure 27- Martensite volume fraction in a plate with a hole at different temperatures (ARMATTOE, 2014). 51
Figure 28- Distribution of the martensite volume fraction under three softening conditions (PHILLIPS, 2018) 51

Figure 29- SMA plate with a hole: (a) stress distribution and (b) martensite fraction (XU *et al.*, 2021). 52
Figure 30 – Comparison of the TRIP strain distribution over different cycles: (a) numerical results and (b) experimental results (XU *et al.*, 2021). 53
Figure 31 – DSC sample preparation: (a) cutting machine, (b) DSC specimen (circled in red), (c) part weighting and, (d) DSC equipment. 56
Figure 32 - DSC test results: (a) As Received (AR) 56
Figure 33 - Tensile test with dimensions: (a) specimen (b) drawing with dimensions in millimeters (c) assembly on the test machine 57
Figure 34 – ASTM 2516 test result for a specimen in an AR condition 58
Figure 35 – Stress-strain curve - As Received specimen 58
Figure 36 - Temperature-controlled furnace 59
Figure 37 - DSC test results for different heat treatments: (a) 100 °C, (b) 400°C, (c) 500°C, (d) 600°C and (e) 950°C 61
Figure 38 – Dependence of transformation temperatures on the heat treatment temperature 62
Figure 39 – DSC test result for 530°C with 10 minutes of soaking time 63
Figure 40 - Specimen mounted in the test machine. 63
Figure 41 – Tensile test results: (a) 500°C – 7%, (b) 500°C – 10%, (c) 600°C – 8%, (d) 600°C – 10%, (e) 530°C – 4%, (f) 530°C – 6,5% and (g) 530°C – 10% 66
Figure 42 – TRIP results for different conditions (600°C – 10%, 600°C – 8%, 500°C – 10%, 500°C – 7%, 530°C – 10%, 530°C – 6,5% and 530°C – 4%) 68
Figure 43 – Comparison of tensile results for the stabilized hysteretic loop. for different conditions (600°C – 10%, 600°C – 8%, 500°C – 10%, 500°C – 7%, 530°C – 10%, 530°C – 6,5% and 530°C – 4%) 68
Figure 44 – Hysteretic dissipation energy for different heat treatment and training conditions for different conditions (600°C – 10%, 600°C – 8%, 500°C – 10%, 500°C – 7%, 530°C – 10%, 530°C – 6,5% and 530°C – 4%) 69
Figure 45 - Stress-strain curve: (a) 6.5% training, (b) 10% training of standardized (ASTM E8) specimens after heat treatment 70
Figure 46 – ASTM 2516 test result for a specimen in the improved condition (heat treated at 530°C for 10 minutes and trained with 6,5% strain) 71
Figure 47 – Tensile test using the DIC technique: a) specimen mounted in the test machine, b) specimen with speckle 72
Figure 48 – Stress-strain curve of a specimen heat treated at 530°C for 10 minutes and 6.5% strain training. DIC results show axial strain associated with phase transformation at different stages 73
Figure 49 - Dimensions of specimens: a) D6 mm, b) D9 mm, c) D12 mm 73
Figure 50 - Cyclic Stress-Strain Curves for the plates with hole diameters of: (a) 6mm, (b) 9mm, (c) 12mm 74
Figure 51 - Tensile test – experimental setup 75
Figure 52 – a) Specimen speckle surface, plates with hole diameters: 6mm, 9mm, 12mm b) black surface of 6mm specimen painted in black 75
Figure 53 – Experimental axial strain for plates with hole diameters: (a) 6mm, (b) 9mm, (c) 12mm 76
Figure 54 – Cyclic temperature variation in different specimen regions 77
Figure 55 – Temperature at the end of the loading for plates with hole diameters: (a) 6mm, (b) 9mm, (c) 12mm 78
Figure 56 – Temperature evolution at two points: near the hole (point A) and far from the hole (pint B). Plates with hole diameters: (a) 6mm, (b) 9mm, (c) 12mm 79
Figure 57 - Typical stress-strain curve of the Auricchio constitutive model (ABAQUS,

2018) 81
Figure 58 - Typical critical stress-temperature curve of SMAs (ABAQUS, 2018) 83
Figure 59 - FEM model with mesh, axial displacement prescribed load and boundary conditions 84
Figure 60 - Comparison between the stress-strain curves obtained from the numerical model and the experimental data: (a) 6.5% training, (b) 10% training of standardized specimens after heat treatment 85
Figure 61 – FEM model with: (*a*) symmetry, boundary conditions and loading, and (*b*) meshes for three hole diameters analyzed 86
Figure 62 – Experimental and FEM axial force x displacement curves, plates with hole diameters: (a) 6mm, (b) 9mm, (c) 12mm 87
Figure 63 –Axial strain results obtained by the FEM model (left column) and experimental analysis (right column) for plates with hole diameters: (a) 6mm, (b) 9mm, (c) 12mm 89
Figure 64 - Mesh of the FEM model for different diameters: (a) 3mm, (b) 6mm, (c) 9mm, (d) 12mm considering a quarter geometry symmetry 91
Figure 65 - Axial stress-strain curves for the local of maximum stress for plates with different hole diameters: (a) 6.5% training, (b) 10% training 91
Figure 66 - Axial nominal stress-strain curves for plates with different hole diameters: (a) 6.5% training, (b) 10% training. 92
Figure 67 - Axial stress distribution (in MPa) for plates with different hole diameters at the end of the loading stage: 6.5% training (a-d) and 10% (e-h). 93
Figure 68 - Martensite volume fraction distribution for plates with different hole diameters at the end of the loading stage: 6.5% training (a-d) and 10% (e-h). 94
Figure 69 - Axial total strain distribution for different diameters at the end of the loading stage: 6.5% training (a-d) and 10% (e-h). 95
Figure 70 - Stress-strain curves at region of maximum axial stress: case with phase transformation (TR) and case with phase transformation and plasticity (TR+PL) for plates with 9mm hole diameter and 10% strain training 96
Figure 71 - Axial strain distribution at the end of the loading stage for plates with different hole diameters: (a) total, (b) elastic, (c) phase transformation, (d) plastic 97
Figure 72 - Time evolution of the axial stress result (S22), martensite volume fraction (MVF) and the axial plastic strain (PE22) during loading stage at the edge of the hole (diameter of 9mm with 10% training strain) 97
Figure 73 - Evolution of the stress concentration factor during loading for plates with different hole diameters: (a) 6.5% training, (b) 10% training 99
Figure 74 – Stress, strain and Neuber concentration factors for 6.5% training: a) D3 mm b) D6mm, c) D9mm, d) D12mm 102
Figure 75 – Stress, strain and Neuber concentration factors for 10% training: a) D3 mm b) D6mm, c) D9mm, d) D12mm 103

LIST OF TABLES

Table 1 – Temperatures and furnace times for heat treatment.....60
Table 2 – Evolution of transformation temperatures according to heat treatment temperature.....62
Table 3 – Temperature heat treatment and training strain of the specimens.....64
Table 4 - Parameters of the phase transformation constitutive model.....85
Table 5 - Parameters of the plasticity model 85

LIST OF SYMBOLS

A - Austenite

A_f - Final temperature of austenite formation at zero stress

A_s - Initial temperature of austenite formation at zero stress

C^A - Slope of austenite transformation lines in the stress–temperature plane

C^M - Slope of martensite transformation lines in the stress–temperature plane

E, E_A, E_M - Young's modulus (overall, austenitic and martensitic phases)

$\boldsymbol{F^{tr}}$ - Transformation surface

$\boldsymbol{G^{tr}}$ - Potential for flow transformation

K_t - Stress concentration factor according to Neuber

K_ε - Strain concentration factor

K_σ - Stress concentration factor under nominal stress

M^d - Maximum temperature at which austenite can be transformed into martensite by stress,

M_s - Initial temperature of martensite formation for a stress-free state

M_f - Final temperature of martensite formation for a stress-free state

M^t – Twinned martensite formation temperature

N_f - Number of cycles to failure

$\boldsymbol{p}$ – Hydrostatic pressure

$\boldsymbol{q}$ – Equivalent von Mises stress

T – Absolute temperature

$\boldsymbol{\varepsilon}$ – Total strain tensor

$\boldsymbol{\varepsilon^{el}}$ – Elastic strain

$\boldsymbol{\varepsilon^{pl}}$ – Elastic strain

$\boldsymbol{\varepsilon^{tr}}$ – Phase transformation strain

$\boldsymbol{\varepsilon_n}$ - Nominal strain.

$\boldsymbol{\sigma_n}$ - Nominal stress

$\boldsymbol{\varepsilon_{ij}}$ – Strain tensor components

ν, ν_A, ν_M – Poisson's ratio (overall, austenite, and martensite)

$\boldsymbol{\sigma}$ – Cauchy stress tensor

σ^{Ms} – Initial critical stress for martensite transformation,

σ^{Mf} – Final critical stress for martensite transformation,

σ^{As} - Initial critical stress for transformation into austenite,

σ^{Af} - Final critical stress for transformation into austenite

σ_s – Start stress for the detwinning of martensite

σ_f - Finishing stress for the detwinning of martensite

ς – Martensite volume fraction

Symbols:

Δ - Variation

$\dot{(\ )}$ - Derivative

TABLE OF CONTENTS

1. INTRODUCTION 19

1.1.Objectives 20

1.1.1.General objective 20

1.1.2.Specific objectives 21

1.1.3.Methodology 21

1.2.Structure of the thesis 22

2. LITERATURE REVIEW 23

2.1.Shape memory alloys 23

2.1.1.Shape memory effect 25

2.1.2.Pseudoelasticity 26

2.1.3.Two -way shape memory effect - TWSME 27

2.1.4.Thermomechanical coupling 28

2.1.5.Lüders type transformation 30

2.1.6.Fatigue 32

2.1.7.Damage 34

2.1.8.Fracture Mechanics 35

2.2.Experimental methods for SMA characterization 36

2.2.1.Differential scanning calorimetry 38

2.2.2.Tensile tests 39

2.2.2.1.Digital Image Correlation (DIC) 40

2.2.2.2.Thermography 44

2.3.Stress concentration 47

2.3.1.Studies on stress concentration in shape memory alloys 50

2.3.1.1.Shape memory effect 50

2.3.1.2.Pseudoelasticity 53

3. EXPERIMENTAL PROCEDURES 55

3.1.Material characterization – As received condition 55

3.2.Heat treatment and training analysis 59

3.2.1.Differential Scanning Calorimetry (DSC) tests 60

3.2.2.Training process 63

3.2.2.1.Digital Image Correlation 71

3.3.Tensile tests – plates with holes 73

3.3.1.Training 74

3.3.2.Digital image correlation and thermography 74

4. NUMERICAL PROCEDURE 80

4.1.Constitutive model (Auricchio).....80
4.2.Model calibration – ASTM E8 specimen.....84
4.3.Finite element model verification – Plates with holes.....86
5. FINITE ELEMENT ANALYSIS OF PLATES WITH HOLES.....90
5.1.Numerical analysis plates with holes.....90
5.2.Stress concentration factor.....98
6. CONCLUSION AND SUGGESTIONS FOR FUTURE WORKS.....104
6.1.Conclusion.....104
6.2.Suggestions for future works.....106
REFERENCES.....108
APPENDIX 1 – LIST OF PUBLICATIONS.....120

1. INTRODUCTION

Smart or intelligent materials are a class of materials that have attracted considerable attention in recent years due to their special capabilities that differentiate them from materials commonly used in engineering. This class of materials exhibits strong coupling between fields, such as mechanical, thermal, electrical, and magnetic fields, allowing them to alter their properties, such as shape, color, and viscosity, when subjected to external stimuli (YILDIRIM, CANDAN, 2023; CHEN *et al.*, 2024).

Shape Memory Alloys (SMAs) belong to the class of smart materials which presents a thermomechanical coupling where the application of mechanical or thermal stimulus can promote large recoverable displacements and/or loads. At the material level, this behavior originates from reversible solid-state martensitic phase transformations, giving rise to several phenomena, such as pseudoelasticity, one-way and two-way shape memory effects, and temperature-driven phase changes (LAGOUDAS, 2008; JADHAV *et al., 2025*). In addition, to nickel and titanium alloys (NiTi), there are those based on copper (CuZnAl and CuAlNi), iron (FePt, FePd), gold (Aucd, AuCuZn), among others according to Lecce (2015). In this study, NiTi alloys will be analyzed.

SMAs applications have grown over the last few decades, and these materials has proven to be extremely versatile. Studies show that these materials have been increasingly used in the aerospace, biomedical, oil and gas, and construction industries, among others, as described in KARAKOC *et al.*, (2021)*,* MATUSZEWSKI, (2020), MOTZKI, SEELECKE (2019), PATIL, SONG (2017) and JADHAV *et al.,* (2025).

Due to their complex behavior, the design of SMA mechanical components presents several challenges, requiring the use of special methodologies that allow for their proper operational functioning while preventing structural failures. Geometric discontinuities produce stress concentrators that can result in high stress values in the mechanical part, making it important to have design methodologies capable of estimating them. The study of stress concentration in notched components is an important factor for the design of parts in relation to functional and structural fatigue. Therefore, methodology for calculating stress concentration factors is important for the dimensioning of SMA components.

The growing adoption of Additive Manufacturing (AM) (AHMED *et al.,* 2026) has further expanded the application space of SMAs by enabling complex geometries that are unattainable through conventional fabrication processes. In the case of NiTi-based SMAs, AM is particularly attractive because functional behavior is highly sensitive to composition, defects, and texture. As

a result, AM is increasingly viewed not merely as a shaping technology, but as a coupled process–microstructure–property design tool (AHMAD *et al*., 2024). However, the advantages of AM come at the cost of design complexity in special due to stress concentration phenomena. Current research still lacks validated frameworks capable of integrating manufacturing parameters, microstructural features, phase transformation, stress concentration, and fatigue into a unified predictive methodology (AHMAD *et al*., 2024; RANGASWAMY *et al*., 2025).

Within the current state of the art on shape memory alloys, this thesis positions itself at the intersection of advanced experimental characterization and numerical modeling of stress and strain concentration. While previous studies have addressed SMA thermomechanical behavior or stress concentration in isolation, the present work builds upon and extends an integrated experimental–numerical framework in which thermomechanical characterization, full-field measurements, and finite element modeling are combined in a unified methodology. In particular, it follows and advances a workflow comprising: (i) SMA characterization, including transformation temperatures and stabilized cyclic response; (ii) full-field experimental mapping of strain and temperature fields near geometric discontinuities; (iii) development of numerical models based on finite element method; (iv) calibration and validation of finite element models using experimental measurements; and (v) analysis of stress concentration factors obtained using the developed numerical models (Silva *et al.,* 2025a,b).

1.1. Objectives

This section describes the objectives of the thesis. Initially, the general objective is defined followed by the specific objectives, finally a description of the methodology followed in this thesis is presented.

1.1.1. General objective

This thesis aims to investigate the stress and strain concentration phenomena in pseudoelastic shape memory alloy (SMA) thin sheets through experimental measurements and

numerical simulations, with emphasis on the effects of geometric discontinuities and loading history.

1.1.2. Specific objectives

In order to achieve the general objective, the following specific objectives have been defined:

- Experimental investigation of the stress and strain fields near notches or stress concentrators in pseudoelastic NiTi thin sheets under uniaxial cyclic loading, using Digital Image Correlation (DIC) and thermography.
- Development of finite element models capable of capturing pseudoelastic and plastic behaviors as well as local stress concentrations, by implementing an appropriate constitutive model in a commercial solver.
- Correlation of the experimentally measured strain fields with numerical predictions, with particular attention to the evolution of strain localization and transformation fronts near geometric discontinuities.
- Evaluation of the influence of specimen geometry on stress amplification and the development of martensitic transformation zones.

1.1.3. Methodology

To achieve objectives, experimental and numerical techniques were used. Initially, an experimental characterization of a plate in an as-received condition is performed, which indicated the need for a study of heat treatment and mechanical training in order to establish a maximum dissipation energy condition associated to the hysteresis loop, condition desired for vibration damping applications using pseudoelastic materials. Subsequently, an experimental study of plates with holes was performed using Digital Image Correlation (DIC) and thermography techniques. Next, a numerical model is created and calibrated with experimental data and the parameters were used in a model that present stress concentration to compare numerical and

experimental results. Finally, an in-depth analysis of stress-strain concentration factors is developed.

During the development of this thesis, several articles were published in academic journals and conferences proceedings to present and discuss the methodology and results with the peers. The list of publications can be found in Appendix 1.

1.2. Structure of the thesis

This thesis is structured with different approaches aiming to test and model the influence of geometric discontinuities in pseudoelastic thin sheets. This first chapter introduces the theme and presents the thesis structure.

The second chapter contains a bibliography review about the themes related to the covered topics, such as shape memory alloys, stress concentration, experimental methods such as Digital Image Correlation (DIC) and thermography, and numerical methods.

The third chapter presents the experimental studies developed including heat treatments and training processes for stabilization, and mechanical tests of plates with holes using Digital Image Correlation (DIC) and thermography techniques

In the fourth chapter, the numerical procedures are presented. Firstly, the constitutive model is presented followed by the definition of the parameters used in the finite element model and its calibration related to experimental data. In the sequence, a comparison between finite element models of plates with holes and the experimental results is presented.

The fifth chapter is related to the study of numerical results of stress and strain in pseudoelastic thin sheets with holes considering phase transformation and plasticity and its influence on the stress concentration factor.

The sixth chapter contains the conclusions and suggestions for future work.

2. LITERATURE REVIEW

2.1. Shape memory alloys

This section describes general concepts about shape memory alloys and some important effects. Firstly, the main behaviors of shape memory effect, pseudoelasticity are presented followed by important effects such as two-way shape memory effect (TWSME), thermomechanical coupling, Lüders bands phase transformation, damage, fatigue and fracture mechanics.

Shape memory alloys (SMAs) are classified as multifunctional materials that exhibit additional functionalities such as actuation, sensing (LAGOUDAS, 2008). These materials are capable of converting non-mechanical stimuli (such as thermal, magnetic, or optical signals) into mechanical responses.

Among the various types of SMAs, the nickel–titanium (NiTi) alloy stands out due to its excellent mechanical performance, functional stability, and wide range of applications (LECCE, 2015). For this reason, NiTi is the focus of the present study.

SMA are materials with high actuation energy density when compared to other classes of material, as shown in Figure 1.

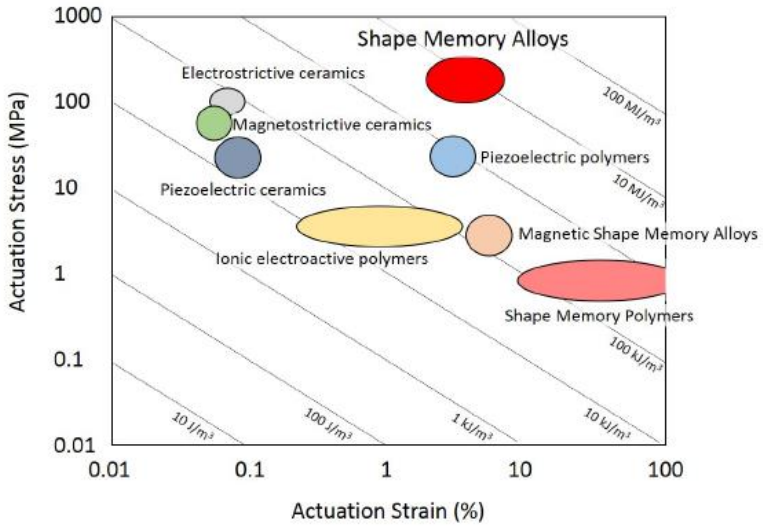


Figure 1 - Actuation energy density (PHILLIPS, 2018)

In addition to nickel and titanium alloys, there are those based on copper (CuZnAl and CuAlNi), iron (FePt, FePd), gold (Aucd, AuCuZn), among others according to LECCE (2015).

The unique properties of NiTi alloys arise from reversible martensitic phase transformations between two main phases: austenite, a high-temperature phase with a more ordered and stable cubic structure; and martensite, a low-temperature phase with a less ordered monoclinic structure (LAGOUDAS, 2008; OLIVEIRA *et al.,* 2016).

A schematic representation of the crystal structure and microstructures of the two main phases for NiTi are presented in Figure 2. Austenite has a cubic structure, and martensite has a monoclinic structure. Another intermediate phase that may be present is called the R phase, which is a rhombohedral distortion of the Austenitic structure (SHAW *et al., 2008*).

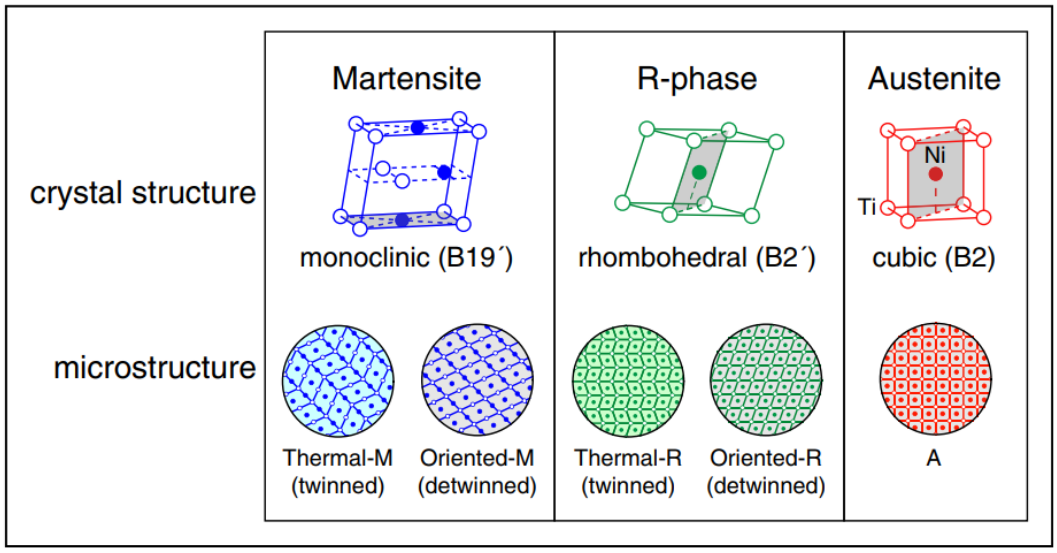


Figure 2 – Schematics of crystal structures and microstructures in NiTi SMA (SHAW *et al.*, 2008)

Phase transformation temperatures define the beginning and end of the forward and reverse phase transformations during thermal cycling. The martensite start temperature (M_s) marks the point at which austenite begins to transform into martensite upon cooling, while the martensite finish temperature (M_f) indicates when this transformation is complete and the material becomes fully martensitic. Upon heating, the reverse transformation begins at the austenite start temperature (A_s), where martensite starts reverting to austenite, and concludes at the austenite finish temperature (A_f), above which the alloy is fully austenitic. These phase transformation temperatures are critical for understanding the thermomechanical behavior of SMAs and are

typically determined through experimental techniques such as Differential Scanning Calorimetry (DSC) (SILVA *et al.,* 2019). A schematic DSC curve of SMA material is presented in Figure 3.

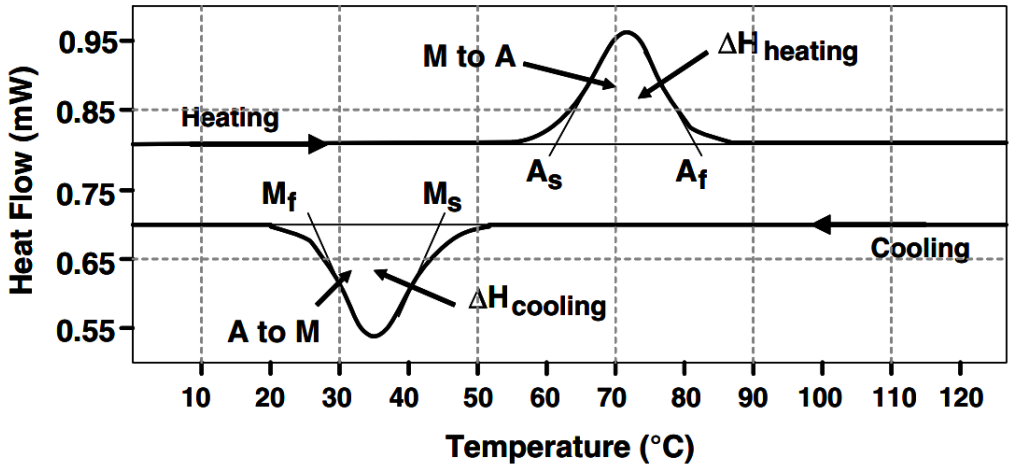


Figure 3 - Schematic SMA Differential scanning calorimetry of SMA material (LAGOUDAS, 2008).

While austenite is an ordered phase stable at high temperature in a stress-free state, the martensitic phase has two variants: twinned martensite, stable at low temperature in a stress-free state, and detwinned martensite, which occurs when the material is under stress. Depending on the work temperature the material can exhibit two main behaviors: shape memory effect or pseudoelasticity, which are discussed in the next two sections.

2.1.1. Shape memory effect

In the shape memory effect, the stable phase at low temperatures and free of stress is twinned martensite (Figure 4, point (1)). When mechanical loading is applied, the reorientation to detwinned martensite ((2) to (3)) begins, from the moment the phase is fully martensitic (4). When unloading, the material maintains a residual strain and remains as detwinned martensite (5). As the temperature increases, the phase changes to austenite, and the residual strain is recovered (6). When the part cools, the structure returns to twinned martensite (7), returning to the original condition (LAGOUDAS, 2008; ADEODATO *et al.,* 2025).

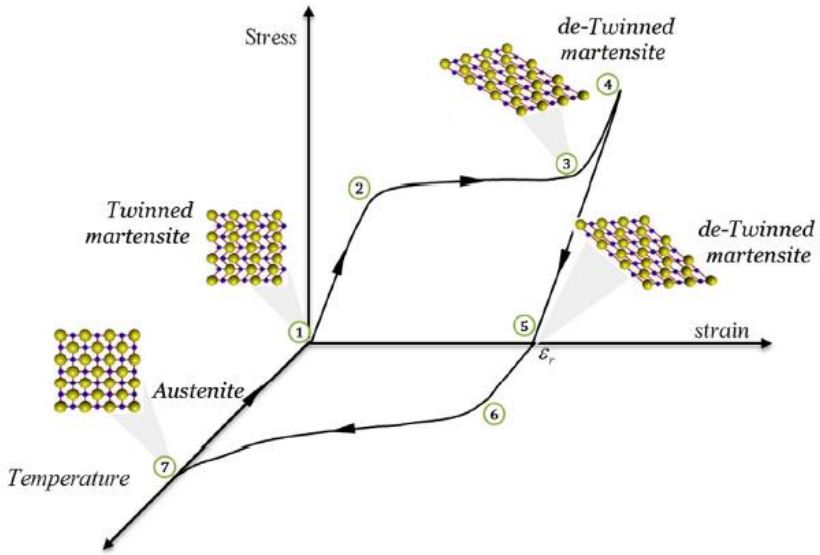


Figure 4- Typical stress-strain-temperature relationship of a shape memory alloy (LECCE, 2015)

2.1.2. Pseudoelasticity

Pseudoelastic behavior occurs at temperatures above the final austenite transformation temperature (A_f), which is the phase in the stress-free state (Figure 5, point (1)). When applying the load, the phase transformation to detwinned martensite occurs ((2), (3) and (4)), and upon unloading, the strain is completely reversed (5) and (6), as well as the return to the austenite phase (LAGOUDAS, 2008).

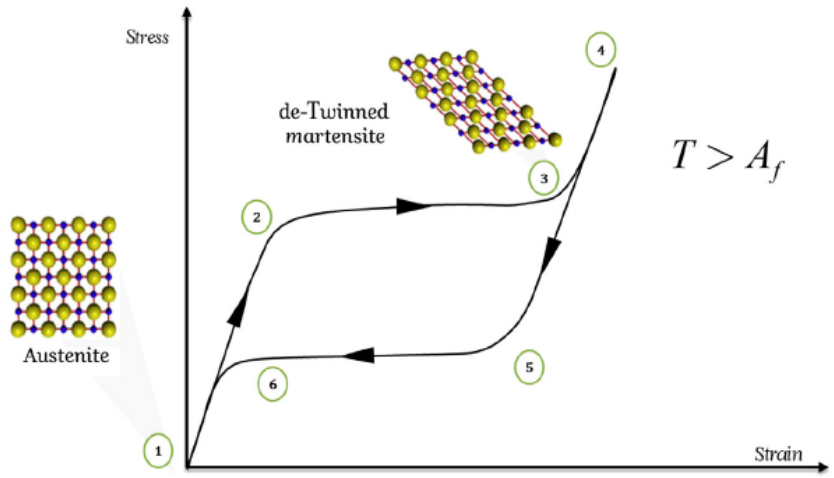


Figure 5– Typical pseudoelastic effect of a shape memory alloy (LECCE, 2015)

2.1.3. Two -way shape memory effect - TWSME

The reversible shape memory effect (two-way shape memory effect - TWSME) can be observed when a shape memory alloy receives repeated thermomechanical cycles (training) (KONG *et al.,* 2024; HONG *et al.,* 2024). The training process causes changes in the microstructure that lead to macrostructural changes in material behavior (LAGOUDAS, 2008). This phenomenon also involves the stabilization of the hysteresis loop (OLIVEIRA, DE PAULA, 2020; KAYA *et al.,* 2020). The representation of the training effect is presented in Figure 6.

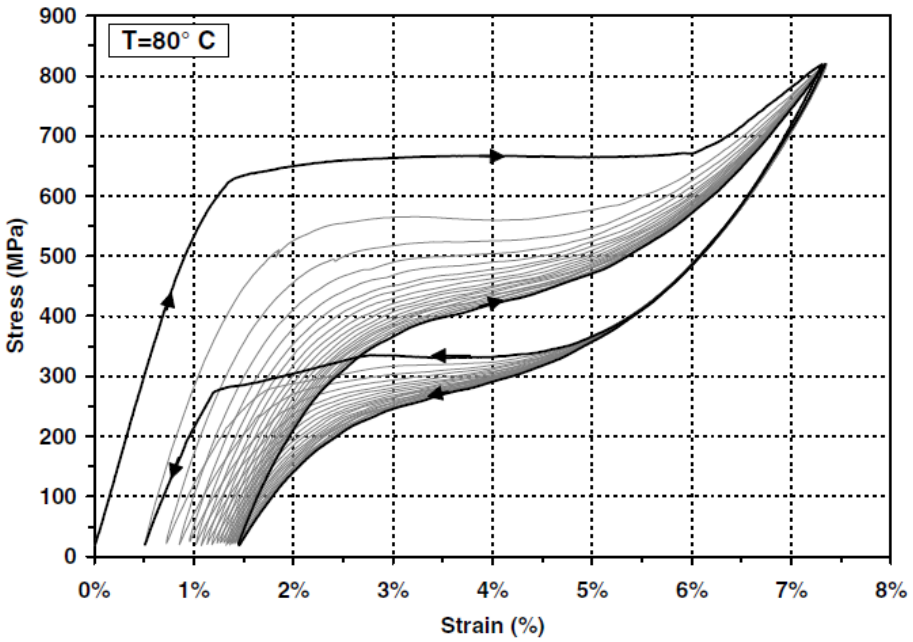


Figure 6– Cyclic loading (training) (LAGOUDAS, 2008)

Transformation-induced plastic strain (TRIP) is an important effect to be considered in the training stage and throughout the service life of the shape memory alloy where inelastic transformations occur during cyclic loading. This effect is responsible for residual stresses and strains and the origin of the TWSME effect that influences the reduction of the component's service life (CISSÉ *et al*., 2016; DORNELAS *et al*., 2021a; DUARTE, 2019; ARGÔLO, 2024; OLIVEIRA *et al.,* 2018). Figure 7 presents experimental and numerical results of the stress-strain curve of a pseudoelastic alloy subjected to cyclic loading, where the stabilization of the hysteresis loop promoted by TRIP is observed.

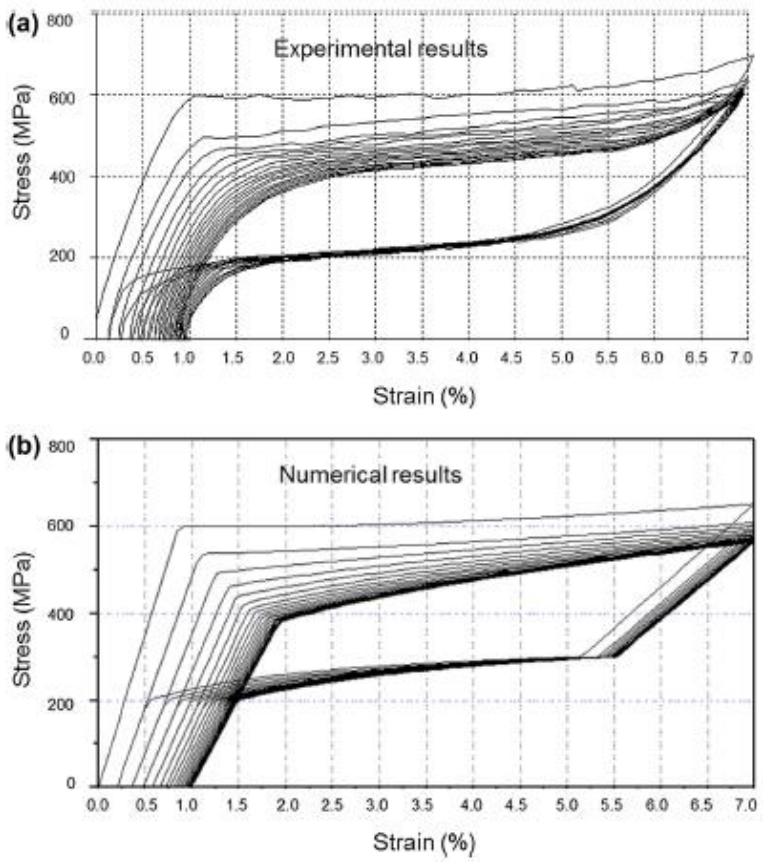


Figure 7– Cyclic pseudoelastic effect of a shape memory alloy. (a) experimental, (b) numerical (LECCE, 2015)

2.1.4. Thermomechanical coupling

Thermomechanical coupling is an important phenomenon in SMAs. Although the austenite-to-martensite transformation is a non-diffusive process, it is still influenced by the loading rate. In the austenite-martensite transformation, latent heat is released and is therefore exothermic, and the reverse transformation is, in turn, endothermic (CISSÉ *et al*., 2016), so, during the phase transformation process, latent heat promotes temperature variation (KUNDU, BANERJEE, 2022; REZAEE-HAJIDEHI *et al.,* 2025). Due to convection, loading rates affect how this heat is absorbed or released, thus impacting the phase transformation behavior, which depends on the critical transformation temperatures. At high loading rates there is not enough time for sufficient heat exchange by convection to occur to reduce the effects of temperature variation (MONTEIRO *et al.*, 2009).

Figure 8 shows the distribution of phase transformation and temperature at different loading rates in a thin pseudoelastic plate subjected to tensile loading at different loading rates (ARMATTOE, 2014). In the results presented, higher loading rates lead to higher temperatures and a larger transformed region. This is due to thermomechanical coupling, where at high strain rates, the effect of latent heat and local convection influence the martensitic transformation, which explains the temperature and phase transformation gradient in the specimens at higher rates. At higher loading rates, the temperature of the test specimen increases, as shown in Figure 8 and Figure 9 (ARMATTOE, 2014).

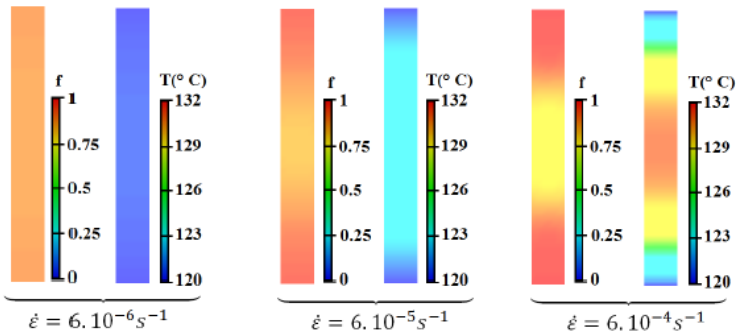


Figure 8- Effect of thermomechanical coupling at different loading rates (ARMATTOE, 2014)

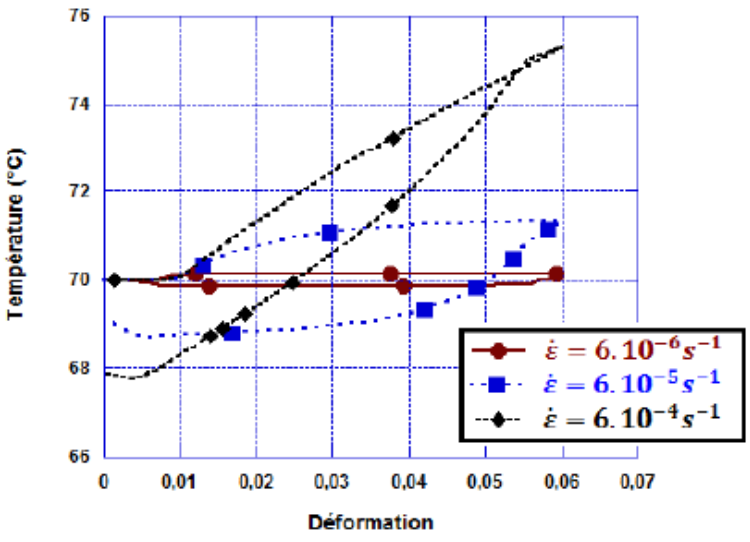


Figure 9- Temperature x deformation curves at different loading rates (ARMATTOE, 2014)

2.1.5. Lüders type transformation

The formation and propagation of Lüders-type bands during stress-induced martensitic transformation is one of the most distinctive phenomena in the pseudoelastic behavior of SMAs, particularly NiTi alloys (SHARIAT *et al.*, 2022, 2023; DI LEONARDO *et al.*, 2022). This localized deformation mode, first reported by MIYAZAKI *et al.* (1981), manifests as the nucleation and propagation of transformation fronts that divide regions of austenite and martensite (Figure 10), resulting in the characteristic stress plateaus observed during tensile tests. This phenomenon represents a macroscopic expression of the mechanical instability associated with the non-convexity of free energy during a first-order phase transformation (HE, 2023).

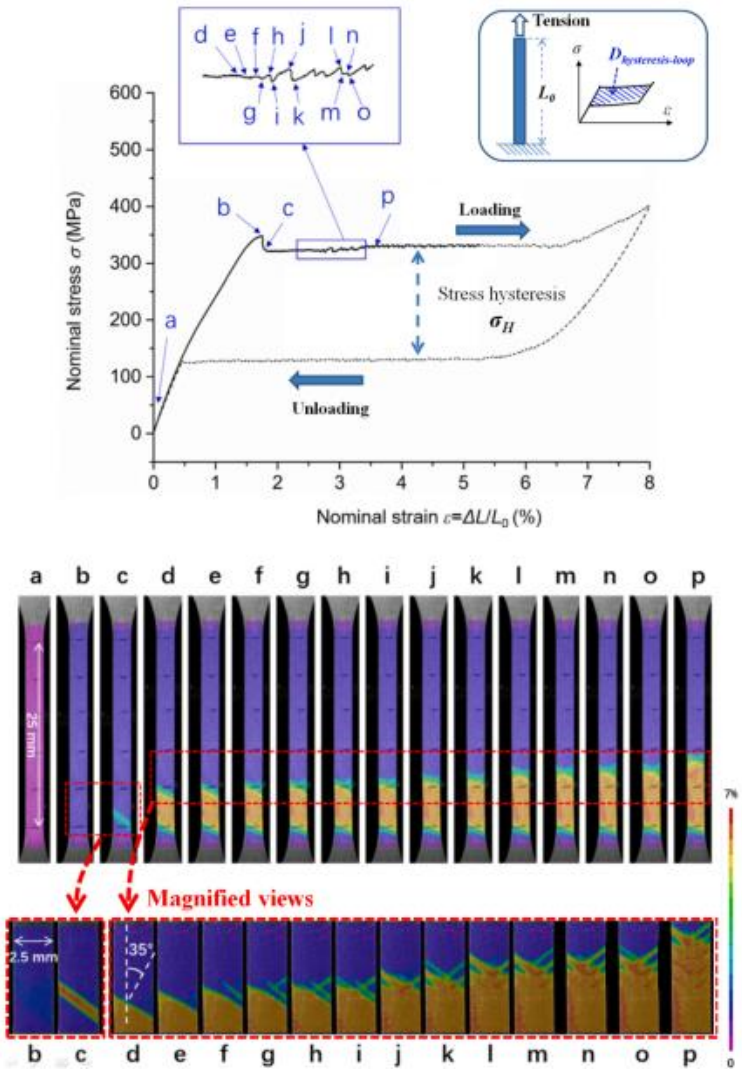


Figure 10 -Domain front of the Lüders bands of the stress-induced austenite - martensite phase transformation (HE, 2023)

Recent studies confirmed that Lüders-type deformation in NiTi occurs predominantly under tensile loading, not being observed under compression or shear (SITTNER *et al.,* 2005; SHARIAT *et al.*, 2022). Using Digital Image Correlation (DIC), the authors identified distinct stages in the evolution of Lüders bands (from nucleation to steady-state propagation) and showed that local strain rates within the bands are significantly higher than the global applied strain rate, revealing the dynamic nature of the transformation front. The inclination angle of these bands, typically between 48° and 67°, depends on specimen geometry and stress state, while the local strain jump between transformed and untransformed regions corresponds to a transformation strain of approximately 6–8 %.

Coupled DIC and infrared thermography (IRT) measurements have made it possible to simultaneously monitor strain and temperature fields during the martensitic transformation. ZHANG *et al.,* (2022) and NARGATTI, AHANKARI (2021), demonstrated that the interface between austenite and martensite is accompanied by localized temperature peaks associated with latent-heat release and transformation-induced plasticity (TRIP). The combination of full-field experimental techniques has therefore become essential to quantify local heterogeneities of stress and strain.

According to the review by DELPUEYO *et al.,* (2021), DIC provides spatial strain maps that reveal the nucleation and movement of transformation fronts, whereas IRT enables synchronous monitoring of heat release and absorption, identifying transformation kinetics, front velocity, and heat-transfer effects. These measurements are indispensable for calibrating and validating thermomechanical constitutive models.

From the modeling perspective, several constitutive frameworks have incorporated mechanical instability to reproduce transformation-band patterns. XIAO, JIANG (2020) developed a model based on the Helmholtz free energy that captures both cyclic degradation and non-homogeneous transformation in pseudoelastic NiTi (Figure 11). In parallel, nonlocal and phase-field models demonstrated that Lüders-type localization naturally emerges from the softening segment of the stress–strain curve. HE (2023) established a quantitative relation between hysteresis and interface energy, clarifying the energy dissipation mechanisms occurring during the propagation of phase transformation fronts.

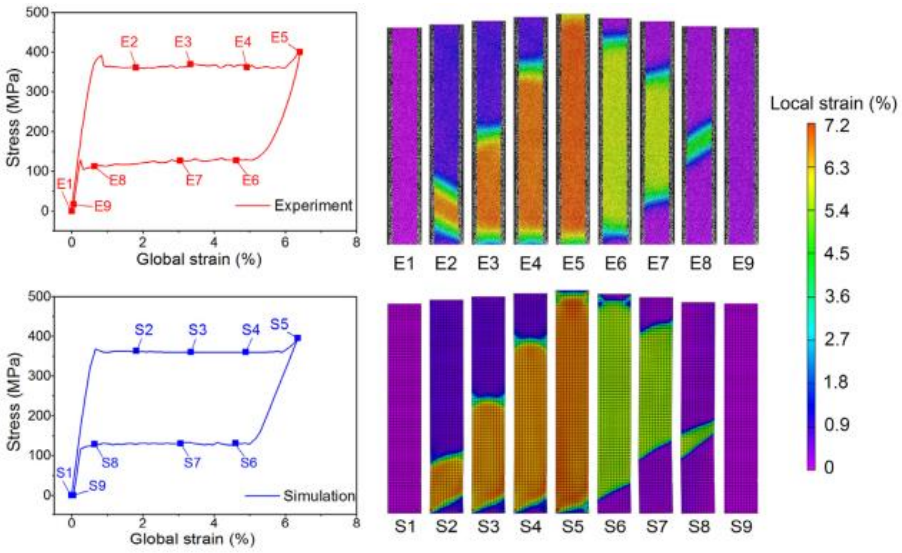


Figure 11 - Experimental and numerical stress-strain response and axial strain contours obtained (XIAO, JIANG, 2020)

2.1.6. Fatigue

Fatigue studies (CATOOR *et al.*, 2019; ZHANG *et al.*, 2022) showed that cracks typically initiate in the transition zones between austenite and martensite, where repeated stress-induced transformations occur and where thermal and plastic concentrations reach their maximum. These findings directly link Lüders-band dynamics to fatigue-damage nucleation, confirming that transformation fronts act as preferential sites for failure initiation. Experimental evidence indicates that stress concentration regions significantly accelerate both mechanisms of fatigue (NARGATTI, AHANKARI, 2021).

Similar phenomena have been observed in β-TiNb alloys (GOLASIŃSKI *et al.*, 2024), the authors confirmed that the local strain rate within the bands can exceed the macroscopic value by an order of magnitude, demonstrating the occurrence of such localized transformation mechanisms in pseudoelastic titanium-based alloys.

Functional fatigue in shape memory alloys is characterized by the reduction of functional properties during cyclic loading. This reduction is influenced by factors such as amplitude, average stress, and load frequency. These properties are related to the phase transformation capacity, hysteresis loop size, maximum recoverable strain, and critical phase transformation

stress (DORNELAS, 2020; DORNELAS *et al.*, 2021a; ZHANG *et al.*, 2022; SONG *et al.,* 2013). Functional fatigue is related to inelastic strains and compromises the service life of shape memory alloys. Figure 12 shows a cyclic test of a SMA wire, where functional fatigue promotes the change in the behavior of the stress-strain curve.

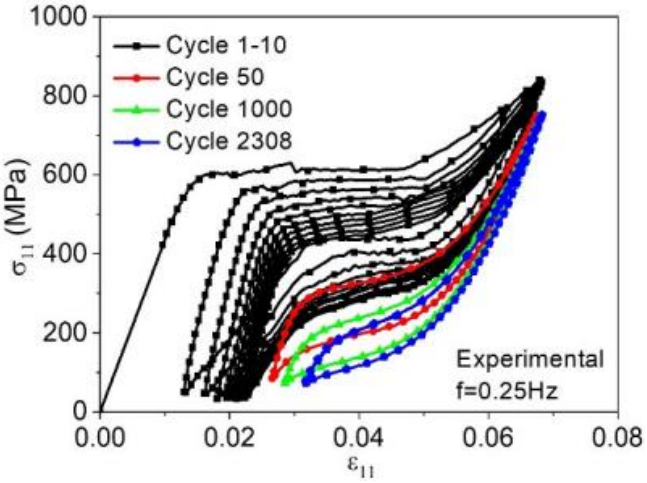


Figure 12- Cyclic loading of a SMA wire where the functional fatigue affects the behavior of stress strain curve (DORNELAS, 2021a)

In addition to functional fatigue, SMAs present structural fatigue, with the same characteristics as the classical fatigue observed in metal alloys (DORNELAS *et al.*, 2021a, b), where microscopic plastic strains occur throughout the cycles.

Structural fatigue is divided into high and low cycle fatigue. High-cycle fatigue occurs when a component is subjected to relatively low stress amplitudes that produce almost entirely elastic deformation, leading to failure only after a large number of cycles and is therefore analyzed using stress-life (S–N) curves. Low-cycle fatigue arises under higher stress levels that cause significant plastic strain during each load cycle, resulting in failure in a much smaller number of cycles and is evaluated using strain-life (ε–N) approaches such as the Coffin–Manson relation (CASTRO, MEGGIOLARO 2009).

The role of geometry as a fatigue damage amplifier has been demonstrated in specimens containing holes, notches, or graded sections. (PAUL *et al.,* 2020; ZITOUNI *et al*., 2023) showed that drilled holes in TiNbZrSn SMAs create heterogeneous stress fields that lead to localized irrecoverable strain accumulation and early functional degradation. Similar conclusions were reached for component-level applications, such as NiTi endodontic instruments, where cyclic nonlinearity and damage are confined to small volumes near stress raisers, motivating localized fatigue assessment strategies (CONGARD *et al.,* 2023). These observations reinforce the notion

that fatigue in SMAs is controlled by local stabilized stress-strain hysteresis loops rather than global loading conditions.

The integrity analysis of a mechanical component aims to calculate the number of cycles for crack initiation. Figure 13 shows curves of equivalent strain and equivalent transformation strain versus number of cycles in SMA tubes experimentally tested with torsion and bending loads.

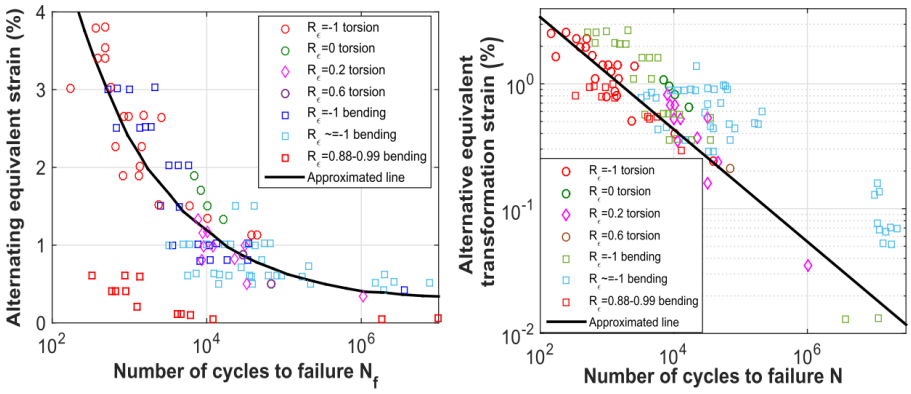


Figure 13 - ε x N_f curves, (a) equivalent strain x number of cycles, (b) equivalent transformation strain x number of cycles (CISSÉ *et al.,* 2016)

2.1.7. Damage

When a material is subjected to cyclic mechanical loading, it undergoes various forms of microstructural damage, including void nucleation and cracking. Eventually, materials subjected to fatigue will fail as a result of these internal damages (PHILLIPS, 2018; DORNELAS *et al.,* 2020). This effect can be considered in the constitutive model as an internal variable of the material (LEMAITRE, CHABOCHE, 1990).

The damage evolution caused by cyclic thermomechanical loading in a notched thin plate is shown in Figure 14 for numerical simulations based on finite element method. In the test, the specimen is tensioned at 300 °C, then the part is subjected to thermal cycles between 150 °C and 300 °C. The notch amplifies both the stress and phase transformation volume fraction, which, under cyclic loads, reduces the component's life.

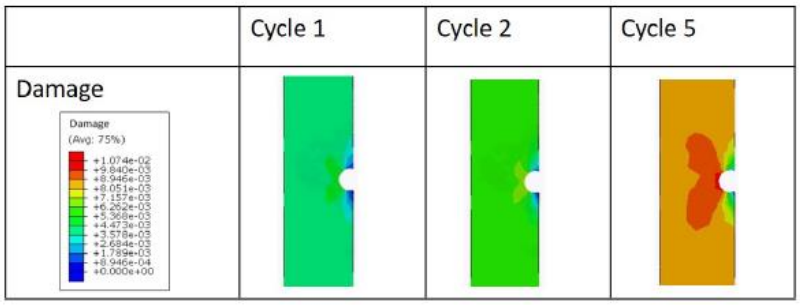


Figure 14 – Evolution of internal damage in a notched plate over 5 actuation cycles (PHILLIPS, 2018)

2.1.8. Fracture Mechanics

Another field of study under development is the fracture mechanics of SMAs, which has a strong correlation with classical fracture mechanics. Traditionally, fracture mechanics are divided into linear elastic fracture mechanics and elastoplastic fracture mechanics. In linear elastic fracture mechanics, it is assumed that the plastic zone at the crack tip is considerably smaller than the size of the notch and the specimen and can therefore be disregarded. In this case, stress intensity factor is used to model the crack growth process. In elastoplastic fracture mechanics, the plastic zone is large in comparison to the notch and specimen size. In such cases, it is necessary to study the energy release around the plastic zone, which is used to calculate crack growth (DOYLE, 2004; ALSAWALHI, LANDIS, 2022).

In shape memory alloys, in addition to knowing the plastic stress field at the crack tip, it is important to identify the martensitic transformation region at the crack tip, since each phase has a different stiffness and thus different resistance to crack opening, as described by BAXEVANIS, LAGOUDAS (2015) and SIMOES, MARTÍNEZ-PAÑEDA (2021).

Figure 15 schematically shows the regions present at the crack tip of an SMA and a stress–strain curve for mode I crack opening, where a plastic region (r_{pl}) and a region with phase transformation (between r_{tr}^{s} and r_{tr}^{f}) can be observed.

At the crack tip, there is a plastic region (with stress above the yield stress); immediately after, a martensitic region; further away, a mixed martensite and austenite region; and even farther, a fully austenitic region.

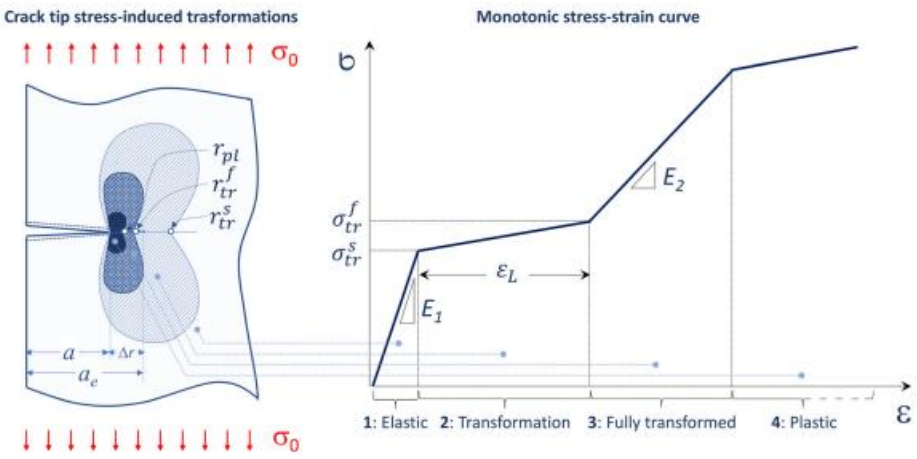


Figure 15 – Description of the regions at the crack tip and the stress–strain curve (SGAMBITERRA *et al.*, 2021)

The reviews by BAXEVANIS, LAGOUDAS (2015) and SHAYANFARD *et al.,* (2021a) addresses the fracture mechanics of shape memory alloys. In their discussion, the authors state that the increasingly complex use of SMAs in applications highlights the need to advance the study of the fracture properties of these materials. The study of stress concentration in SMAs contributes to this effort.

2.2. Experimental methods for SMA characterization

The experimental characterization of SMAs requires the use of multidisciplinary approaches capable of associating microstructural evolution with macroscopic thermomechanical behavior. Since SMAs exhibit complex, temperature and stress-dependent transformations between austenite and martensite, their accurate study can benefit from the combination of characterization techniques with full-field mechanical and thermal measurement methods (LAGOUDAS, 2008; OTSUKA; WAYMAN, 1998). Together, these methods enable a comprehensive understanding of the mechanisms governing phase transformation, plastic accommodation, and functional degradation during cyclic loading.

Microstructural techniques such as Scanning Electron Microscopy (SEM), Transmission Electron Microscopy (TEM) and X-ray Diffraction (XRD) provide insight into the crystallography and morphology of the martensitic and austenitic phases (ZHANG *et al.,* 2024; FAN *et al*., 2017;

FU *et al.,* 2023). These methods allow the identification of precipitates (e.g., Ti_3Ni_4), the evaluation of grain size and texture, and the determination of transformation temperatures, which are key parameters for thermomechanical modeling (HASTUTI *et al*., 2014). Differential Scanning Calorimetry (DSC) is extensively employed to quantify the enthalpy and temperature range associated with forward and reverse transformations (MOHD JANI *et al.*, 2014; ABOUTALEBI *et al.*, 2015; YAMAZAKI, *et al.,* 2023), establishing a direct connection between the microstructural state and phase transformation

Complementary mechanical testing methods—such as uniaxial tension, compression, and cyclic loading—are important to evaluate the pseudoelastic response and the shape-memory effect under controlled thermal conditions. Standardized procedures like ASTM E8 (ASTM, 2007) are normally used to the determination of stress–strain curves and hysteretic behavior, however, because SMAs deform heterogeneously through the nucleation and propagation of transformation bands, conventional pointwise strain measurements are often insufficient to capture the full complexity of their response.

To overcome this limitation, Digital Image Correlation (DIC) has become a powerful optical technique for full-field strain measurement. By tracking a random speckle pattern applied to the specimen surface, DIC enables high-resolution mapping of strain localization, transformation-front propagation, and stress-concentration effects (SUTTON *et al*., 2009). The method has proven particularly effective for NiTi sheets and micro-actuators, where phase transformation is governed by heterogeneous transformation bands (LOUCHE *et al.*, 2012). When combined with conventional mechanical testing, DIC provides a quantitative basis for correlating observed deformation modes with underlying microstructural mechanisms.

In parallel, Infrared Thermography (IRT) has become an essential tool for analyzing the thermomechanical coupling intrinsic to SMAs. Since the martensitic transformation is accompanied by latent-heat release and absorption, temperature fields measured by IRT directly reflect the progress of transformation and the associated energy dissipation (VOLLMER, MÖLLMANN, 2010). Modern infrared cameras, with high spatial and temporal resolution, can detect temperature changes of just a few millikelvin, allowing real-time visualization of transformation bands, stress-concentration zones, and fatigue damage.

Figure 16 shows the phase diagram schematic with the main material properties typically used in constitutive models: σ_{Ms} - Initiation stress for martensite transformation, A_s - Initial temperature of austenite formation at zero stress, A_f - Final austenite formation temperature at zero stress, M_s - Initial temperature of martensite formation with zero stress, M_f - Final temperature of martensite formation with zero stress, σ_{Mf} - Ultimate stress for martensite transformation, σ_{As} - Initial stress for transformation into austenite, σ_{Af} - Ultimate stress for transformation into austenite, C^A - Slope of austenite transformation lines in the stress-temperature plane, C^M - Slope of martensite

transformation lines in the stress-temperature plane, σ_s – Start stress for the detwinning of martensite, σ_f - Finishing stress for the detwinning of martensite, M^d - Maximum temperature at which austenite can be transformed into martensite by applying stress, M^t – Twinned martensite formation temperature. The stress-free transformation temperatures can be obtained by DSC tests while the critical stress transformation for different temperatures can be obtained from temperature controlled tensile tests.

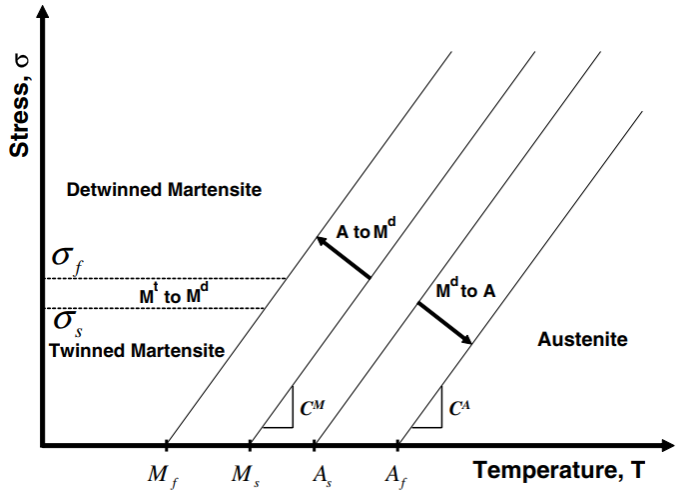


Figure 16- Schematic representation of the phase diagram with material properties (adapted from LAGOUDAS, 2008)

Sections 2.2.1 and 2.2.2 discuss some experimental techniques used along the thesis in order to characterize the material and to study stress concentration phenomena.

2.2.1. Differential scanning calorimetry

Differential Scanning Calorimetry (DSC) is an experimental method usually used to determine phase transformation critical temperatures in SMAs (BEN FRAJ, ZGHAL, 2025). Figure 17 shows a typical DSC plot for an SMA, where it can be observed two transformation peaks. The power required to maintain a constant heating rate for the alloy is represented on the y- axis, while the chamber temperature is reported on the x-axis. The endothermic peak is associated with the transformation from martensite to austenite, meaning that additional heat must be supplied to

maintain constant heating (LECCE, 2015). This phase transformation is identified by two temperatures: the initial austenite transformation temperature (A_s) and the final austenite transformation temperature (A_f). The exothermic peak represents the transformation between austenite and martensite, it is identified by an initial martensite transformation temperature (M_s) and a final martensite transformation temperature (M_f). Throughout the phase transformation process, temperatures are measured using the tangent method (LECCE, 2015).

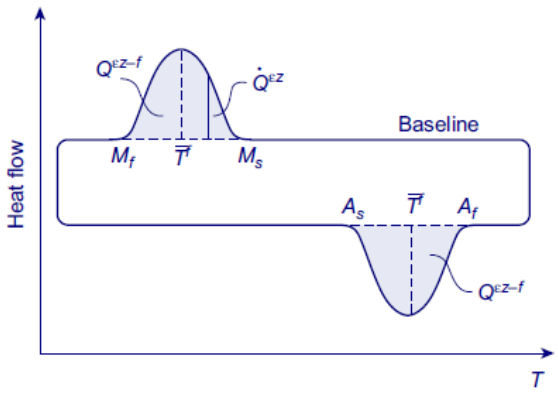


Figure 17- Schematic representation of differential scanning calorimetry (DSC) for SMAs (LECCE, 2015)

2.2.2. Tensile tests

In order to evaluate the stress-strain behavior of SMAs, tensile tests are important to perform monotonic and cyclic tests at different strain rates (AMMAR, *et al.,* 2017). Furthermore, when equipped with specific devices as the DIC, tensile tests are capable to obtain the full strain field that develops in the specimen during the application of the load.

DELPUEYO *et al.,* (2021) presented a literature review about experimental full field methods used for Thermomechanical characterization of SMA components and described different methods for surface or 3D field measurement, i.e.: digital image correlation (DIC), grid method (GM), and moiré interferometry (MI), are dedicated to displacement and strain field measurement while infrared thermography (IRT) contemplates thermal measurements. According to the study, the use of DIC technique and thermography have been increasing over the years due to its capabilities to accurately measure surface strains and temperature, respectively. An example of an electromechanical test machine is presented in Figure 18.



Figure 18 – Electromechanical system Instron 5985. Specimen assembly

2.2.2.1. Digital Image Correlation (DIC)

Digital Image Correlation (DIC) is a non-contact optical technique widely used for measuring full-field surface displacements and strains in experimental mechanics. The method relies on capturing digital images of a specimen surface during the strain evolution and tracking the displacement of a speckle pattern applied to the surface. SUTTON *et al.,* (2009), provides a comprehensive theoretical and practical framework for DIC, including mathematical formulations, experimental setups, and stereo vision systems. An experimental setup using the DIC technique is shown in Figure 19.

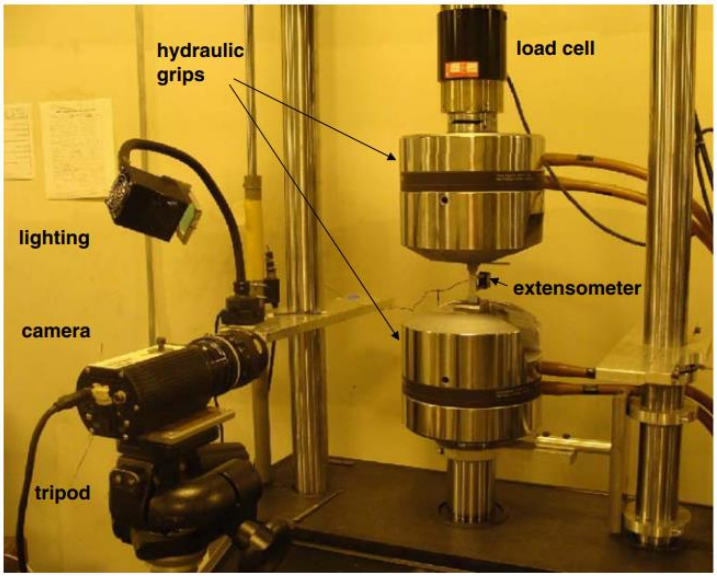


Figure 19 - DIC measurement setup (SUTTON *et al.*, 2009)

The fundamental assumption underlying DIC is the conservation of grayscale intensity, i.e., the grayscale value of a specific point in the reference image is assumed to remain constant in the deformed image. Sub-pixel accuracy is typically achieved using interpolation algorithms, yielding displacement resolution. A detail of a specke pattern, and subset representation is presented in Figure 20.

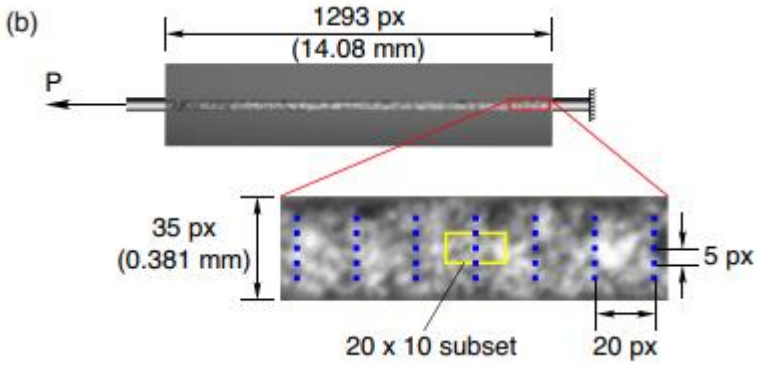


Figure 20 - Specimen with detail of speckle pattern (LOUCHE *et al*., 2012)

Figure 21 illustrates portions of the digital images captured before and after deformation. The displacement of a subset in the reference (undeformed) image is determined by locating, in the deformed image, the region that exhibits the most similar light intensity distribution. Once the corresponding subset is identified in the deformed image, its displacement can be calculated. To

enable this correlation process, the specimen surface must present a distinct texture or speckle pattern that allows accurate matching between subsets (BÁRNIK *et al.*, 2020).

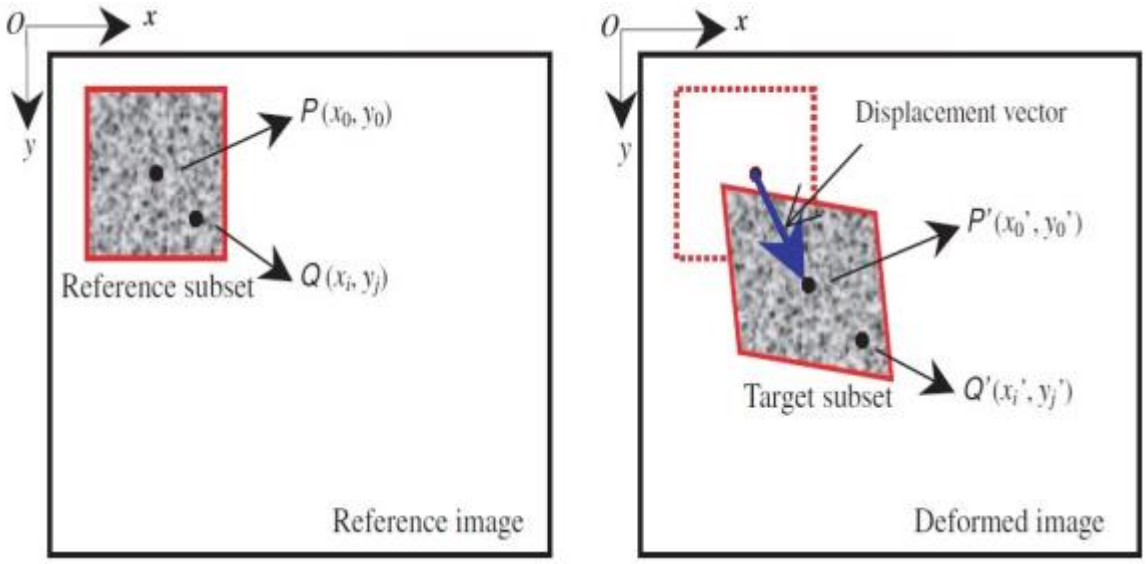


Figure 21 - Illustration of a reference subset before and after deformation (BÁRNIK *et al.*, 2020)

DIC may be implemented in 2D (planar surfaces) or 3D (stereo DIC), where the latter requires synchronized camera pairs and stereo triangulation. The ability of DIC to provide full-field, high-resolution strain data makes it particularly suitable for studying localized phenomena such as stress concentrations and crack tip fields.

The Good Practices Guide for Digital Image Correlation issued by the International Digital Image Correlation Society (IDICs, 2018) outlines critical aspects to ensure the accuracy, repeatability, and uncertainty quantification in DIC applications.

The application of DIC in the analysis of SMAs is particularly advantageous due to the localized and heterogeneous nature of strain resulting from stress-induced martensitic transformations. In the context of stress concentration, DIC enables the precise mapping of strain gradients and phase transformation bands near notches, cracks, or geometric discontinuities.

ROMANOWICZ *et al.,* (2020) explored the use of DIC to characterize stress concentration factors and plastic zone development in notched steel specimens under quasi-static loading. The study compared DIC measurements with finite element simulations and analytical predictions, showing that conventional theoretical models underestimated stress concentration factors due to their inability to capture localized plasticity. DIC, by contrast, effectively identified the spatial evolution of strain concentrations and their sensitivity to notch shape.

In terms of SMAs, LOUCHE *et al.,* (2012) demonstrated the capability of DIC to capture full-field strains during thermo-mechanical cycling of pseudoelastic and shape memory NiTi wires. The study highlighted the challenges of testing SMA wires, including specimen preparation, thermal gradients, and cyclic degradation, while emphasizing the value of 2D and 3D DIC in visualizing strain localization and transformation fronts under Joule heating and mechanical loading.

These studies collectively highlight DIC as an important tool for identifying and quantifying localized strain phenomena in SMAs - particularly in geometrically complex regions.

While DIC offers significant advantages, its accuracy and reliability depend on mitigating a range of error sources, especially in applications involving high strain gradients such as notch tips in SMAs.

HIJAZI, KÄHLER (2017) investigated the contribution of imaging system components to the total uncertainty in 2D-DIC. Their analysis revealed that lens distortion, camera misalignment, and lighting inhomogeneities can contribute up to 15% of the total measurement error. Calibration errors in stereo-DIC were particularly critical, necessitating frequent validation using known displacements and distortion models.

The thickness of the paint layer used to generate the speckle pattern directly influences the fidelity of strain measurements. If the coating is too thick, it may debond or shear independently of the substrate, leading to underestimation of strain. Studies have shown that coatings above approximately 30 µm begin to introduce systematic underestimations of strain, particularly under large deformations (PÉREZ *et al.*, 2015).

GONZÁLES *et al.,* (2017) specifically addressed the challenge of measuring steep strain gradients in notched specimens using a feature-based DIC algorithm. Their implementation of a meshless approach with enhanced accuracy in notch-adjacent regions, where traditional subset-based DIC suffers from spatial averaging and poor convergence. The results emphasized the necessity of high-resolution imaging and adaptive subset techniques when analyzing fracture mechanics in SMA components.

2.2.2.2. Thermography

Infrared thermography, or infrared thermal imaging, is a non-contact optical technique that enables the visualization and quantitative measurement of surface temperature fields in real time (Figure 22). Its theoretical foundation derives from radiation physics, which establishes that all bodies with temperature above absolute zero emits electromagnetic radiation (VOLLMER; MÖLLMANN, 2010).

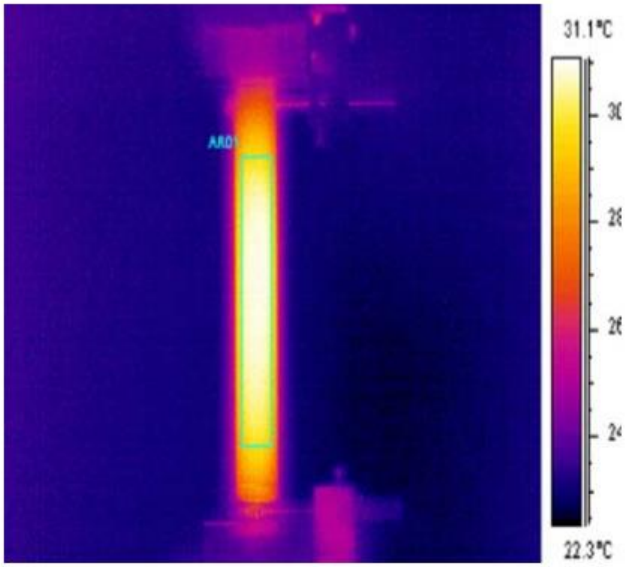


Figure 22 - Temperature measurement by thermography (PIECZYSKA *et al.*, 2012)

Infrared thermography has become a versatile experimental tool in engineering and materials science, particularly for the investigation of materials that exhibit thermomechanical coupling.

Thermographic methods are generally categorized as active or passive. In the active mode, an external excitation source (flash lamp, halogen heater, mechanical vibration, or eddy current) induces a transient thermal contrast that reveals hidden defects or inhomogeneities. Variants include pulsed, lock-in, step-heating, vibro- and eddy-current thermography (VOLLMER, MÖLLMANN, 2010). In contrast, passive thermography relies on naturally temperature variations that occur within the specimen, such as those produced by cyclic loading or friction (PAIVA, 2020).

The strain rate has a significant influence on the temperature distribution in shape memory alloys due to their strong thermomechanical coupling. It has been experimentally observed that heat is produced during the forward martensitic transformation and absorbed during the reverse

transformation. These heat exchanges cause local temperature variations that directly affect the material's mechanical response.

At high strain rates, the phase transformation occurs rapidly, leaving insufficient time for effective heat convection. As a result, the latent heat generated during the transformation accumulates in the material, leading to a noticeable temperature increase. At low strain rates, the transformation occurs more gradually, allowing sufficient time for heat to dissipate. This enables the release of latent heat to the surroundings, resulting in lower temperature levels.

Infrared thermography captures the exothermic and endothermic signatures associated with phase transformations, providing the visualization of the transformation fronts as present in Figure 23.

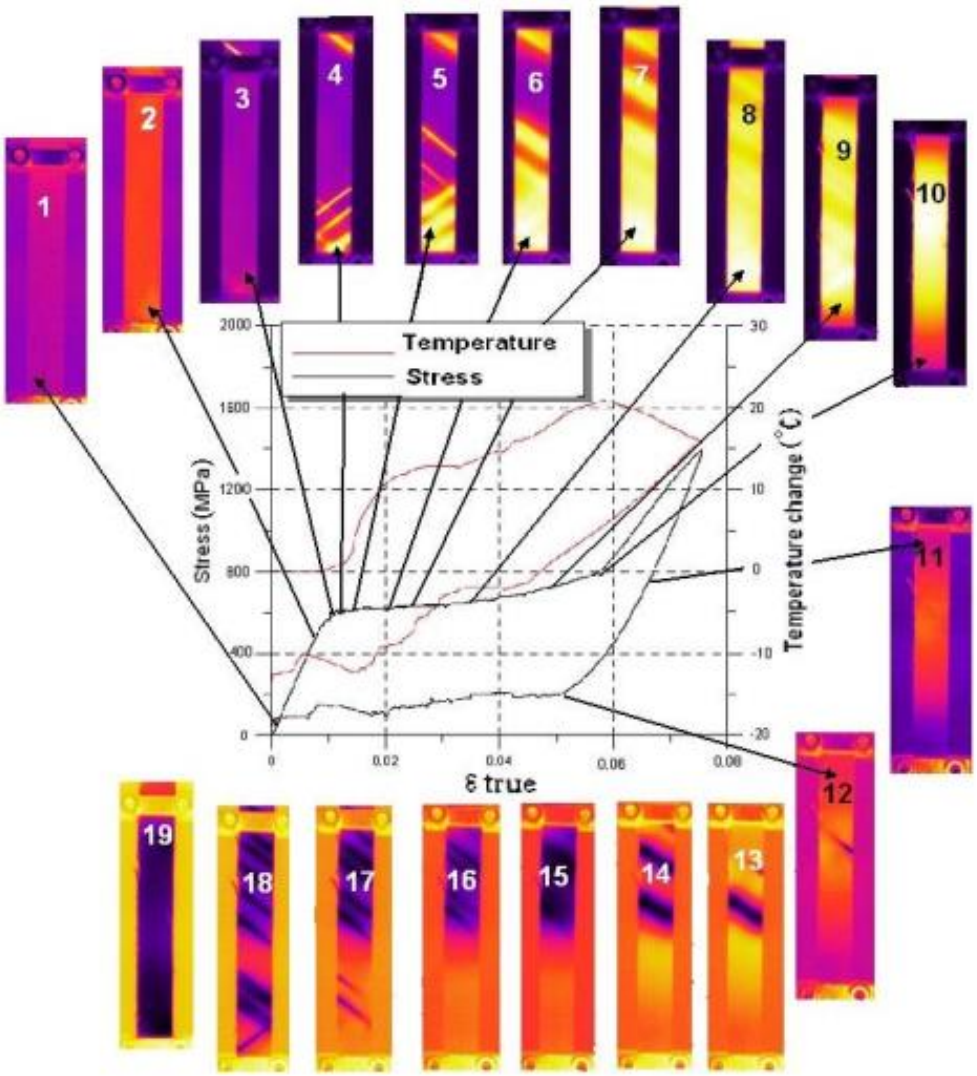


Figure 23 – Experimental stress and temperature evolution as a function of strain for a pseudoelastic plate (PIECZYSKA *et al*., 2012)

Typical tests on pseudoelastic NiTi sheets show the nucleation of narrow inclined thermal bands (analogous to Lüders bands in steels) that propagate through the gauge section during loading. The temperature increase within these bands corresponds to latent heat release from the austenite–martensite phase transformation. Upon unloading, an inverse pattern with temperature decrease marks the reversion to austenite. These reversible yet dissipative processes constitute the core of pseudoelasticity and can be observed through thermography. In specimens containing geometric discontinuities such as holes or notches, thermal maps clearly highlight the stress concentration regions where phase transformation initiates earlier, revealing the mechanical heterogeneity introduced by geometry (Figure 24).

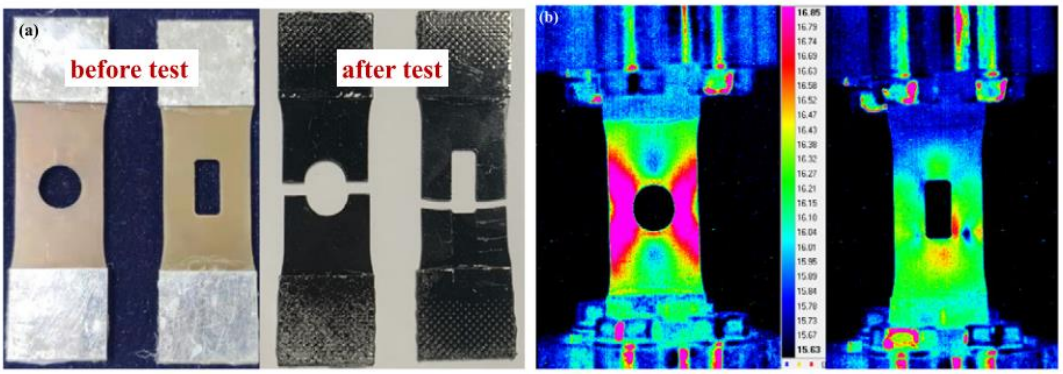


Figure 24 - Samples before and after test and temperature fields (GU *et al.*, 2020)

Infrared thermography is, therefore, an important experimental technique that complements the mechanical and optical techniques normally used to characterize the main behaviors of SMAs. When combined with Digital Image Correlation (DIC), which provides full-field strain data, it allows direct correlation between localized strain and temperature changes. This coupling is invaluable for materials that exhibit complex internal mechanisms, as shown in the full-field optical analyses of, where the integration of DIC enabled the mapping of strain concentrations and energy release near crack tips. This concept is well applied to SMAs, in which DIC and thermography together enable simultaneous measurement of strain localization, transformation propagation, and heat generation as represented in Figure 25.

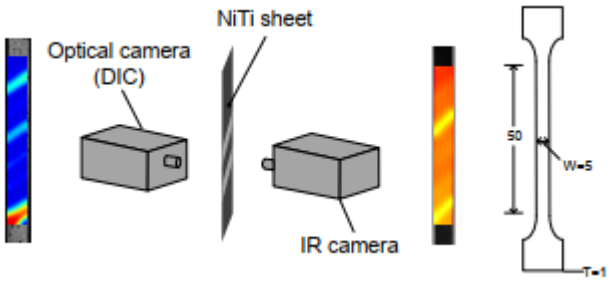


Figure 25 - Experimental setup scheme of the combined DIC and IR measurements (ZHANG *et al*., 2022)

Experimental studies of SMAs by thermography demand specific considerations. Surface emissivity must be enhanced by applying a thin, uniform black coating that does not interfere with mechanical behavior. Calibration using blackbody reference ensures accurate temperature conversion, and synchronization between thermal acquisition and mechanical load signals enables analysis of phase transformation cycles

2.3. Stress concentration

In the design of mechanical components, geometric discontinuities are responsible for increased stresses and strains when compared to regions far from these discontinuities. Therefore, it is important to consider this aspect in the design of mechanical components.

Classical approaches used in the design of mechanical components consider stress analysis in the linear elastic regime. Stresses are calculated at locations far from locations of the application of the loads and/or restrictions (Saint-Venant principle) and far from geometric discontinuities. However, it is common for mechanical components to have geometric discontinuities such as holes, notches, among others, making it necessary to study the stresses maximum values close to these locations.

In the elastic regime, the stress concentration factor (K_σ) is defined as the ratio between the maximum stress value (σ_{max}) and the nominal stress (σ_{nom}):

$$K_\sigma = \frac{\sigma_{max}}{\sigma_{nom}} \quad (1)$$

For a plate with a center hole submitted to a uniaxial loading, the nominal stress is normally calculated as:

$$\sigma_{nom} = \frac{F}{\left(\frac{w-d}{t}\right)} \tag{2}$$

where F refers to the applied uniaxial force, and w, d and t represents the width, hole diameter and thickness, respectively.

In the case of the strain concentration factor (K_ε), a similar way is employed, that is, the ratio between the maximum strain (ε_{max}) and the nominal strain (ε_{nom}):

$$K_\varepsilon = \frac{\varepsilon_{max}}{\varepsilon_{nom}} \tag{3}$$

$$\varepsilon_{nom} = \left(\frac{u}{l_0}\right) \tag{4}$$

where u refers to the longitudinal displacement, and l_0 is the reference initial length.

There are analytical solutions that allow the calculation of such factors. One can use as an example the Kirsh problem (CASTRO, MEGGIOLARO, 2009), which provides equations for the stress field in an infinite plate with a circular hole loaded axially. Through these equations it is possible to obtain an analytical value for K_σ.

Kirsh's solution shows that the stress concentration factor value is equal to 3 at the edge of the hole, and 1 away from the hole, where the stress value is equal to the nominal stress. The value of K_t is different when the plate is not infinite, and the effect of the plate edge is considered.

The classic stress concentration factor for elastic behavior in a semi-infinite plate with a hole can be calculated using the analytical equation proposed in (CASTRO, MEGGIOLARO, 2009):

$$K_\sigma = 3.00 - 3.13\left(\frac{2r}{D}\right) + 3.66\left(\frac{2r}{D}\right)^2 - 1.53\left(\frac{2r}{D}\right)^3 \tag{5}$$

In the elastoplastic case, the stress concentration factor is different from that calculated in the linear elastic case. After yielding, the stress concentration factor (K_σ) presents a decreasing behavior while the strain concentration factor (K_ε) increases, as shown in Figure 26. This behavior is associated with a process of redistribution of the stress field in the region close to the geometric discontinuity promoted by the evolution of plastic strain.

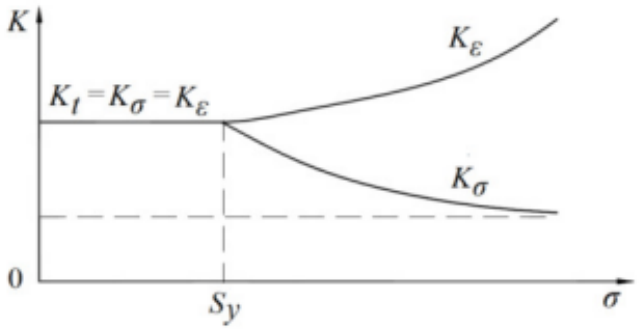


Figure 26- Elastoplastic stress and strain concentration factors (GONZÁLES, 2014)

For situations involving elastoplastic behavior, an approach using the Neuber rule (NEUBER, 1961) is normally used, that considers a definition of a stress concentration factor as:

$$K_t = \sqrt{K_\sigma K_\varepsilon} \tag{6}$$

For more complex geometries and loads, these values can be determined using experimental and numerical methods. A widely used numerical method for this purpose is the finite element method. In the literature (PILKEY, 1997), there are many examples of stress concentration factors being calculated using models that consider the behavior of the material in the elastic and elastoplastic regimes. Studies can also be found for SMAs, which are more complex due to the characteristics of material behavior. The martensitic transformations present in regions close to the notch significantly alter the stress distribution in this region, affecting the calculation of the stress concentration, especially when dealing with cyclic loading.

2.3.1. Studies on stress concentration in shape memory alloys

2.3.1.1. Shape memory effect

The study of stress concentration phenomena in SMAs, particularly in nickel–titanium (NiTi) systems, has gained relevance due to the complex relation between mechanical loading, phase transformation, and temperature-dependent material behavior. Unlike conventional metals, SMAs exhibit strong thermomechanical coupling arising from reversible martensitic transformations. When geometric discontinuities (such as holes, notches, or grooves) are introduced, local stress and strain fields become highly nonuniform, directly influencing the initiation and propagation of phase transformation zones (SHAYANFARD *et al.,* 2021 a,b). Understanding these local effects is fundamental for predicting functional fatigue, energy dissipation, and structural reliability in SMA-based components. Over the past decades, several experimental, analytical, and numerical studies have sought to describe how stress concentration modifies the pseudoelastic response of NiTi alloys under different thermal and mechanical loading paths.

LAGOUDAS, (2008) presented a numerical study with a plane-strain NiTi SMA thick plate with a central hole subjected to a combined thermomechanical loading path to evaluate the model response under non-proportional loading conditions. Mechanical loading at low temperature generates pronounced stress concentrations near the hole, promoting the detwinning of self-accommodated martensite and illustrating the role of geometric discontinuities in strain localization. Subsequent heating under constrained displacements leads to sequential phase transformations which significantly modify local stiffness and redistribute stresses throughout the domain.

A study by ARMATTOE (2014) examined the influence of temperature on phase transformation in thin notched plates subjected to tensile loading–unloading cycles (Figure 27). The results demonstrated that lower testing temperatures promote more extensive martensitic transformation around the notch. This behavior is associated with the reduction of critical transformation stresses as temperature decreases. At elevated temperatures, no martensitic transformation was observed, even in the vicinity of the stress concentrator. In contrast, at lower temperatures, a more complex phase transformation distribution was detected around the square hole, including regions with relatively low stress levels where no transformation occurred.

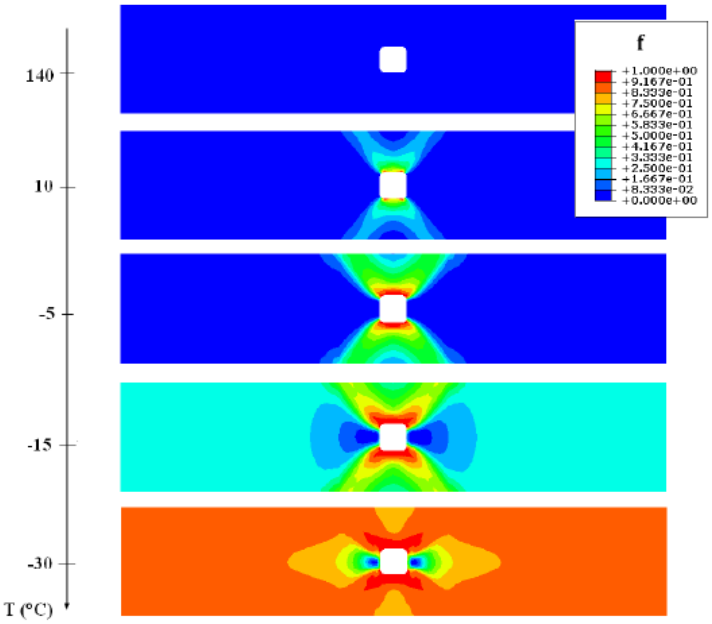


Figure 27- Martensite volume fraction in a plate with a hole at different temperatures (ARMATTOE, 2014).

An investigation by PHILLIPS (2018) further explored the distribution of phase transformation under different geometric conditions associated with stress concentration (Figure 28). The author observed that specimens with greater straight ligament lengths exhibited transformation extending toward the center of the specimen, while those with sharper notches showed incomplete transformation near the midsection. In configurations with smooth transitions, transformation developed more uniformly across the section, whereas in cases, stress gradients led to localized transformation zones.

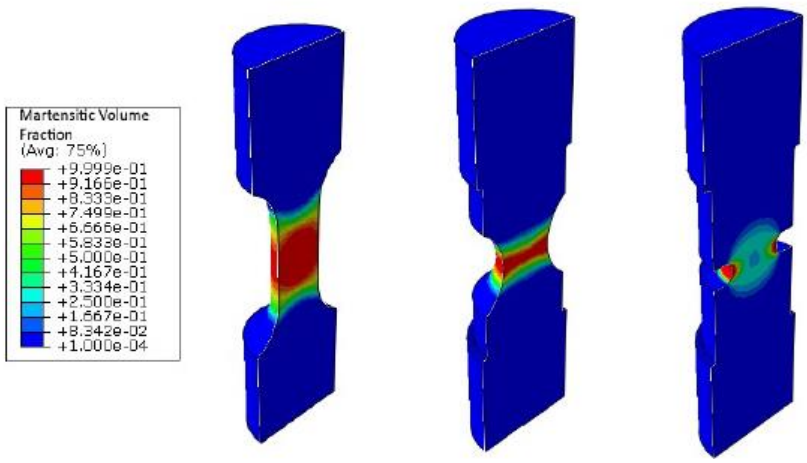


Figure 28- Distribution of the martensite volume fraction under three softening conditions (PHILLIPS, 2018).

HARTL, LAGOUDAS (2009) studied stress concentration effects while considering viscoplastic flow under different loading rates. Their results showed that the rate of load application significantly affects the transformation behavior: longer loading durations allow for viscoplastic accommodation and lower local martensite concentrations (interpreted as localized creep), while higher loading rates result in greater localization of martensitic transformation.

The study conducted by XU *et al.,* (2020) analyzed the distributions of maximum principal stress and martensite volume fraction in a thin NiTi plate with a circular hole subjected to constant-stress loading (Figure 29). The authors reported a characteristic circumferential distribution of both stress and phase transformation zones around the hole, reflecting the strong mechanical–thermal coupling in NiTi alloys.

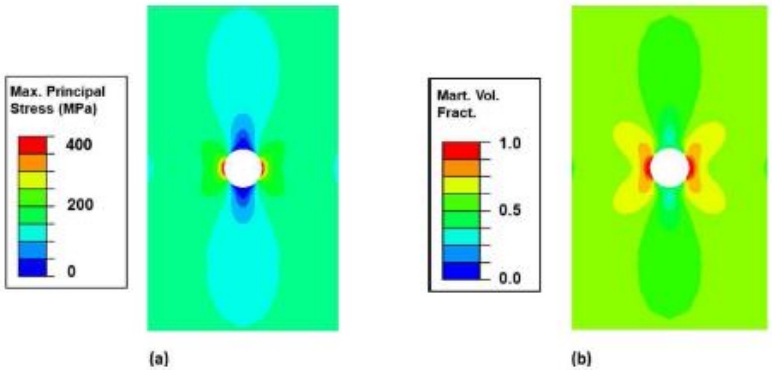


Figure 29- SMA plate with a hole: (a) stress distribution and (b) martensite fraction (XU *et al.*, 2021).

In addition, XU *et al.* (2020) compared axial strain results obtained from their finite element model—which included the Transformation Induced Plasticity (TRIP) effect—with experimental data measured by Digital Image Correlation (DIC) and Differential Scanning Calorimetry (DSC) during thermal cycles between 7 °C and 127 °C at a constant tensile stress of 136 MPa (Figure 30). The numerical and experimental results showed excellent correlation, confirming the model's ability to capture the coupled evolution of stress, strain, and transformation in perforated NiTi plates under thermomechanical loading.

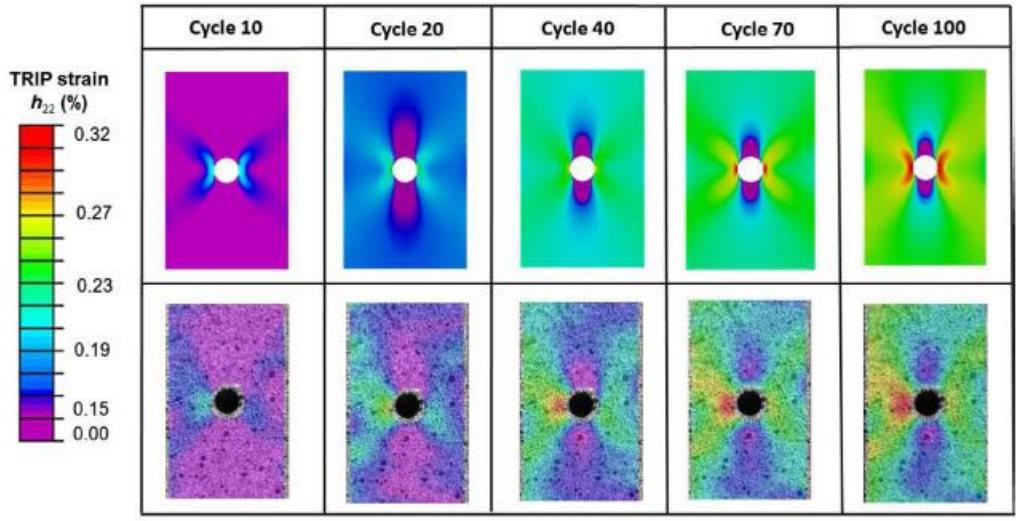


Figure 30 – Comparison of the TRIP strain distribution over different cycles: (a) numerical results and (b) experimental results (XU *et al.*, 2021).

2.3.1.2. Pseudoelasticity

The analysis of stress concentration factors plays a critical role in the design of notched and perforated structural components. Analytical models are frequently employed to describe stress distributions and to predict the onset and propagation of cracks under various loading conditions (HASAN, BAXEVANIS, 2019; SIMOES, MARTÍNEZ-PAÑEDA, 2021). In pseudoelastic materials, understanding stress concentration is also fundamental for assessing damage mechanisms and functional degradation (PHILLIPS *et al*., 2019).

Several studies have addressed the effects of geometric discontinuities in pseudoelastic thin sheets. (MURASAWA *et al.,* 2011*)* conducted finite element analyses on 1 mm-thick pseudoelastic sheets with double U-shaped notches. Their comparison between numerical and experimental stress–strain curves for both notched and unnotched specimens revealed discrepancies arising from localized phase-transformation bands not captured by the simulations. ZHU *et al.,* (2013) examined NiTi plates containing hole arrays and emphasized the need to incorporate plasticity effects to achieve accurate predictions of stress fields and martensite volume fractions. In a subsequent work ZHU *et al., (2014)* demonstrated that plastic deformation patterns depend on hole configuration: clustered holes promote more uniform stress redistribution, whereas dispersed holes intensify local plasticity.

SHARIAT *et al.,* (2013) numerically analyzed pseudoelastic sheets with holes of varying diameters, spacing, and orientation, showing that the deformation pattern is highly sensitive to both the number and size of holes. Later, SHARIAT *et al.,* (2014a) proposed a constitutive model, validated with experimental data, capable of predicting the stress–strain response in both pseudoelastic and steel sheets with holes. Their findings indicated that increasing porosity decreases the stiffness, while larger holes lead to sharper stress gradients between hole boundaries and sheet edges due to redistribution driven by phase transformation effects. An analytical approach developed by SHARIAT *et al.,* (2014b) also successfully reproduced the stress–strain behavior of sheets with circular holes. XIAO *et al.,* (2016) investigated pseudoelastic NiTi plates with double-edge semicircular notches and found that deeper notches produced higher local strains and more intense transformation activity.

In perforated and multi-hole configurations, the temperature and phase-transformation state further govern recoverability and residual strain, as demonstrated in perforated NiTi strips subjected to tensile and bending loading by ALTAS *et al.,* (2022).

More recent research has applied the stress-concentration approach to analyze SMA components with geometric discontinuities, emphasizing the need for SMA-specific criteria that capture transformation-induced stress redistribution and local hysteresis effects (CONGARD *et al.*, 2023; GU *et al.,* 2020).

HOSSEINI, ASHRAF (2023) incorporated both martensitic transformation and plasticity into a constitutive framework to calculate stress concentration factors, showing that local stresses near holes increase during phase transformation, potentially triggering plastic yielding and influencing functional fatigue. Recent studies by SILVA *et al.*, (2023, 2024a,b, 2025a,b) examined stress redistribution induced by cyclic phase transformation in thin pseudoelastic sheets using experiments and numerical simulations. These works proposed an approach to obtain stress and strain concentration factors, also demonstrating that heat treatment and training process significantly affects the cyclic stress–strain response due to changes in critical transformation stresses and temperatures.

The main challenges in this field arise from the limited number of studies addressing stress concentration in trained SMA sheets containing geometric discontinuities. In addition, only a few investigations have established a direct correlation between stress concentration factors and both low- and high-cycle fatigue behavior. Furthermore, the combined effects of thermomechanical coupling and stress concentration remain insufficiently explored, particularly under cyclic loading, making their accurate representation a continuing challenge for the field.

3. EXPERIMENTAL PROCEDURES

This section describes the experimental procedures used in this work. First, experimental tests are developed to characterize the material as received, using DSC and ASTM 2516 standard tensile tests. Next, heat treatments and training processes involving cyclic mechanical loading are studied with the aim of obtaining a material condition where the pseudoelastic effect is maximized. The coupling between phase transformation and plasticity is also analyzed, considering tensile tests involving the presence of the two effects. Finally, the experimental techniques of Digital Image Correlation and IR Thermography are performed in standard tensile specimens and in plates with holes to assess the effects of stress concentration on the strain and temperature fields during the application of mechanical loads.

3.1. Material characterization – As received condition

The specimens were obtained from a pseudoelastic near-equiatomic NiTi sheet measuring 200 mm in length, 100 mm in width, and 1 mm in thickness, supplied by Nexmetal Corporation with a specified A_f temperature of -10°C. Tensile test specimens were cut from the sheet by electric discharge machining (EDM), and the DSC test specimen was prepared from the remaining portion of the plate using a Struers Minitom cutting machine. Each DSC specimen weighed between 20 and 30 mg.

A DSC analysis (Netzsch model DSC200 F3) was performed in Mecanon LAB (COPPE/UFRJ) to determine the transformation temperatures in specimens quenched. For the DSC tests, a temperature range between -150°C and 120°C was used, with a constant heating/cooling rate of 10°C/min. Figure 31 presents the DSC preparation process as follow: (a) cutting machine, (b) DSC specimen (circled in red), (c) part weighting and, (d) DSC equipment.



(a) (b) (c) (d)

Figure 31 – DSC sample preparation: (a) cutting machine, (b) DSC specimen (circled in red), (c) part weighting and, (d) DSC equipment.

The results of DSC analysis of different heat treatment temperatures are shown in Figure 32. In the AR (As Received) condition, it can be noted that the phase transformation enthalpy is very small, so that the peaks related to the phase transformation are difficult to identify and are practically absent. This behavior may be due to mechanical work performed on the sheet during manufacturing, such as that resulting from a rolling process (VILARINHO *et al.,* 2010; ZHENG *et al.*, 2008).

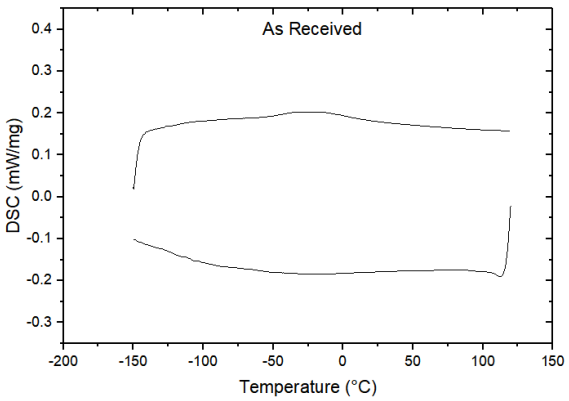
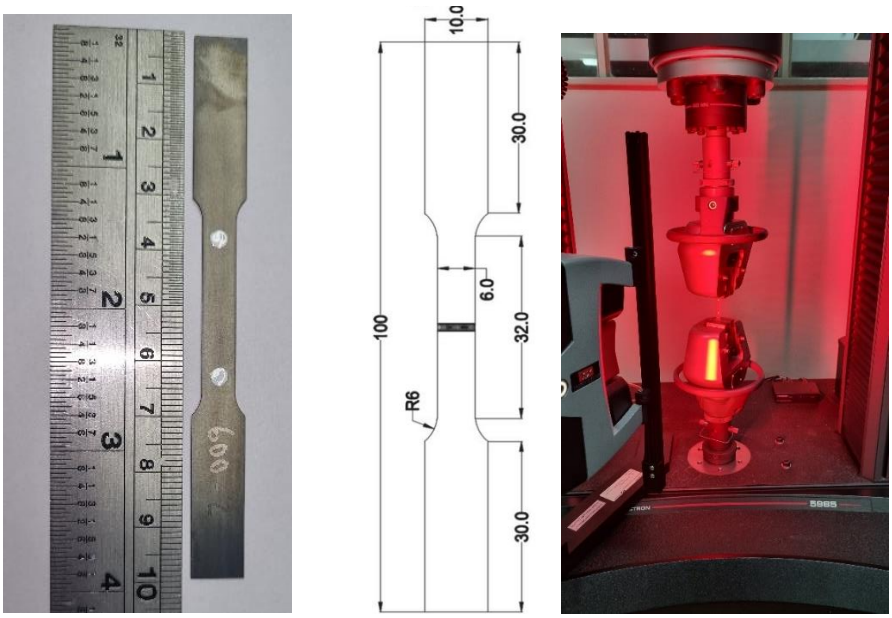


Figure 32 - DSC test results: (a) As Received (AR)

Tensile tests were performed in specimens with the geometry recommended by the ASTM E8 standard (ASTM, 2007), with 1 mm thickness, 10 mm width, and a total length of 100 mm. The specimens are obtained from the same pseudoelastic sheet described for the DSC tests and fabricated using a wire electrical discharge machining (EDM). The tensile test specimen, the drawing with dimensions and its setup on the test machine, is presented in Figure 33. The two

white marks in the specimen are used as reference marks to measure axial strain with a non-contact video extensometer until the specimen reaches the defined strain during the test.



(a) (b) (c)

Figure 33 - Tensile test with dimensions: (a) specimen (b) drawing with dimensions in millimeters (c) assembly on the test machine

The samples were tested in an Instron model 5985 universal testing system equipped with a 50 kN load cell at room temperature (LAMAT - PPEMM/CEFET/RJ).

Initially, a tensile test was conducted following the ASTM 2516 standard (ASTM, 2022). First, a loading step up to 6% strain at a strain rate of 0.02 mm/min is applied, followed by the unloading until the stress reaches 7 MPa. After that, a second load at the strain rate of 0.2 mm/min takes place until the fracture of the specimen.

Figure 34 shows the stress-strain curve for a tensile test performed with a specimen in an AR (as received) condition, following the ASTM F2516 standard (ASTM, 2022) The plateau characteristic of pseudoelasticity is not observed in the test and there is relatively small hysteresis. The rupture occurred at 1300 MPa stress with a 17.5% strain.

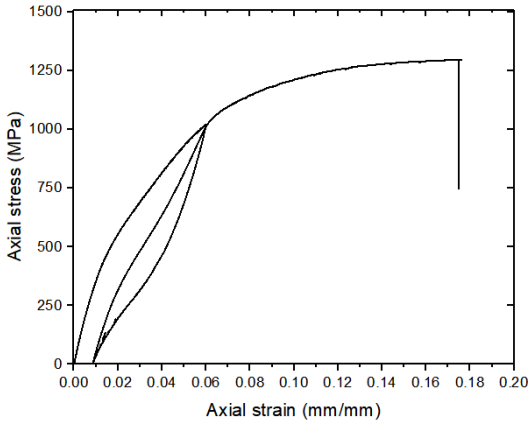


Figure 34 – ASTM 2516 test result for a specimen in an AR condition

For the training process, a prescribed cyclic displacement loading was applied through a sequence of quasi-static triangular waves at a rate of 1%/min (1.67 x 10^{-4} s^{-1}). The strain was measured using a non-contact video extensometer (Instron model AVE 2). Ten cycles were applied during ten cycles.

The AR specimen under the training procedure also presented no pseudoelastic plateau and had a residual strain due to TRIP of 3.8% (Figure 35). The black curve presents the first cycle, the red curve the stabilized cycle (10^{th} cycle), and the gray line indicates the cyclic evolution from 2^{nd} to 9^{th} cycles. The hysteretic loop experiences a gradual reduction during the training cycles and in the 10^{th} cycle reaches a stabilization condition.

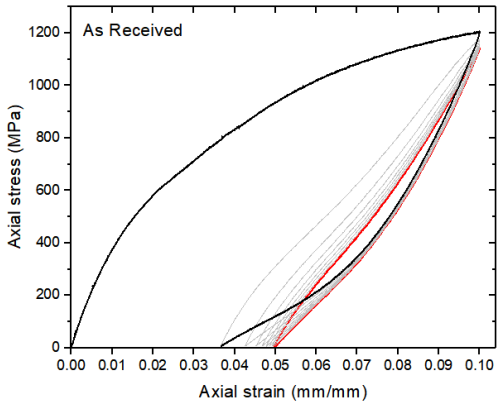


Figure 35 – Stress-strain curve - As Received specimen

The material AR did not exhibit typical pseudoelastic behavior, with a very narrow hysteretic loop. Therefore, a series of heat treatments and training procedures were developed to achieve an adequate condition for studying the stress concentration phenomena.

3.2. Heat treatment and training analysis

The experimental results described in the last section show that the material in AR condition does not present the typical pseudoelastic behavior. To obtain adequate material conditions to permit the analysis proposed in this work, it was necessary to develop a study of heat treatments aiming to improve pseudoelastic behavior. First it is necessary to achieve a condition that presents a final austenitic transformation temperature (A_f) below the room temperature. Therefore, DSC tests were performed to evaluate the transformation temperatures for several heat treatment conditions. Then, a series of cyclic mechanical tests with training are performed, after the heat treatments, to study their influence in pseudoelastic behavior.

After the cuttings from the original plate, heat treatments were performed in a temperature-controlled furnace Jung model 1813 (LASOL - PPEMM/CEFET/RJ, present in Figure 36, with different temperatures and soaking times, followed by rapid cooling in water. A furnace temperature stabilization time of 120 minutes was used before each heat treatment.



Figure 36 - Temperature-controlled furnace

After the specimen preparation, a series of heat treatments aiming to analyze the effect on transformation temperatures were conducted. The material supplier recommended a heat

treatment at 530°C for 10 minutes. There is a lack of literature on the effect of heat treatment for short soaking times, as the one recommended by the manufacturer. Therefore, several furnace temperatures and soak times conditions have been explored, according to Table 1.

Table 1 – Temperatures and furnace times for heat treatment

Temperature	**100°C**	**400°C**	**500°C**	**530°C**	**600°C**
Soaking time	1h	1h	1h	10 min	1h

3.2.1. Differential Scanning Calorimetry (DSC) tests

The results of DSC analysis for the five different heat treatment temperatures are shown in Figure 37 a-e (with upper lines related to heating and lower lines related to cooling). In the same way as AR test Figure 32, for the 100°C condition, transformation temperatures are absent.

Results for the 400°C condition indicate R phase formation during both heating and cooling, while for 500°C the R phase formation is observed only during the cooling phase. For 600°C and 950°C the presence of R phase is not observed.

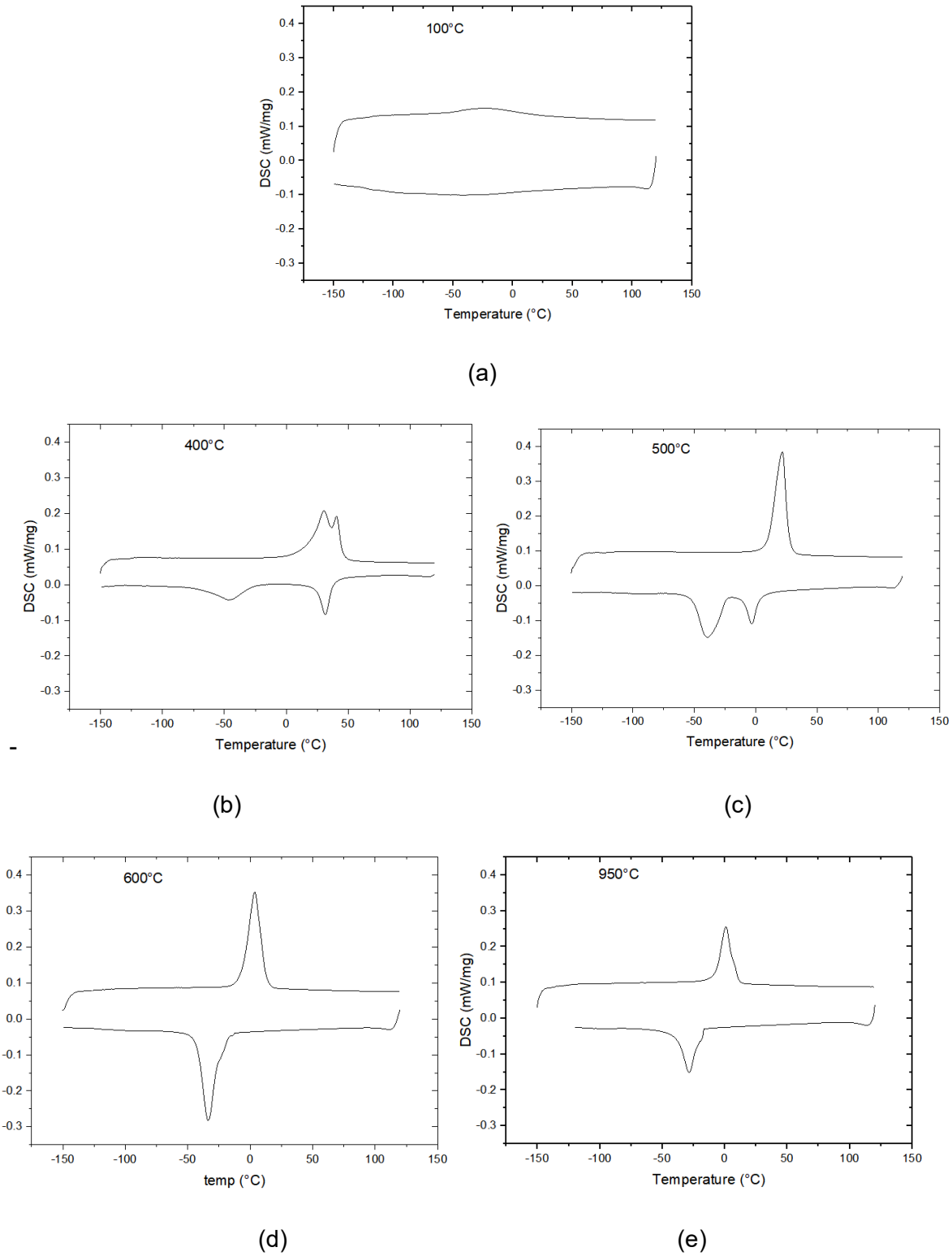


Figure 37 - DSC test results for different heat treatments: (a) 100 °C, (b) 400°C, (c) 500°C, (d) 600°C and (e) 950°C

The transformation temperatures obtained from the specimens heat treated between 400°C and 950°C are presented in Figure 38. M_s, M_f, A_s, and A_f are the martensite start, martensite finish, austenite starts, and austenite finish transformation temperatures, respectively. R_{sm}, R_{fm}, are R-phase start and finish temperature for the forward transformation, whereas R_{sa} and R_{fa} are R-phase start and finish temperature for the reverse transformation, respectively.

Table 2 and Figure 38 shows the critical transformation temperatures as a function of the heat treatment temperature. As the heat treatment temperature increases, M_s, A_s, and A_f tend to decrease, while M_f tend to get larger, mainly in the range of 400 °C to 600 °C.

Table 2 – Evolution of transformation temperatures according to heat treatment temperature

Transformation Temperature (°C)	**Heat Treatment Temperature (°C)**			
	400	500	600	950
A_s	12.2	11.1	-7.1	-7.6
R_{sa}	36.12			
R_{fa}	37.2			
A_f	45.7	27.5	13.9	8.9
M_s	40.5	4.6	-20.9	-19.5
R_{sm}	-7.7	-10.4		
R_{fm}	-21.6	-23		
M_f	-72.5	-51.7	-42.5	-39.1

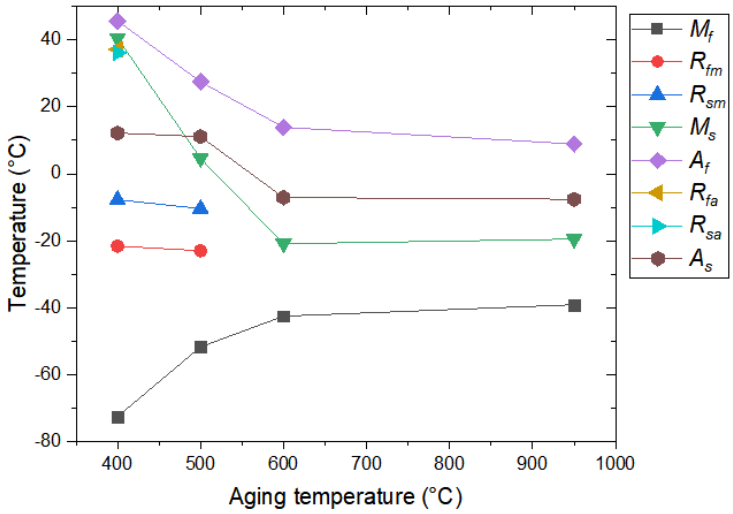


Figure 38 – Dependence of transformation temperatures on the heat treatment temperature

The DSC test result of the specimen heat treated at 530°C for 10 minutes is presented in Figure 39 (with upper lines related to heating and lower lines related to cooling). The result shows that the R phase does not develop during the heating stage, but an intermediate R phase is observed during cooling. Also, a lower value of A_f is observed in comparison with the other heat treatment conditions.

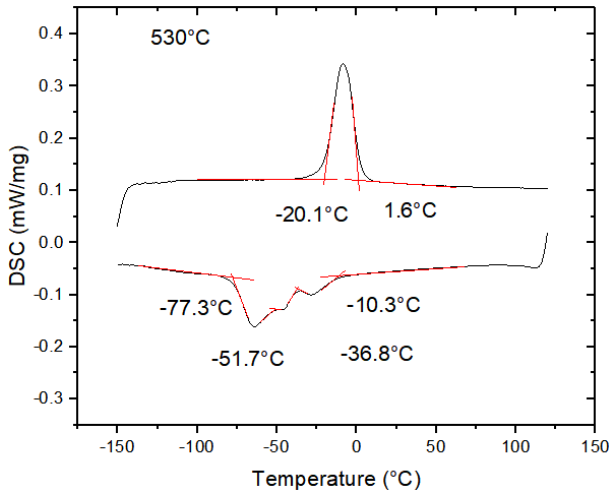


Figure 39 – DSC test result for 530°C with 10 minutes of soaking time

3.2.2. Training process

In addition to analyzing the influence of heat treatments in the transformation temperatures, it was necessary to study the influence of cyclic mechanical training in the stabilized hysteresis loop for each condition. Figure 40 present a specimen mounted in the test machine used to provide mechanical cyclic training of the specimens.



Figure 40 - Specimen mounted in the test machine.

For the training process, similarly to the procedure used in the as-received (AR) specimen, a prescribed cyclic displacement-controlled loading was applied using a sequence of quasi-static triangular waves at a rate of 1% min^{-1} (1.67×10^{-4} s^{-1}). The strain also was measured using a non-contact video extensometer Instron model AVE 2. Ten cycles were applied. The tests were performed on model 5985 universal testing system equipped with a 50 kN load cell at room temperature (LAMAT - PPEMM/CEFET/RJ).

Table 3 presents the heat-treatment temperatures and corresponding training strain levels applied to the specimens. Three temperatures (500, 530, and 600 °C) were selected, with holding times of 1 h for the 500 °C and 600 °C treatments and a furnace time of 10 min for the 530 °C condition. A maximum training strain of 10% was applied to all heat-treatment conditions to establish a common reference state involving near-complete martensitic transformation. In addition, intermediate strain levels were introduced to investigate the influence of transformation amplitude and cyclic stabilization on the hysteretic response.

Table 3 – Temperature heat treatment and training strain of the specimens

Temp. heat treatment	**600°C**	**600°C**	**500°C**	**500°C**	**530°C**	**530°C**	**530°C**
training strain	10%	8%	10%	7%	10%	6.50%	4%

To analyze the effect of stress concentration in pseudoelastic plates, it is essential that the material exhibits a well-defined pseudoelastic response. Therefore, in this work, the hysteresis area, associated with the material's energy dissipation in the 10th loading cycle, is adopted as a key parameter to establish the optimal material condition (KANG *et al.,* 2012; RAMOS *et al.,* 2018; YOU *et al.,* 2020; GONZÁLEZ-SANZ, *et al.,* 2019).

$$E_d = \oint \sigma d\varepsilon \tag{7}$$

Figure 41 shows the stress-strain curves for the specimens submitted to the different heat treatment conditions. Here, also the black curve presents the first cycle, the red curve the stabilized cycle (10th cycle), and the gray line the cyclic evolution from the first to the stabilized cycle.

Figure 41 (a) and (b) show the stress-strain curves for the specimens heat treated at 500°C for 1 hour, at 7% and 10%, respectively. The specimen trained with 10% strain reaches a stress value of 900 MPa. This stress value is beyond the yielding stress, and during the unloading the specimen did not transform back to austenite. The specimen trained with 7%, despite reaching the end of martensitic phase transformation, did not develop plastic strain, and similarly to the 10% training condition, no austenitic phase transformation occurred during unloading, the maximum stress levels were below 400 MPa and the strain range in the hysteretic loops developed between a range of 5.5 and 7%.

The stress-strain curves for the specimen treated at 600°C are presented in Figure 41 (c) and (d). The specimen trained with 8% strain (Figure 41(c)) completed the phase transformation in the first cycle and transformed back to austenite during unloading with a residual strain of 0.9%. From the second cycle on, the stress becomes higher than the one observed in the first cycle, and during the unloading, a TRIP strain is equal to 4.1%. For the following cycles, the residual strain becomes closer to each other until stabilizes in 5.5% during the 10^{th} cycle.

The specimen trained with 10% strain (Figure 41(d)) shows a pseudoelastic plateau during the first cycle during the phase transformation process, followed by plastic strain. During the unloading, the curve shows no reverse transformation back to austenite and presents a high value of Transformation Induced Plasticity (TRIP) strain (7.8%).

The specimens treated at 530°C for 10 minutes are presented in Figure 41(e-g). Figure 41(e) shows the stress-strain curve for the 4% training specimen. The prescribed strain was not enough to complete the martensitic phase transformation, and during the unloading, the residual strain due to TRIP was reduced. In the final cycle, the residual strain reaches 1% and the maximum stress value remains at 450 MPa.

Figure 41(f) presents the stress-strain curve for the 6.5% training. In this case, the specimen transforms completely with no yielding, and during the unloading, the reverse transformation takes place with a reduced TRIP residual strain. In the following cycles, the stress values converge to a value that is higher than the first cycle and the TRIP strain tend to stabilize.

The part trained with 10% strain (Figure 41 (g)) reached the plastic zone but transformed back to austenite during the unloading. A residual strain is observed due to plasticity and TRIP, and the following cycles present a reduction of stress values, progressively converging to the residual strain due to TRIP.

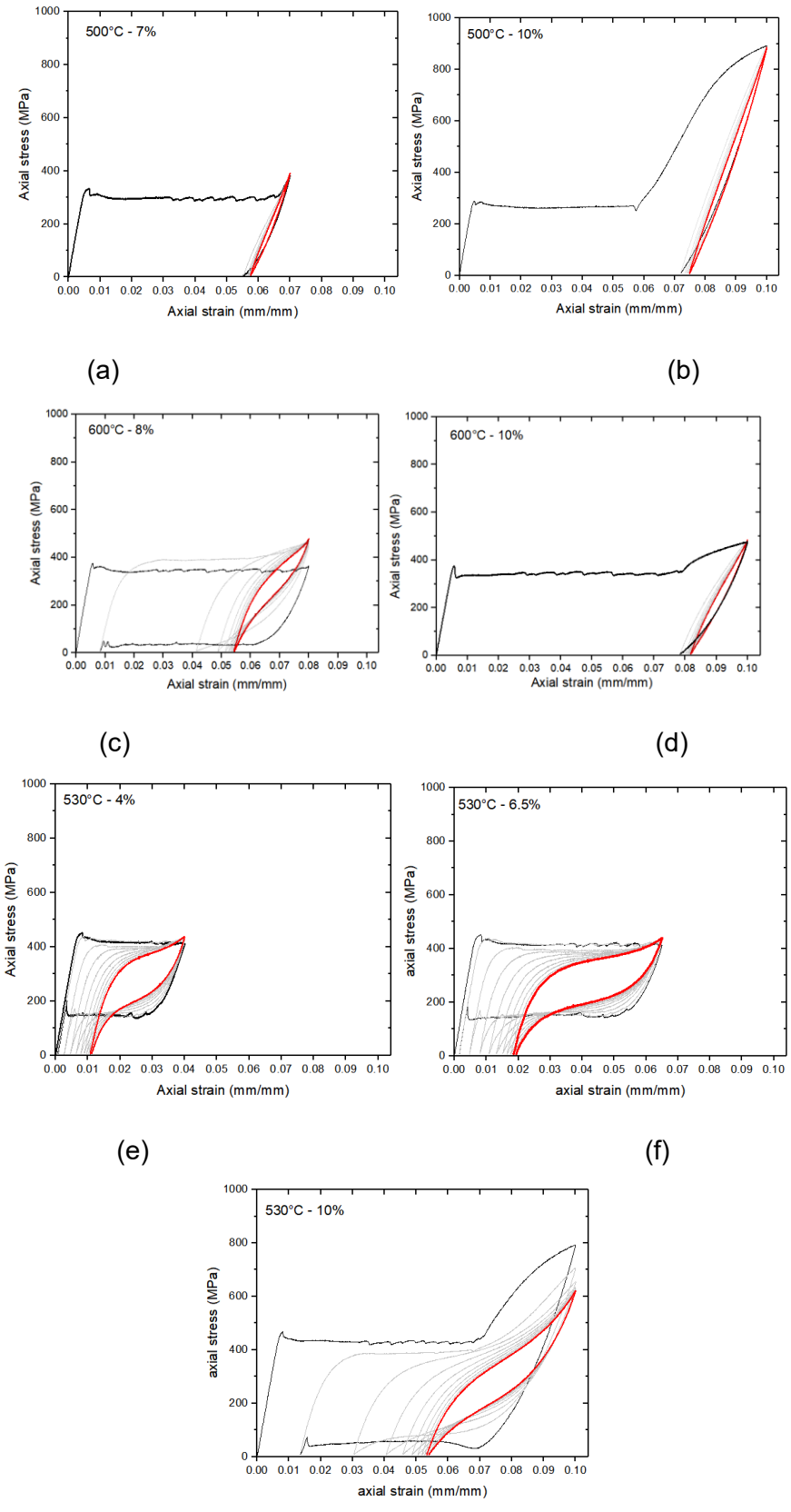


Figure 41 – Tensile test results: (a) 500°C – 7%, (b) 500°C – 10%, (c) 600°C – 8%, (d) 600°C – 10%, (e) 530°C – 4%, (f) 530°C – 6,5% and (g) 530°C – 10%

At 500°C treatment (Figure 41 (a) and (b)), there is no austenitic reverse transformation in both training strain levels, it can be associated with the A_f temperature above room temperature that indicate that the specimen is not completely austenitic (PANDOLFI *et al.,* 2020).

Comparison of specimens treated at 600°C reveals a distinct difference in phase transformation behavior between the two strain levels, as there is no austenite reverse transformation in the 10% strain training while austenitic transformation is presented in the 8% training in first cycle. In the first case, it can be associated with plastic strain. Also, the DSC result (Figure 38) indicates that at room temperature the specimen is completely austenitic as the A_f transformation temperature is below the room temperature (approximately 23°C).

For the 530°C-10 minutes heat treatment, there is always austenite transformation during unloading, it can be explained by the A_f transformation temperature being considerably lower than the room temperature (Figure 39). The 10% training (Figure 41 (g)) shows a higher residual strain when compared to 6,5% and 4% training strain. It can be associated with plastic residual strain.

Figure 42 presents the residual strain during unloading associated with TRIP. After 10 cycles all the specimens presented a variation below 5% that can be considered a stable condition after the training process. The specimens that presented low austenitic transformation during unloading present higher levels of residual strain (AR, 600-10%, 500-10%, 500-7%). The specimen 600-8% presented a low residual strain in the first cycle and high TRIP strain during the other cycles due to the reduction of the hysteresis loop. Specimen 530-10% presents a pseudoelastic hysteresis loop during all cycles and the TRIP strain was progressively stabilized. Other specimens (530-6.5% and 530-4%) presented lower levels of TRIP strain. These results provide complementary data to the results reported by CHEN *et al.,* (2023), as this reference compares the soaking times and different specimen geometries, while the results presented in this work compare temperatures and soaking times. The results also indicate that the soaking time has a greater influence than the temperature, however more tests are necessary for a more in-depth analysis.

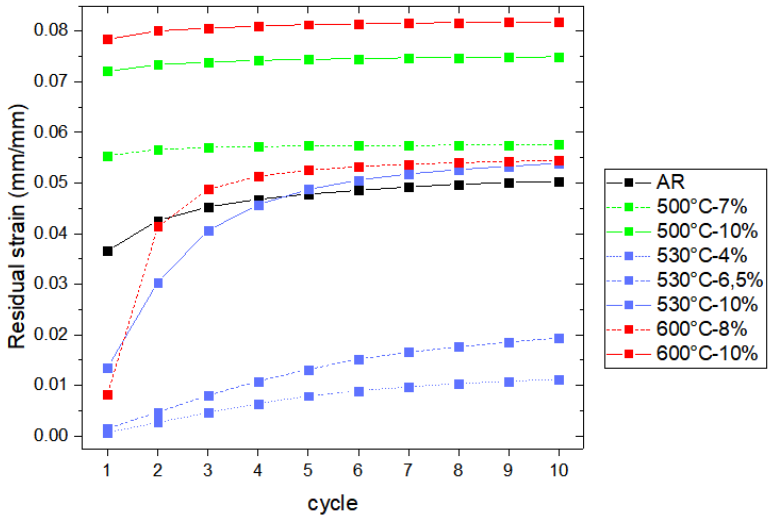


Figure 42 – TRIP results for different conditions (600°C – 10%, 600°C – 8%, 500°C – 10%, 500°C – 7%, 530°C – 10%, 530°C – 6,5% and 530°C – 4%)

The stress-strain curves for the 10th cycle of all the specimens are presented in Figure 43, where it can be observed that the heat treatment and the cyclic mechanical training affect considerably the pseudoelastic behavior of the material.

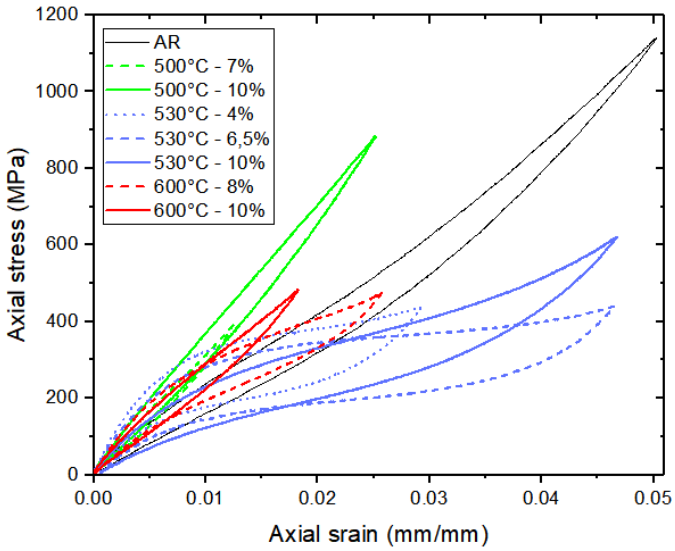


Figure 43 – Comparison of tensile results for the stabilized hysteretic loop. for different conditions (600°C – 10%, 600°C – 8%, 500°C – 10%, 500°C – 7%, 530°C – 10%, 530°C – 6,5% and 530°C – 4%)

The hysteretic dissipated energy developed during the stabilized cycle (10th), obtained from the curves show in Figure 43, is presented in Figure 44. The specimen heat treated at 530°C for

10 minutes and trained with 6,5% strain presents the largest value of dissipation. Although the curve does not have the larger maximum stress and/or strain values, it presents a larger hysteretic area. The hysteretic dissipation energy capability of the material, adopted in this work as the parameter to choose the optimal material condition, is an important characteristic of pseudoelastic components, such as those used in vibration reduction devices or structures (MOHAMMADGHOLIPOUR, BILLAH, 2023).

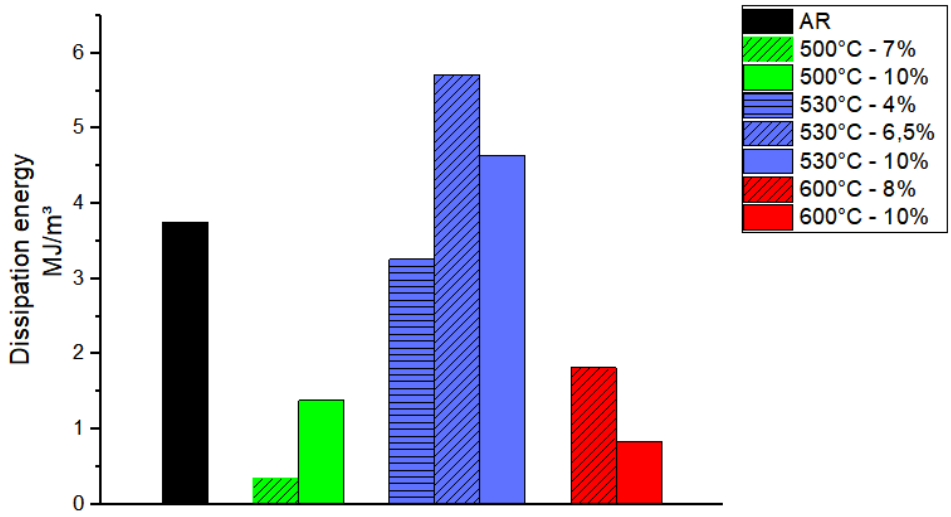
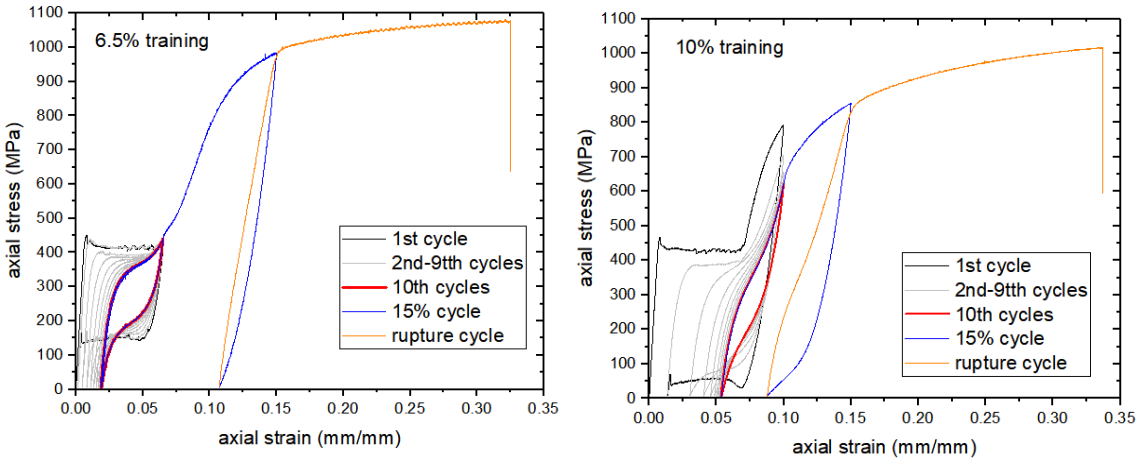


Figure 44 – Hysteretic dissipation energy for different heat treatment and training conditions for different conditions (600°C – 10%, 600°C – 8%, 500°C – 10%, 500°C – 7%, 530°C – 10%, 530°C – 6,5% and 530°C – 4%)

In order to study the combining effects of phase transformation and plasticity, an experimental scheme were executed consisting of 3 stages : 1) 10 cycles for training; 2) one cycle of prescribed strain applied until a value strain of 15% is reached, followed by unloading until the stress 7 MPa is reached, (a minimum stress limit is necessary to prevent the buckling of the test specimen); 3) loading applied until the fracture. Two training conditions were considered: 6.5% and 10%. The stress-strain curves of the complete test for the two conditions are presented in Figure 45.



(a) (b)

Figure 45 - Stress-strain curve: (a) 6.5% training, (b) 10% training of standardized (ASTM E8) specimens after heat treatment

Figure 46 shows the ASTM F-2516 test results for the specimen with the highest dissipated energy (530°C – 6.5%). The graphic shows a clear pseudoelastic plateau, during load and unload and a plateau in the second cycle at a higher level when compared to the first one due to the higher strain rate. The phase transformation process occurs through exothermic and endothermic processes that alter the material's temperature and, consequently, the critical stresses for phase transformation. Low loading rates reduce this effect, allowing heat exchange by convection with the environment, resulting in smaller temperature variations (MONTEIRO *et al.*, 2009; KUNDU, BANERJEE, 2022; REZAEE-HAJIDEHI *et al.,* 2025).

A comparison with the stress-strain curve for the AR condition(Figure 34), shows lower levels of stress, but a large strain capacity, as the rupture occurs at 39.8% while in the AR specimen occurs at 17.5%.

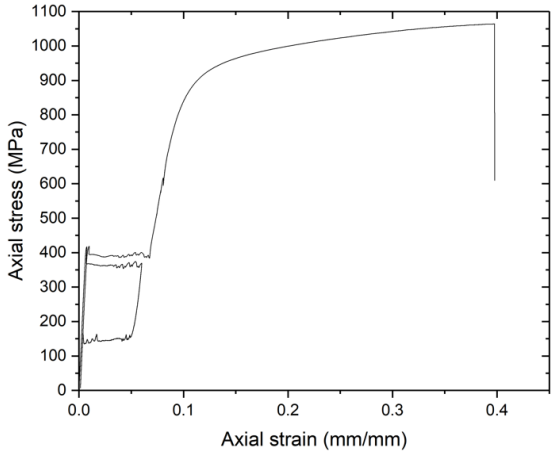
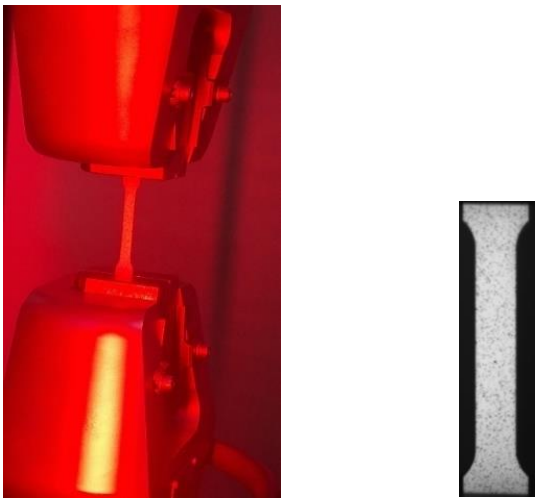


Figure 46 – ASTM 2516 test result for a specimen in the improved condition (heat treated at 530°C for 10 minutes and trained with 6,5% strain)

3.2.2.1. Digital Image Correlation

Digital Image Correlation (DIC) technique was used to study the effect of phase transformation on strain distribution during the loading and unloading. The specimen preparation requires the application of a white base coat followed by a random black speckle, necessary for the image processing. The image of an ASTM E8 specimen prepared for DIC analysis is present in Figure 47. The subset values were set to 15x15 pixels, and the images were processed using DIC replay software. The tests were performed on model 5985 universal testing system equipped with a 50 kN load cell at room temperature, using the Advanced video extensometer (AVE2) hardware (LAMAT - PPEMM/CEFET/RJ).



a) b)

Figure 47 – Tensile test using the DIC technique: a) specimen mounted in the test machine, b) specimen with speckle

The specimen heat treated at 530°C for 10 minutes and with 6.5% strain training was chosen and DIC results were evaluated at the first cycle. Figure 48 shows the stress-strain of the first cycle, and five DIC images obtained in the test are presented at different stages of the loading-unloading cycle.

The evolution of longitudinal strain distribution through the loading-unloading tensile test is represented in five instants, where the strain distribution observed indicate the following behavior: (a) initially the part is completely austenitic; (b) phase transformation begins in a preferential region in a Lüder´s band pattern; (c) the transformation front propagates to all the specimen interest area; (d) during unloading, the strain level decreases; (e) during further unloading the transformation band reduces to a localized region; (f) until be completely reversed to austenite. This behavior is consistent with results published in literature (CHEN *et al.*, 2023; ZHANG *et al.*, 2022; SHARIAT *et al.*, 2019; DELPUEYO *et al.*, 2021; LI *et al.*, 2023 a,b).

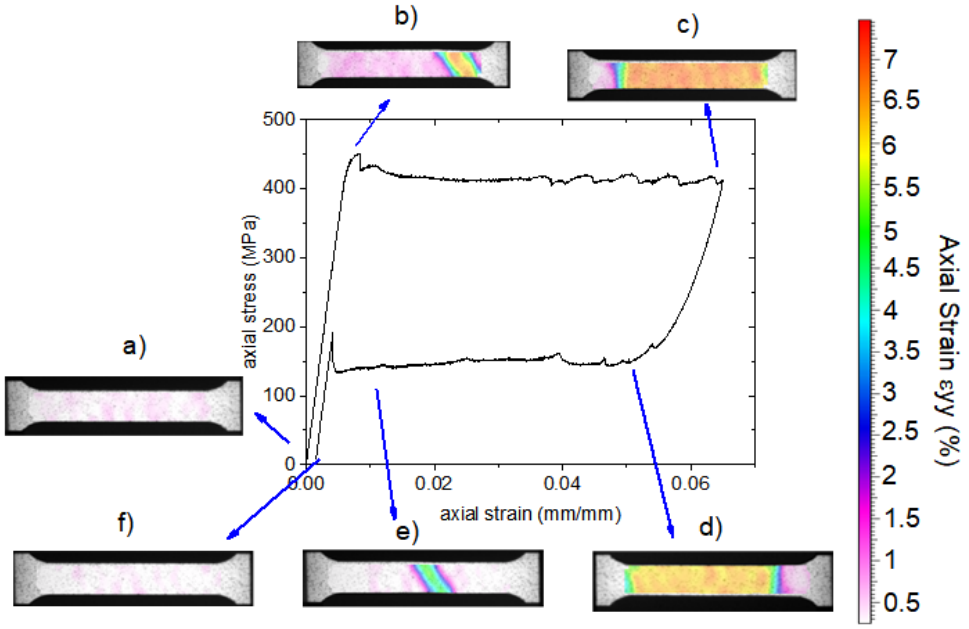


Figure 48 – Stress-strain curve of a specimen heat treated at 530°C for 10 minutes and 6.5% strain training. DIC results show axial strain associated with phase transformation at different stages

3.3. Tensile tests – plates with holes

To study the effect of phase transformation in pseudoelastic plates with holes, uniaxial tests were developed with three plates, with 100 mm length, 20 mm width and 1mm thick, contained central holes of 6, 9 and 12 mm. The specimens were cut by EDM (Electric discharge Machine) with the dimensions presented in Figure 49.

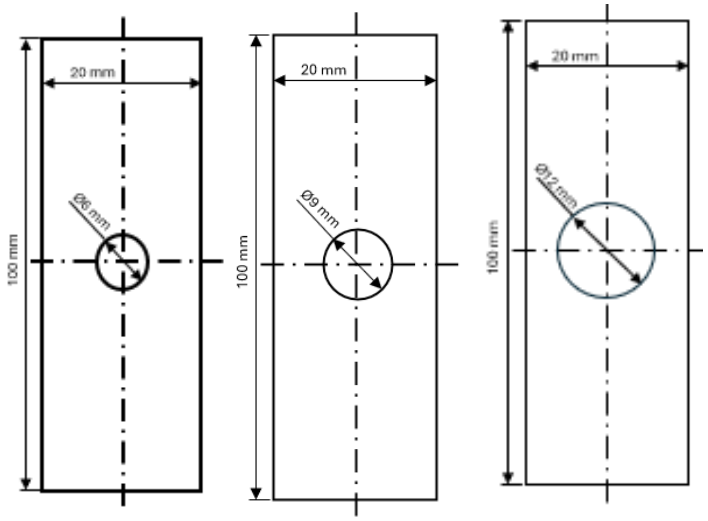
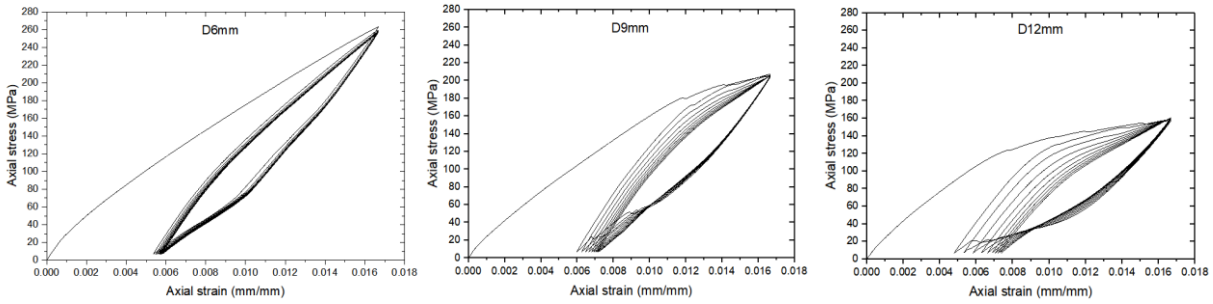


Figure 49 - Dimensions of specimens: a) D6 mm, b) D9 mm, c) D12 mm

3.3.1. Training

Prior to conducting tensile tests, the specimens were heat treated in the furnace at 530°C for 10 minutes as described in section 3.2. The experimental scheme was executed by applying to each specimen a sequence of quasi-static triangular waves at a rate of 1%/min (1.67 x 10^{-4} s^{-1}), with 1 mm displacement amplitude, followed by unloading until the stress 7 MPa is reached.

The samples were tested in an Instron model 5985 universal testing system equipped with a 50 kN load cell at room temperature (LAMAT - PPEMM/CEFET/RJ). The stress-strain curves obtained for the training process are present in Figure 50. It can be observed that the hysteretic loop decreases throughout the cycles, reaching a stabilized condition. It can be observed that, as the hole diameter increases, the net cross-sectional area and the global stiffness decrease, which explains the lower stress required to reach a given prescribed strain.



(a) (b) (c)

Figure 50 - Cyclic Stress-Strain Curves for the plates with hole diameters of: (a) 6mm, (b) 9mm, (c) 12mm

3.3.2. Digital image correlation and thermography

Tests were developed using both DIC and IR thermography. During the test, specimens were recorded by an optical camera Instron AVE 2 for the DIC method, and by an infrared camera FLIR A-320 to temperature measurement. The experimental setup is presented in Figure 51 (LAMAT - PPEMM/CEFET/RJ). The acquisition rates used were 0.5 Hz for the DIC, and 1 Hz for thermography.

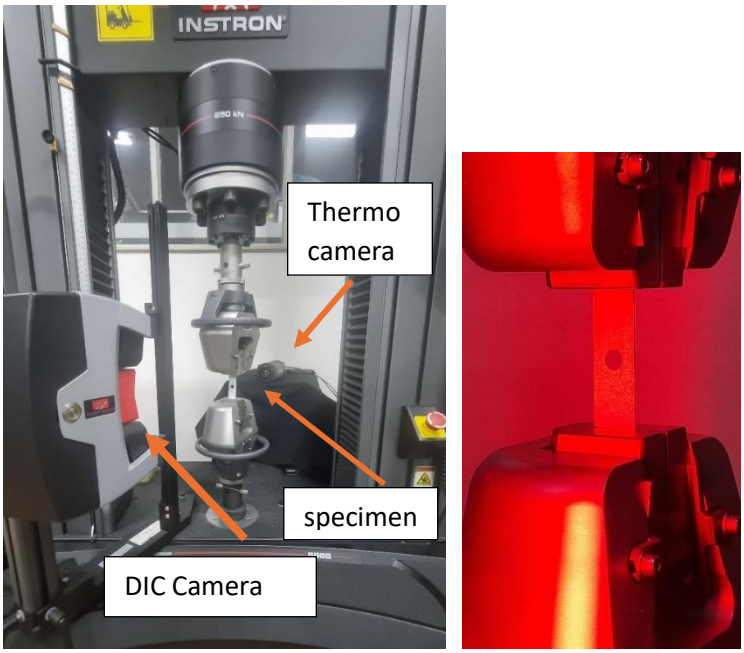
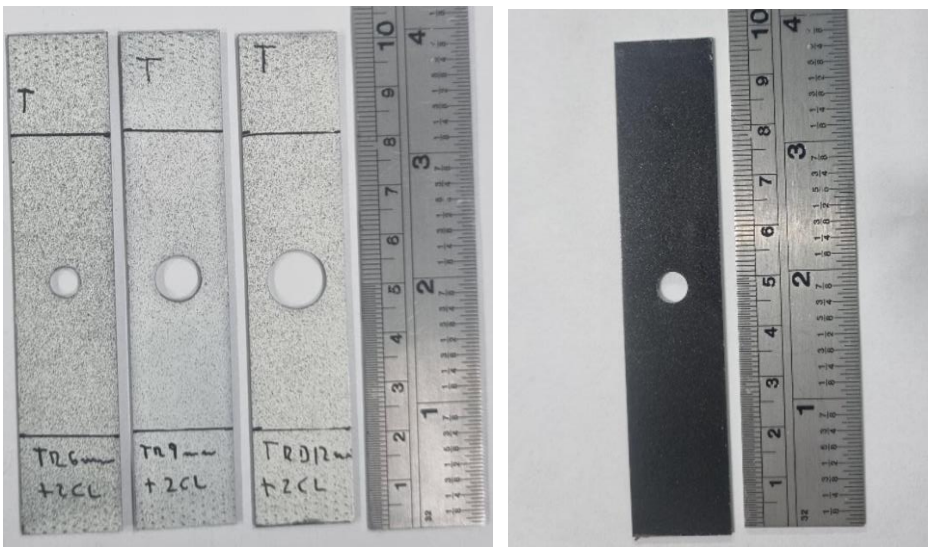


Figure 51 - Tensile test – experimental setup

After the training cycles used for material stabilization, two more cycles with the same load were performed to capture images for strain and temperature measurements. Digital Image Correlation (DIC) technique involves the painting of a write regular paint followed by a random black speckle necessary for the DIC processing, while the reverse face of the specimen was painted in black to improve emissivity for the infrared camera temperature measurement. The image of the specimens prepared for DIC analysis is present in Figure 52.

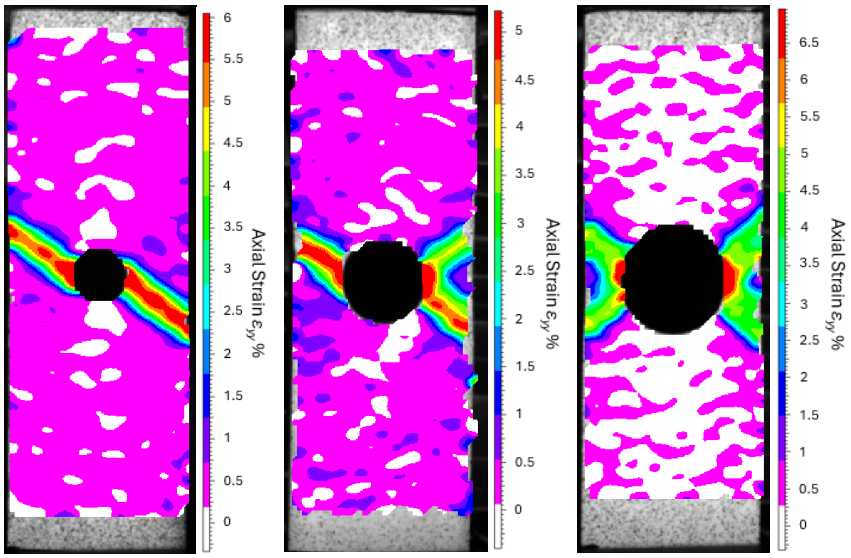


a) b)

Figure 52 – a) Specimen speckle surface, plates with hole diameters: 6mm, 9mm, 12mm b) black surface of 6mm specimen painted in black

The axial strain results of DIC are presented in Figure 53 for the maximum axial load displacement condition. Comparing the three hole diameters, it can be observed that in the 6 mm specimen the region of higher strain does not presents an “X” shape for maximum strains; instead, it develops maximum values along an inclined direction, which can be attributed to the formation of Lüders bands—localized strain bands (HE, 2023).

In the 9 mm specimen, although the inclined band begins to form in the second direction, it does not fully develop as in the 12 mm specimen. This behavior indicates a strain concentration phenomenon and suggests that a certain strain level is required to complete the phase transformation. From the beginning of the load application, stress concentration points form at the edge of the hole, but there is no austenite transformation. As the sample reaches a critical stress value, the phase transformation takes place.



a) b) c)

Figure 53 – Experimental axial strain for plates with hole diameters: (a) 6mm, (b) 9mm, (c) 12mm

Figure 54 presents the temperature variation along 10 cycles in 3 different specimen regions: (1) horizontal edge of the hole; (2) vertical edge of the hole; and (3) far from the hole. The results show that region 1 reaches higher temperature values during loading, indicating phase transformation, whereas during the unloading the temperatures reaches values below initial temperatures. Throughout the cycles the minimum temperature tends to increase due to the heat conduction-convection process that develops in the test specimen. This behavior is observed by other authors and is associated with the competition between the thermomechanical coupling

related to the exothermic/endothermic phase transformation processes present in SMAs and the convection process with the medium (MONTEIRO *et al.*, 2009; KUNDU; BANERJEE, 2022; REZAEE-HAJIDEHI *et al.,* 2025)

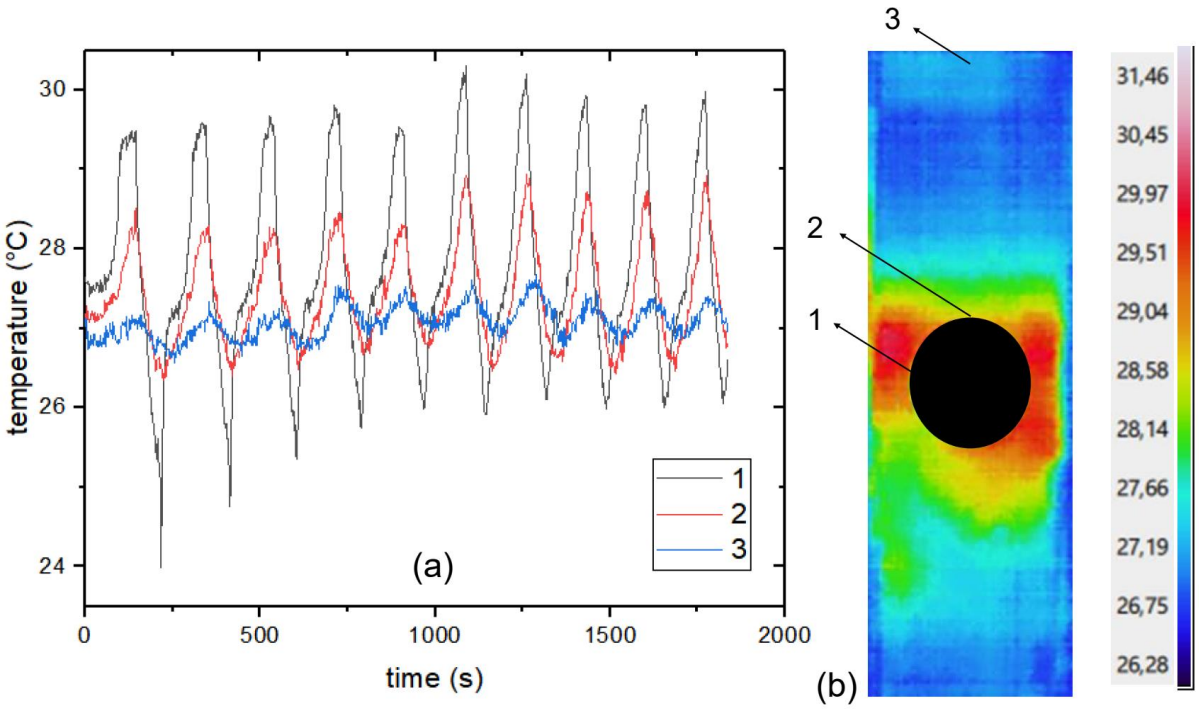
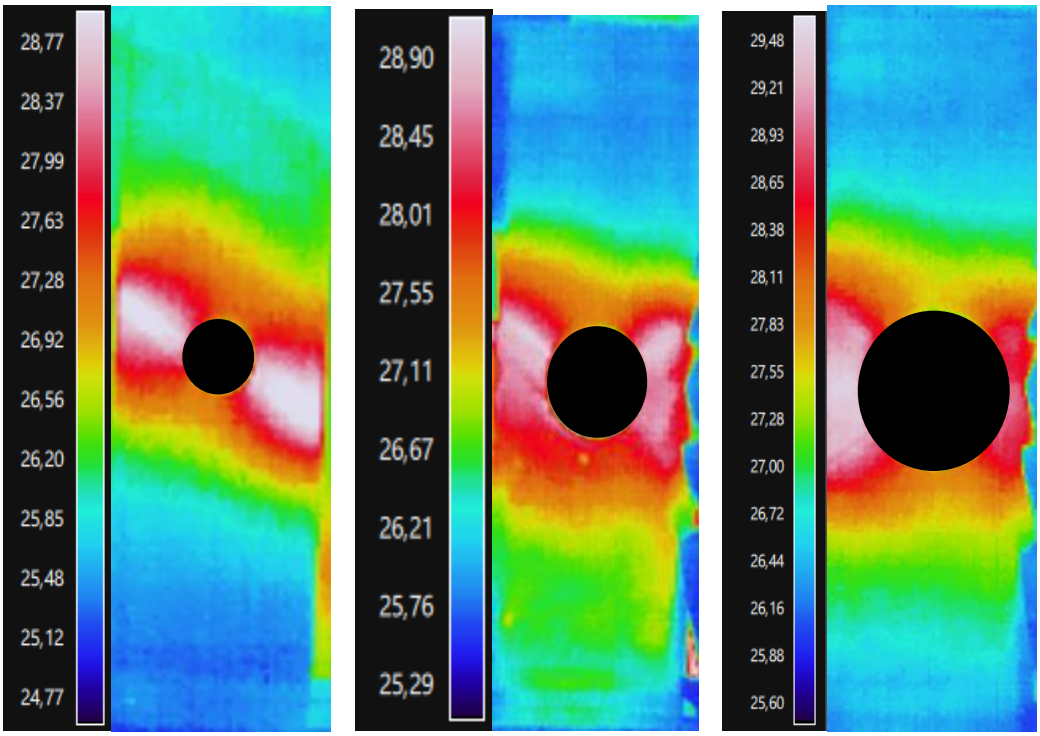


Figure 54 – Cyclic temperature variation in different specimen regions

Figure 55 shows the temperature distribution at the end of loading step. The result shows higher temperature values in the regions where phase transformation develops, and this is related to the thermomechanical coupling that promotes temperature variation during phase transformation. The temperature presents a variation around the holes, and its distribution is consistent with the observed strain distribution. The loading rate was chosen high enough, so the convection process is not sufficient to remove substantially the heat generated by the thermomechanical coupling. Therefore, the areas of higher temperatures can be associated with phase transformation regions.



(a) (b) (c)

Figure 55 – Temperature at the end of the loading for plates with hole diameters: (a) 6mm, (b) 9mm, (c) 12mm

Temperature-time evolution is presented in Figure 56 for plates with hole diameters of 6, 9 and 12mm, at two points: one point near the region of maximum strain and another far from the region of maximum strain. It is observed that in all cases, the temperatures near and far away from the holes are similar in the beginning of loading. Next, there is a rise in the values of temperature around the holes, especially in the location of maximum strain. This indicates the presence of phase transformation, since the austenite-martensite transformation is an exothermic process. During the unloading the near hole temperature decreases to values below the initial temperature, indicating the reverse phase transformation, as the martensite-austenite transformation is an endothermic process (DELPUEYO *et al.,* 2021).

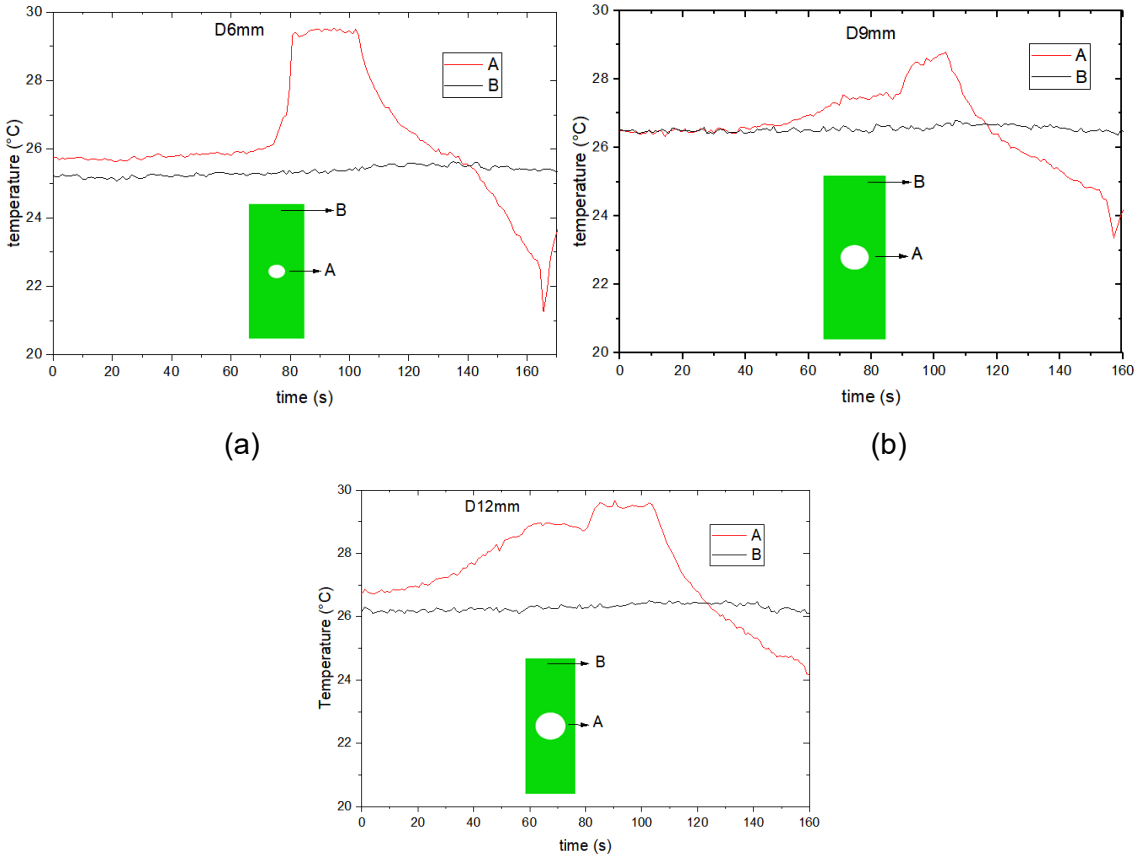


Figure 56 – Temperature evolution at two points: near the hole (point A) and far from the hole (pint B). Plates with hole diameters: (a) 6mm, (b) 9mm, (c) 12mm

4. NUMERICAL PROCEDURE

In order to further analyze the mechanical behavior of pseudoelastic thin sheets with stress concentrators, a numerical model based on the finite element method (FEM) is used. The analysis is performed in Abaqus software, using Auricchio´s constitutive model, a well-recognized model that is available in the software´s material library.

First, a calibration of the constitutive model is developed using the experimental data results presented in the last chapter for standard tensile tests. Next, results obtained from experimental data for plates with holes are used to verify if the model is able to capture the main behaviors.

4.1. Constitutive model (Auricchio)

To study the stress concentration phenomena of a pseudoelastic thin sheet with holes, a numerical model based on the finite element method is used. The Auricchio model (AURICCHIO, TAYLOR, 1997) was chosen to represent the pseudoelastic behavior of the material. It is a well-established model, which is available in several commercial software, such as Abaqus, Ansys, LS-Dyna (LECCE, 2015; DELPUEYO *et al.*, 2021; CISSÉ *et al.*, 2016); MOHAMMADGHOLIPOUR, BILLAH, 2021) and therefore can be applied in the study of complex geometries.

The model proposed by AURICCHIO, TAYLOR (1997) and AURICCHIO *et al.*, (1997) applies to isothermal pseudoelasticity in three-dimensional models, and uses the Drucker-Prager criterion to describe critical stresses for the pseudoelastic transformation (LAGOUDAS 2008).

The formulation, implemented in the Abaqus computational package, is based on the additive decomposition of strains, where the total strain is found by the sum of the elastic and phase transformation components (LECCE, 2015). The model considers traction-compression asymmetry and hardening (LECCE, 2015).

The constitutive model considers an initial austenitic state for a stress-free condition (ABAQUS, 2018). When a mechanical loading is applied, linear elastic behavior is observed until a critical stress is reached. The process of phase transformation occurs for higher stress levels promoting the variation of material properties that depend on phase volume fraction, as the Young

Modulus and the Poisson Ratio. As with several constitutive models, this model uses the rule of mixture to represent these properties, in the form described by the following equations:

$$E(\varsigma) = E_A + \varsigma(E_M - E_A) \quad (8)$$

$$\nu(\varsigma) = \nu_A + \varsigma(\nu_M - \nu_A) \quad (9)$$

where ς represents the martensitic volume fraction.

After complete transformation into the martensitic phase, the material returns to linear behavior associated with the properties of martensite. During unloading, the material has the opposite behavior. In the case of compressive loading, the constitutive model includes traction-compression asymmetry, therefore the critical transformation stresses are different in the two types of loading.

The typical stress-strain curve for the constitutive model, with critical stress values and transformation strain, is shown in Figure 57.

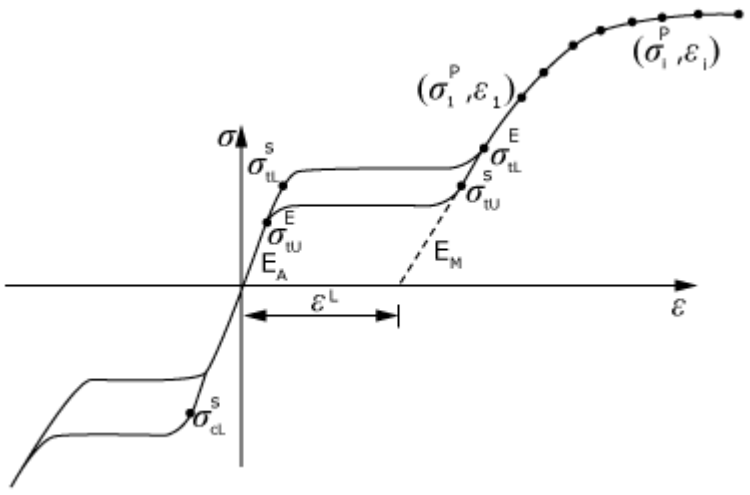


Figure 57 - Typical stress-strain curve of the Auricchio constitutive model (ABAQUS, 2018)

The constitutive equation for stress in isotropic materials can be represented according to the following equation:

$$\boldsymbol{\sigma} = \frac{E}{2(1+\nu)}\left[\left(\boldsymbol{\varepsilon} - \boldsymbol{\varepsilon}^{\boldsymbol{tr}} - \boldsymbol{\varepsilon}^{\boldsymbol{pl}}\right) + \frac{2\nu}{(1-2\nu)} tr\left(\boldsymbol{\varepsilon} - \boldsymbol{\varepsilon}^{\boldsymbol{tr}} - \boldsymbol{\varepsilon}^{\boldsymbol{pl}}\right)\right] \quad (10)$$

where $\boldsymbol{\varepsilon}$, $\boldsymbol{\varepsilon^{tr}}$, and $\boldsymbol{\varepsilon^{pl}}$ represents the total, phase transformation and plastic strains, respectively.

This model considers an additive decomposition, where the total strain component increment is composed of the sum of the elastic, phase transformation and plastic increment components:

$$\Delta\boldsymbol{\varepsilon} = \Delta\boldsymbol{\varepsilon^{el}} + \Delta\boldsymbol{\varepsilon^{tr}} + \Delta\boldsymbol{\varepsilon^{pl}} \tag{11}$$

The incremental strain for phase transformation depends on the incremental martensite volume fraction and the potential for flow transformation, G^{tr}:

$$\Delta\boldsymbol{\varepsilon^{tr}} = \Delta\varsigma\frac{\partial \boldsymbol{G^{tr}}}{\partial\boldsymbol{\sigma}} \tag{12}$$

The potential for flow transformation is given in the form of the Drucker-Prager model:

$$\boldsymbol{G^{tr}} = \boldsymbol{q} - \boldsymbol{p}\,tan\,\psi \tag{13}$$

where p is the hydrostatic pressure and q is the equivalent von Mises stress.

$$\boldsymbol{p} = -\frac{1}{3}tr\boldsymbol{\sigma} \tag{14}$$

$$\boldsymbol{q} = \sqrt{\frac{3}{2}\boldsymbol{S}:\boldsymbol{S}} \tag{15}$$

The transformation surface is given by the Drucker-Prager equation and varies linearly with temperature.

$$\boldsymbol{F^{tr}} = \boldsymbol{q} - \boldsymbol{p}\,tan\,\beta \tag{16}$$

The parameters β and ψ define the shape and flow direction of the material. The parameter β represents the inclination of the transformation surface, while ψ, on the other hand, appears in

the transformation potential function and corresponds to the dilatancy angle, which controls the volumetric tendency of the material during transformation flow.

Typical stress-temperature curves of the constitutive model are represented in Figure 58, showing that critical stresses depend linearly on temperature.

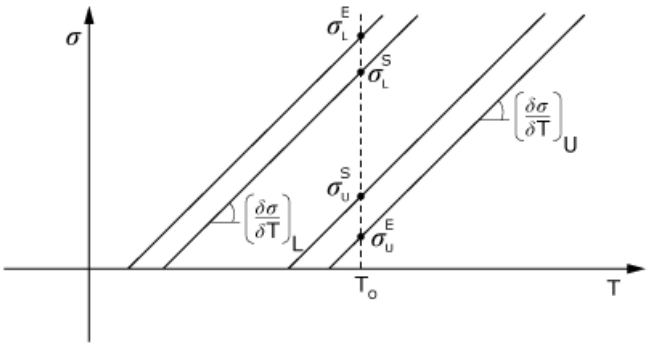


Figure 58 - Typical critical stress-temperature curve of SMAs (ABAQUS, 2018)

The increment in plastic strain is calculated using a nonassociated flow rule:

$$\Delta\boldsymbol{\varepsilon}^{\boldsymbol{pl}} = \Delta\bar{\boldsymbol{\varepsilon}}^{\boldsymbol{pl}}\frac{\partial \boldsymbol{G}^{\boldsymbol{pl}}}{\partial \boldsymbol{\sigma}} \tag{17}$$

where G^{pl} is the plastic flow potential, G^{pl} is equal to the Mises equivalent stress, q,

$$\boldsymbol{G}^{\boldsymbol{pl}} = \boldsymbol{q} \tag{18}$$

The yield surface, $\boldsymbol{F}^{\boldsymbol{pl}}$, is assumed to follow the Drucker-Prager formulation with hardening driven by the equivalent plastic strain, $\Delta\bar{\boldsymbol{\varepsilon}}^{\boldsymbol{pl}}$:

$$\boldsymbol{F}^{\boldsymbol{pl}} = \boldsymbol{q} - \boldsymbol{p}\tan\beta - \boldsymbol{F}^{\boldsymbol{Y}}\left(\Delta\bar{\boldsymbol{\varepsilon}}^{\boldsymbol{pl}}\right) \tag{19}$$

The initial yield stress is the stress at which the transformation of austenite into martensite ends, $\boldsymbol{\sigma}_{\boldsymbol{tL}}^{\boldsymbol{E}}$.

4.2. Model calibration – ASTM E8 specimen

A numerical model representing the tension test specimen was used to determine the parameters to be used in the finite element model. Figure 59 shows the mesh, obtained after a convergence analysis. Double symmetry conditions (in vertical and horizontal directions) and a 1 mm prescribed axial displacement loading applied at the specimen end (u_{22}) were adopted.

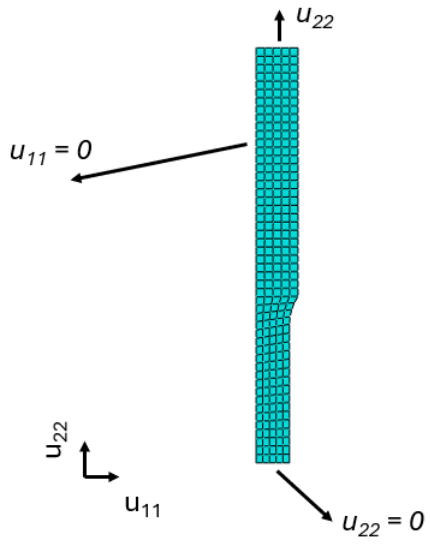


Figure 59 - FEM model with mesh, axial displacement prescribed load and boundary conditions

The constitutive model for isothermal pseudoelastic behavior has the possibility of including hardening effects for phase transformation process and plasticity. The determination of model parameters involves a fitting process of the experimental data (ADEODATO *et al.*, 2022) considering stress-strain curves for the 10th cycle, the 15% cycle and rupture cycle presented on Figure 45. The parameters of the constitutive model obtained are presented in Table 4 (phase transformation) and Table 5 (plasticity).

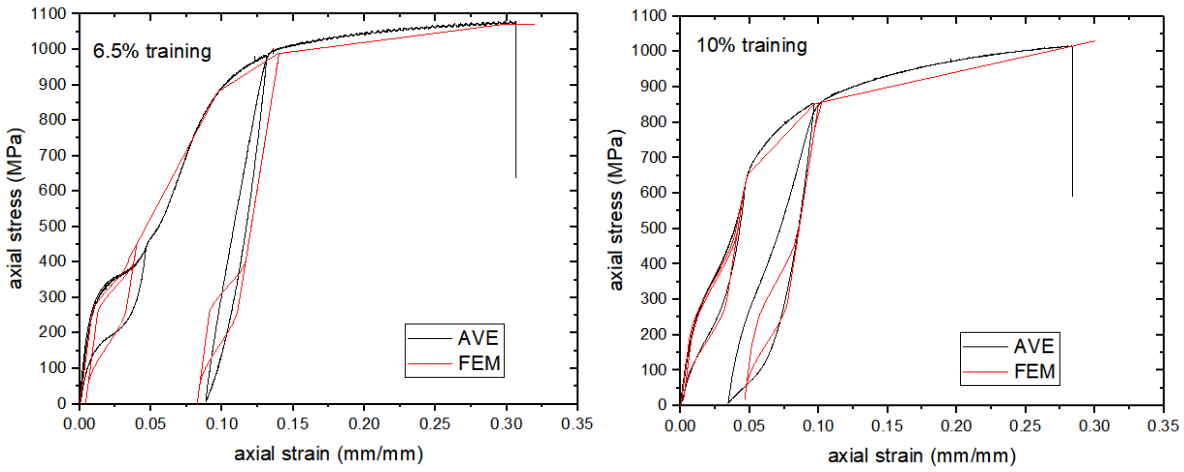
Table 4 - Parameters of the phase transformation constitutive model

Specimen	E_A (MPa)	ν_A	E_M (MPa)	ν_M	ε_r	σ_{tL}^S (MPa)	σ_{tL}^E (MPa)	σ_{tU}^S (MPa)	σ_{tU}^E (MPa)	σ_{cL}^S (MPa)
6.5% training	30180	0.3	25000	0.3	0.018	250	408	272	50	250
10% training	30180	0.3	25000	0.3	0.02	185	500	300	50	250

Table 5 - Parameters of the plasticity model

6.5% training		**10% training**	
S_y (MPa)	Total strain (mm/mm)	S_y (MPa)	Total strain (mm/mm)
745	0.08	673	0.05
880	0.10	853	0.10
1072	0.30	1030	0.30

Figure 60 shows a comparison between the stress-strain curves obtained from the numerical model and experimental data, where a good agreement is observed.



(a) (b)

Figure 60 - Comparison between the stress-strain curves obtained from the numerical model and the experimental data: (a) 6.5% training, (b) 10% training of standardized specimens after heat treatment

4.3. Finite element model verification – Plates with holes

For the stress concentration study, a quasi-static finite element model considering the material parameters obtained from experimental tensile tests with specimens was developed. For model simplification, double symmetry was employed. The mesh uses quadratic plane stress elements (CPS8), with a maximum step increment size of 0.002 (1/500) unitless time. The geometry was divided into different regions to facilitate the control of the discretization near the hole. A representation of the specimen with symmetry boundary conditions and the applied vertical loading displacement is presented in Figure 61*a*, where u_{11} stands for horizontal displacement and u_{22} for vertical displacement. The numerical model with ¼ symmetry were adopted for the presented analysis, after a prior verification with a full geometry representation. Displacement boundary conditions are applied to the left (fixed displacement in the horizontal direction) and lower (fixed displacement in the vertical direction) edges to represent the double symmetry condition. Figure 61*b* shows the meshes for the three hole diameters used in the experimental procedure, adopted after a convergence analysis.

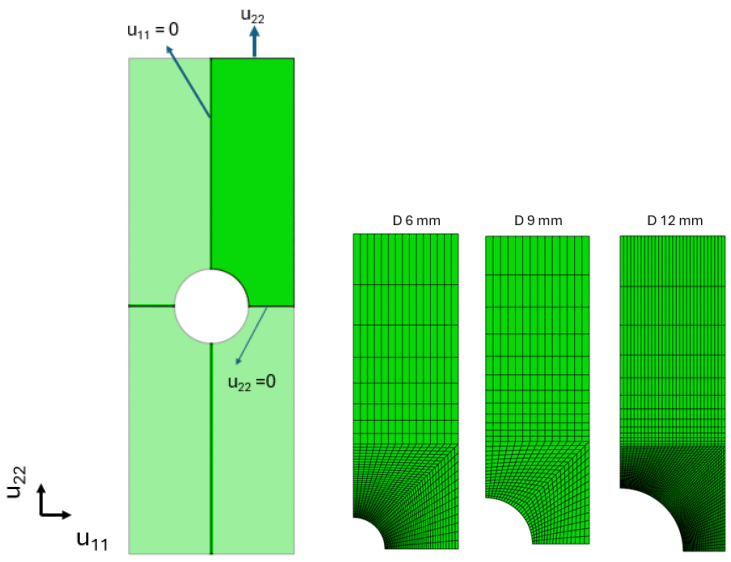


Figure 61 – FEM model with: (*a*) symmetry, boundary conditions and loading, and (*b*) meshes for three hole diameters analyzed

A triangular (linear) loading-unloading prescribed displacement is applied at the upper edge of the sheet in the vertical (axial) direction, with amplitudes (u_{22}) of 0.81, 0.74 and 0.76 mm (for hole diameters of 6, 9 and 12 mm respectively) and a total time duration of 2 (dimensionless time). The three prescribed displacements values were chosen to be equal to the displacement observed in the 10th cycle in the experimental results.

The force-displacement curves for numerical simulation and experiment data, considering the 3 hole diameters, are presented on Figure 62 showing a good agreement. The displacement was obtained in upper edge of the sheet in the vertical direction, and the force represents the reaction force at the lower edge of the sheet.

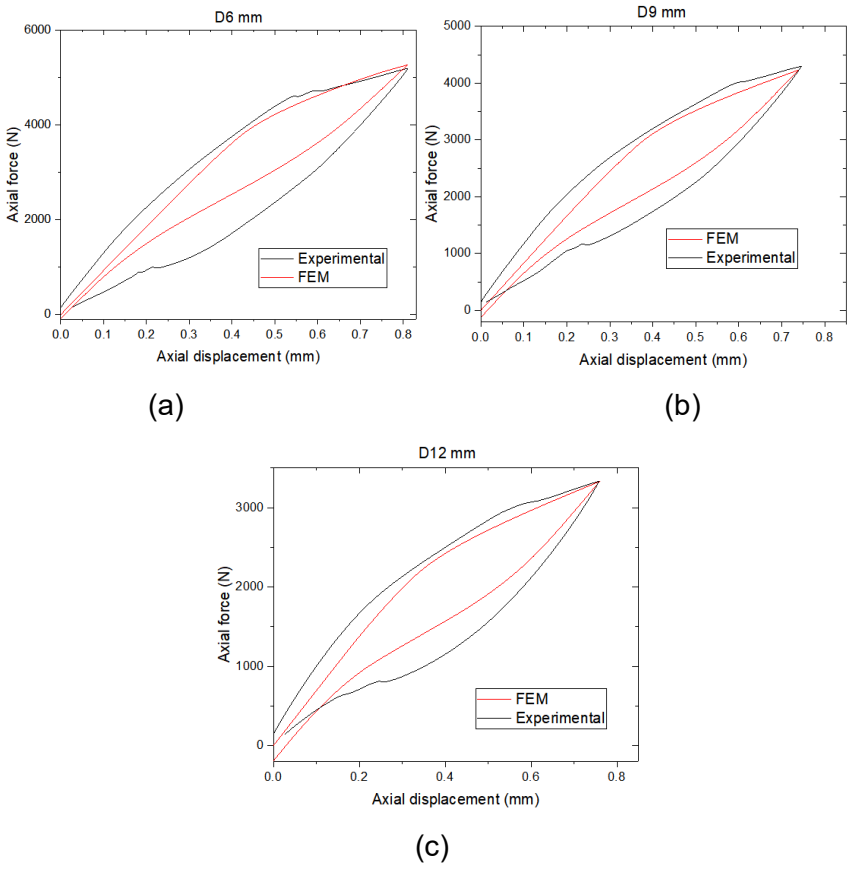


Figure 62 – Experimental and FEM axial force x displacement curves, plates with hole diameters: (a) 6mm, (b) 9mm, (c) 12mm

Figure 63 compare the distribution of the axial strain obtained from the numerical model and from the experimental data for different diameters. For all the conditions, despite similar strain distribution are observed, numerical results present higher maximum values than DIC results. The difference between the maximum values of FEM and DIC are 29%, 32% e 13% for diameters 6mm, 9mm and 12mm respectively. This is related to the resolution limitations of DIC method in regions with high gradients are present near borders, a characteristic reported by other authors (GONZALEZ *et al.*, 2010), combined with a lower resolution in comparison to the FEM results.

Although the FEM model consider double symmetry, the experimental results show a preferential direction of phase transformation consistent with Lüders band pattern. In 6 mm specimen, this transformation region occurs in a single direction, the 9 mm diameter specimens

show an incomplete transformation in the second direction, and the 12 mm diameter specimen has a “X” shape pattern. The formation of Lüders bands occurs due to local instabilities that can be preferentially activated by local heterogeneities present in real materials and geometric imperfections present in real mechanical components, which are not present in the developed numerical model.

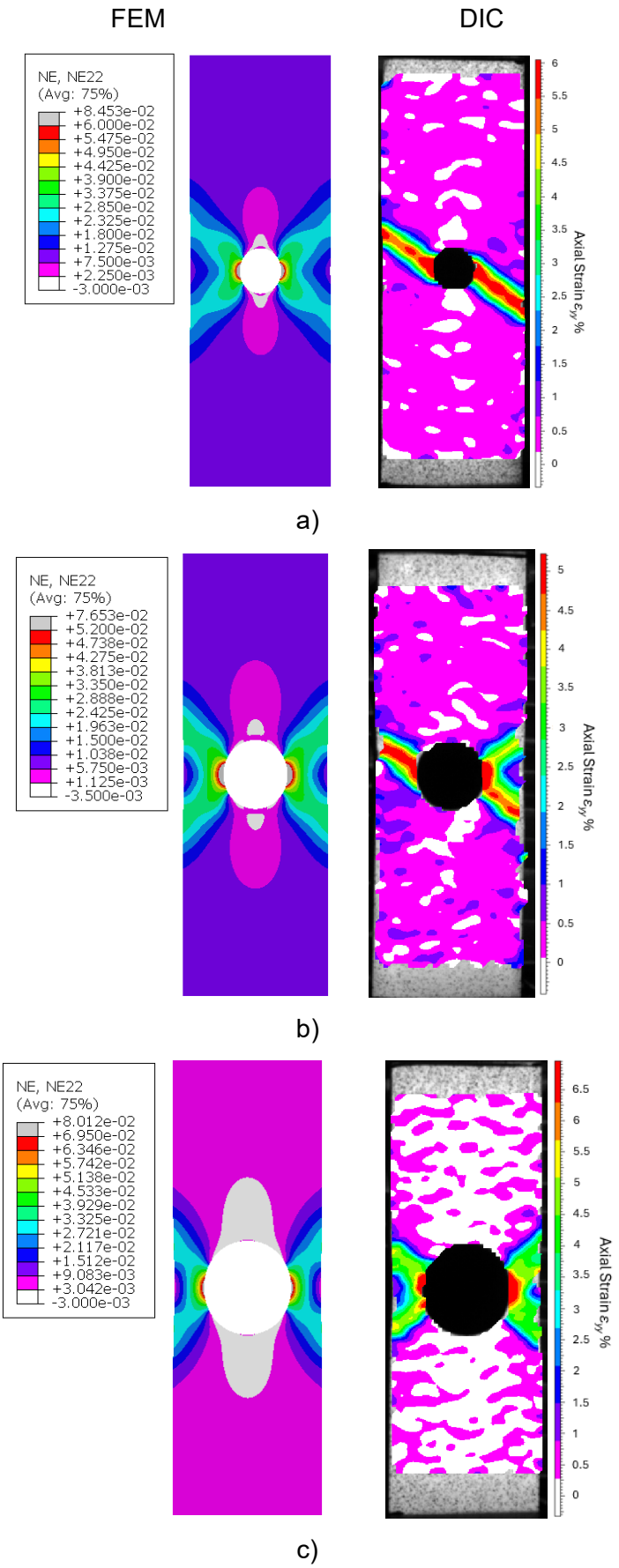


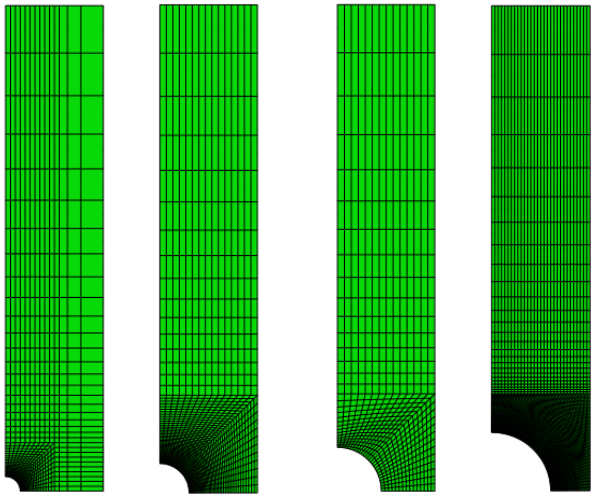
Figure 63 –Axial strain results obtained by the FEM model (left column) and experimental analysis (right column) for plates with hole diameters: (a) 6mm, (b) 9mm, (c) 12mm

5. FINITE ELEMENT ANALYSIS OF PLATES WITH HOLES

In this section, plates with holes are analyzed using the proposed finite element model to study the effects of phase transformation and plasticity on the stress concentration factors. Two material conditions associated with the training process are considered. Also, a plate with a 3mm hole diameter is included from previous section for further analysis.

5.1. Numerical analysis plates with holes

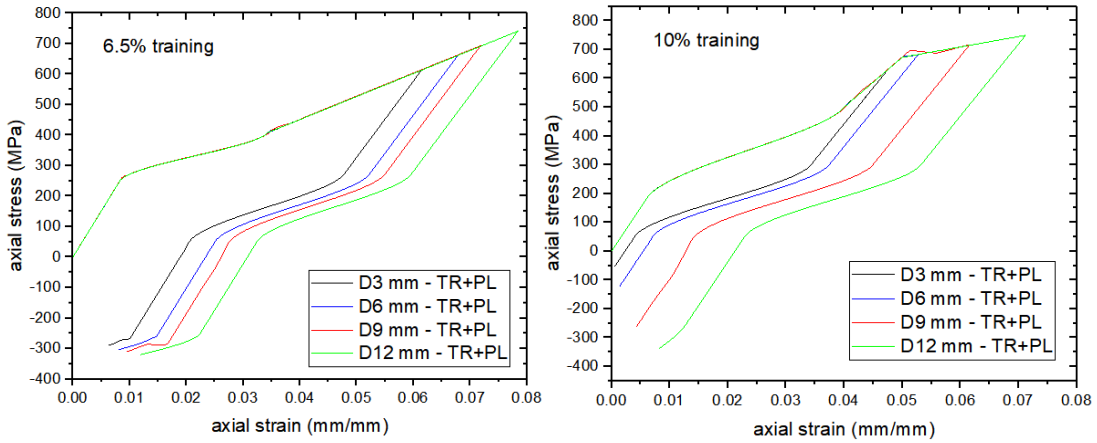
For the stress concentration study, a quasistatic finite element model of a plate with 20 mm width and 100 mm length containing a circular hole at its center were developed. Four different hole diameters are considered in the analysis: 3, 6, 9 and 12 mm. As in the previous chapter, for model simplification, double symmetry was employed. The mesh shown in Figure 64, obtained after a convergence analysis, uses quadratic plane stress elements (CPS8). A triangular (linear) loading-unloading prescribed displacement is applied at the upper edge of the sheet in the vertical (axial) direction, with an amplitude of 1 mm and a total time duration of 2 (dimensionless time). A ¼ of the geometry is considered by applying the following displacement boundary conditions to represent a double symmetry condition: fixed displacement in the horizontal direction at the left edge and fixed displacement in the vertical direction at the lower edge.



(a) (b) (c) (d)

Figure 64 - Mesh of the FEM model for different diameters: (a) 3mm, (b) 6mm, (c) 9mm, (d) 12mm considering a quarter geometry symmetry

Axial stress-strain curves for the two training conditions described in the last chapter (6.5 and 10%) considering phase transformation and plasticity (TR+PL) for all hole diameters obtained at the region of maximum axial stress, are presented in Figure 65. It can be noted that the conditions for 6.5% training strain cycles have lower strain values compared with the ones of the same diameter for 10% training. Higher values of residual stress after unloading are observed for 6.5% training conditions particularly in smaller diameters, whereas similar values are observed for diameter of 12 mm.

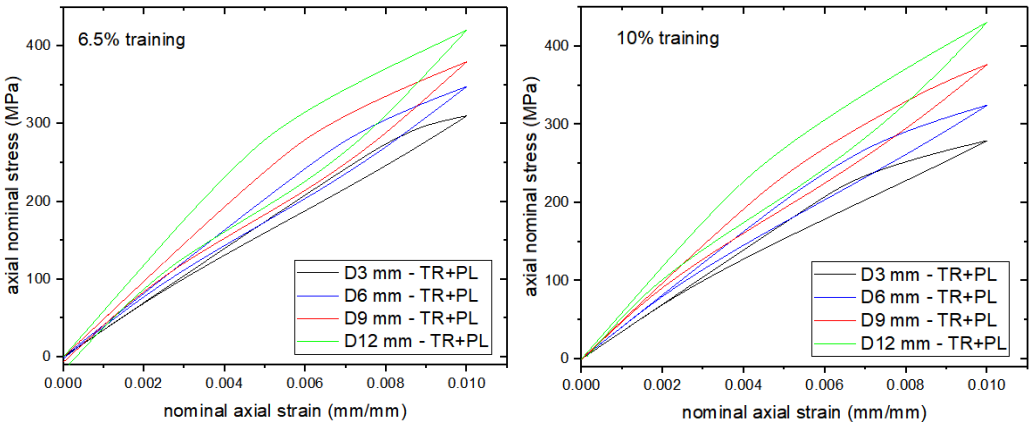


(a) (b)

Figure 65 - Axial stress-strain curves for the local of maximum stress for plates with different hole diameters: (a) 6.5% training, (b) 10% training

Figure 66 compare the axial nominal stress-strain curves of the 4 different hole diameters for the 2 different training conditions. For the smaller diameters (3 and 6 mm) the 6.5% training

presents smaller values due to small critical stress that initiate phase transformation. For 9 and 12 mm diameters, the results are similar between both training conditions.



(a) (b)

Figure 66 - Axial nominal stress-strain curves for plates with different hole diameters: (a) 6.5% training, (b) 10% training.

Axial stress distribution obtained with the model at the end of the loading stage (dimensionless time equal to 1) is presented in Figure 67 for 6.5% (a-d) and 10% (e-h) training conditions, respectively. It is possible to observe that the stress values near the point of maximum stress are higher for parts with larger diameters.

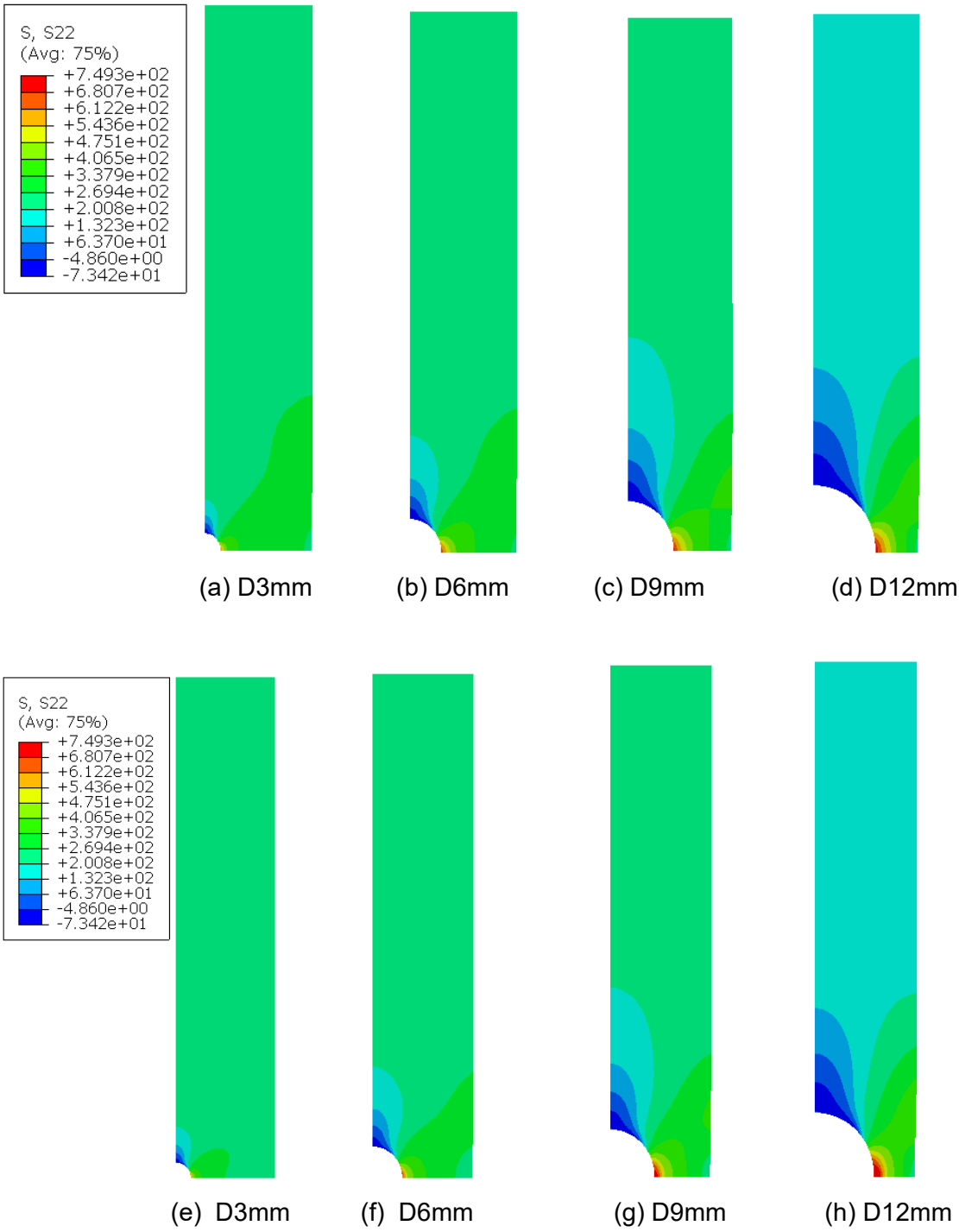


Figure 67 - Axial stress distribution (in MPa) for plates with different hole diameters at the end of the loading stage: 6.5% training (a-d) and 10% (e-h).

The distribution of martensite volume fraction at the end of the loading (dimensionless time equal to 1) is present in Figure 68 and for 6.5% (a-d) and 10% (e-h) conditions, respectively. It can be observed that the region experiencing martensitic transformation expands as the hole diameter increases, this is related to the stress distribution around the hole.

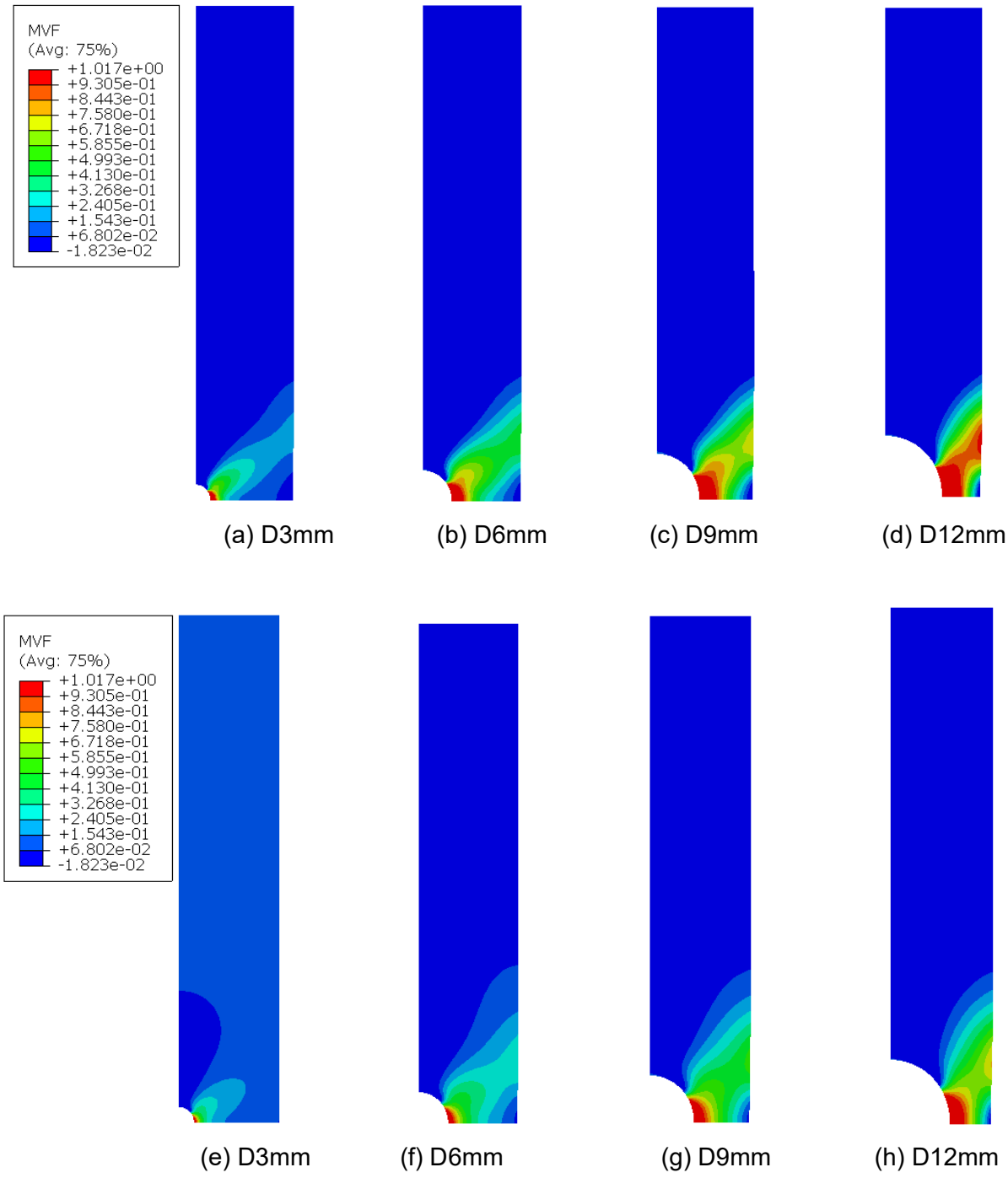


Figure 68 - Martensite volume fraction distribution for plates with different hole diameters at the end of the loading stage: 6.5% training (a-d) and 10% (e-h).

Axial total strain at the end of the loading stage is present in Figure 69 for 6.5% (a-d) and 10% (e-h) training conditions, respectively. As the previous results, the strain distribution region around the hole increases as the diameter increases.

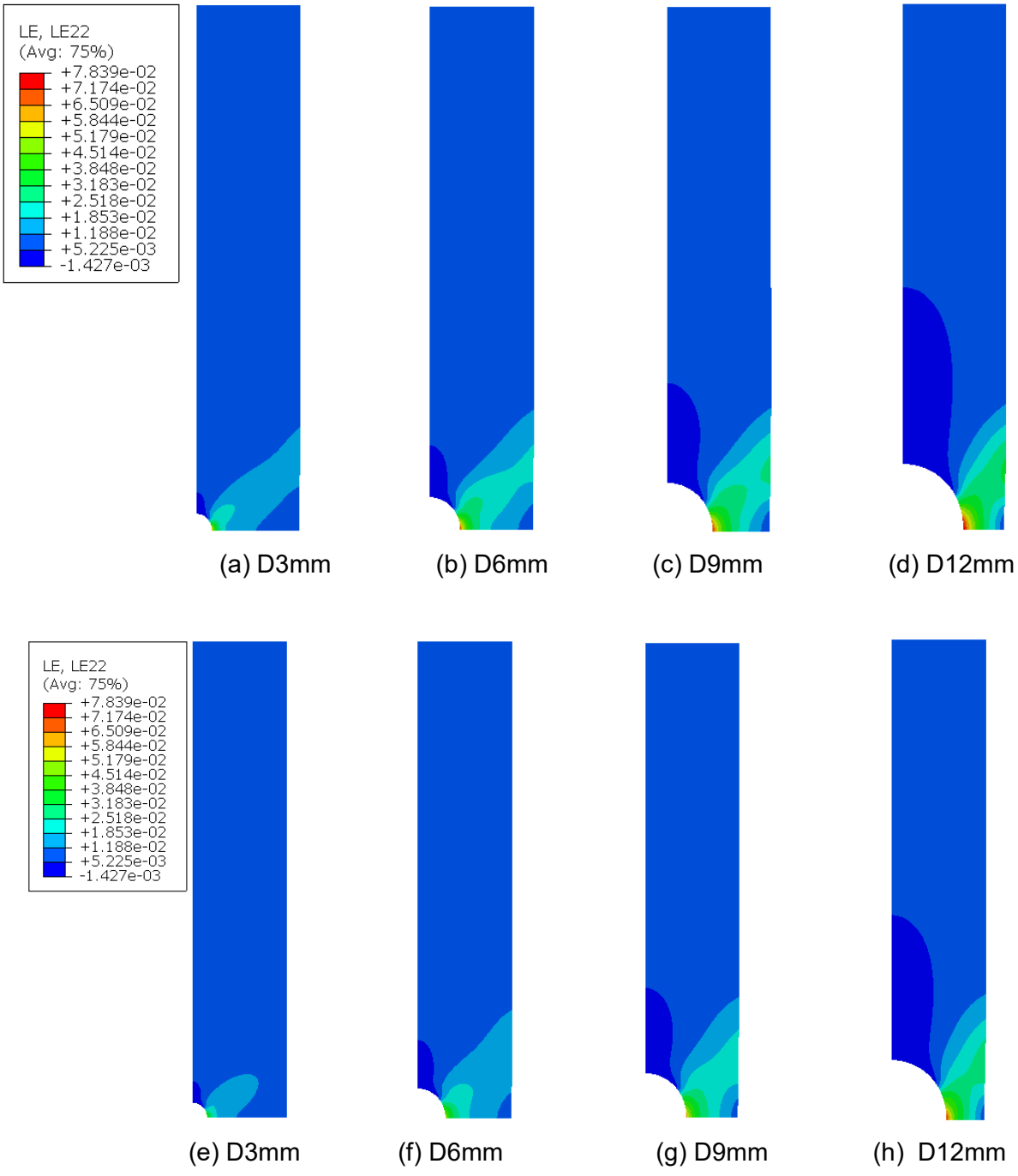


Figure 69 - Axial total strain distribution for different diameters at the end of the loading stage: 6.5% training (a-d) and 10% (e-h).

At this point, to study the influence of plasticity, two scenarios were analyzed: a case with phase transformation (TR) and a case with both phase transformation and plasticity (TR+PL). The

plasticity behavior is included in the analysis for the (TR+PL) scenario by activating the plasticity constitutive model in the Abaqus finite element package. The stress-strain curves for both cases at the point of maximum axial stress are presented in Figure 70 for a typical condition: 10% training, 9mm hole diameter, 1 mm displacement (SILVA *et al.*, 2024a). It can be observed that the curve, considering only phase transformation (TR), develops higher stress levels and lower strain values. In the case with phase transformation and plasticity (TR+PL), the plastic strain contributes to amplify the stress redistribution and a localized reduction in the stress is observed. Additionally, the curve for the case with plasticity exhibits residual compressive stress upon unloading, a characteristic behavior associated with displacement-controlled tests with the presence of plastic strain.

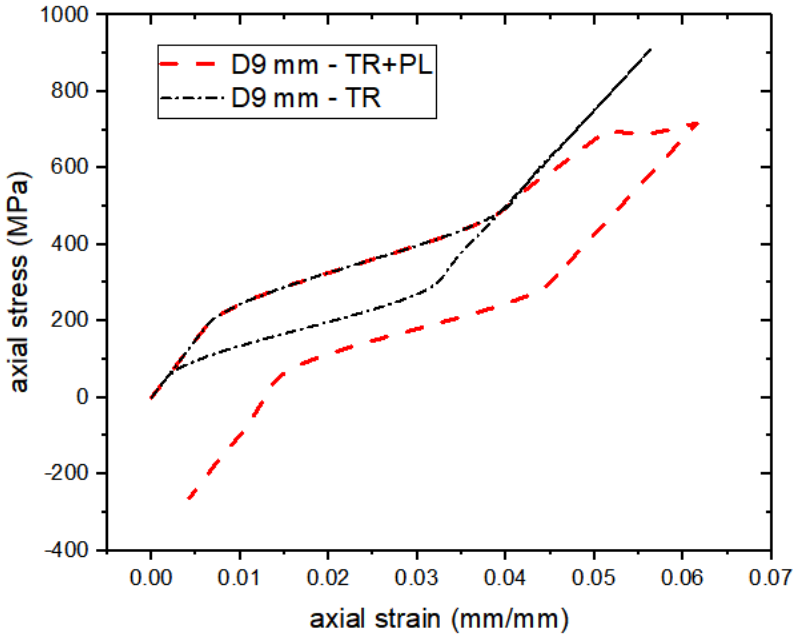
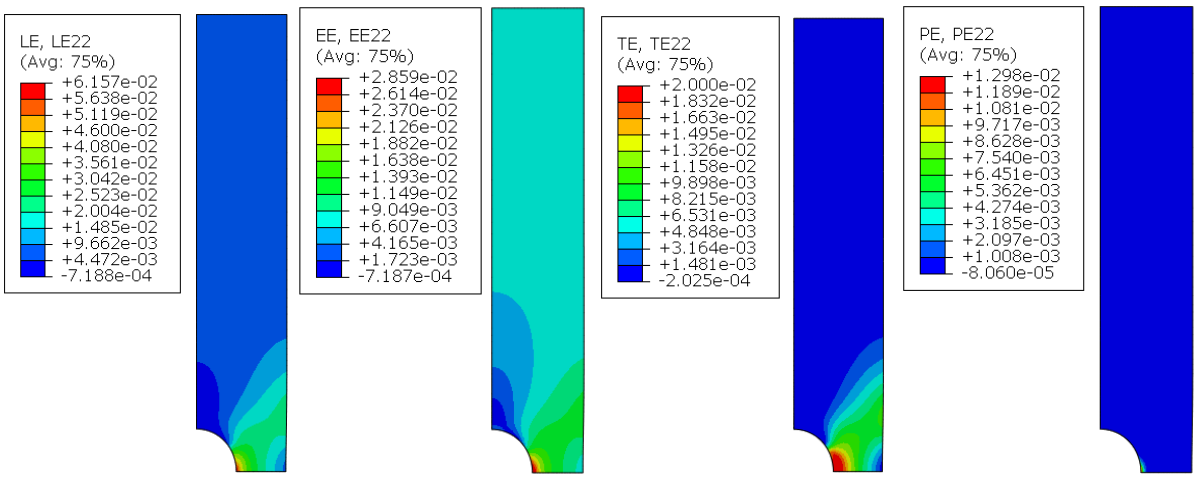


Figure 70 - Stress-strain curves at region of maximum axial stress: case with phase transformation (TR) and case with phase transformation and plasticity (TR+PL) for plates with 9mm hole diameter and 10% strain training

The distribution of total strain and the components of elastic, phase transformation, and plastic strain at the end of loading stage for the case considering phase transformation and plasticity are presented in Figure 71. It can be noted that the phase transformation strain is lower than the elastic component. Furthermore, it is observed that the plastic strain (1.3%) is the smallest of the components analyzed and is confined to a very small region.



(a) (b) (c) (d)

Figure 71 - Axial strain distribution at the end of the loading stage for plates with different hole diameters: (a) total, (b) elastic, (c) phase transformation, (d) plastic

Figure 72 presents the time evolution of axial stress result (S22), martensite volume fraction (MVF) and axial plastic strain (PE22) during the loading stage (time equal to 1) at the edge of the hole for the typical condition previously analyzed (diameter of 9 mm with 10% training strain). It can be noted that at time instant of 0.18, the phase transformation process initiates, promoting the reduction in the rate of stress increase. In time instant of 0.68, the plastic strain evolution initiates, and promotes a further reduction in the rate of stress increase.

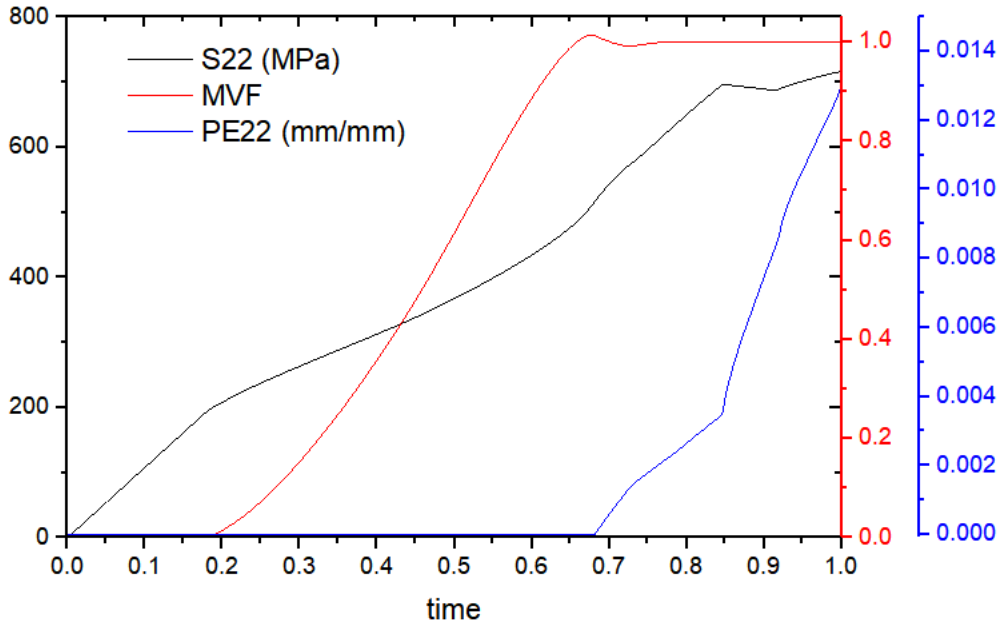
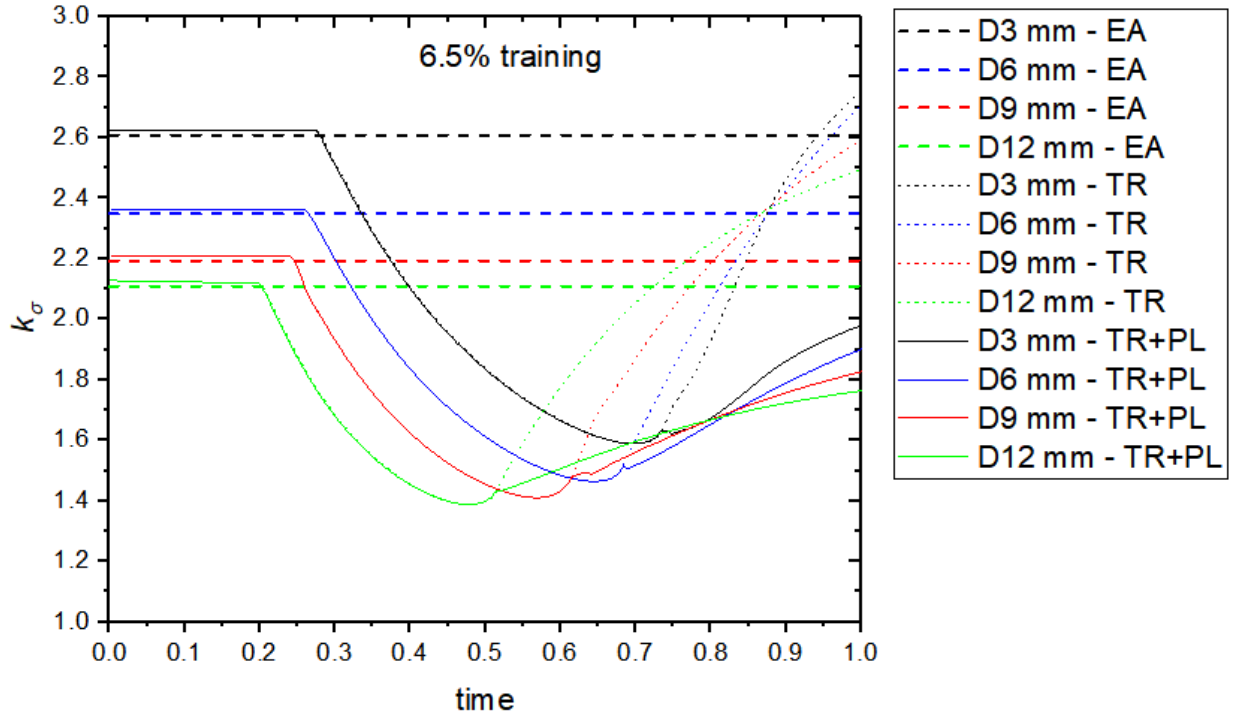


Figure 72 - Time evolution of the axial stress result (S22), martensite volume fraction (MVF) and the axial plastic strain (PE22) during loading stage at the edge of the hole (diameter of 9mm with 10% training strain)

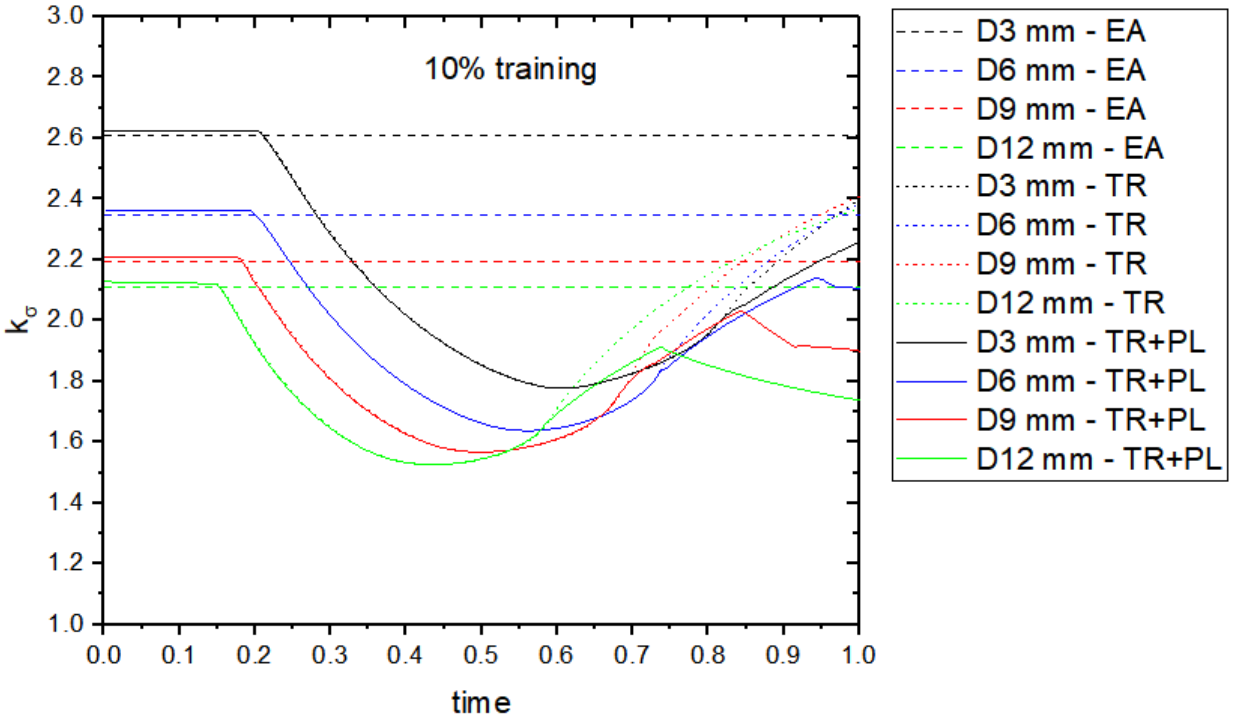
5.2. Stress concentration factor

The evolution of the stress concentration factor throughout loading for the elastic analytical case (EA), calculated by Eq. (5), and for the cases considering phase transformation (TR) and phase transformation and plasticity (TR+PL) is shown in Figure 73 for 6.5% and 10% training conditions.

It can be observed that at the beginning of loading, while the phase transformation process has not yet initiated, and the specimen is fully austenitic, the value of the K_σ is close to the one estimated by the analytical model for the elastic case. As the load increases, phase transformation initially develops in the region of maximum stress (time instant of 0.18 for diameter 9 mm with 10% training strain), resulting in martensite formation in that region while the rest of the specimen remains in the austenitic phase. This phase transformation leads to stress redistribution in the region near the hole and, consequently, a reduction in the value of K_σ. When martensitic phase transformation develops in the rest of the specimen, K_σ starts to increase again. Yielding promotes a second stress redistribution (time instant of 0.68 for diameter 9mm with 10% training strain), and the curves begin to differentiate. For the case considering only phase transformation, K_σ values continue to increase, while the curve for the case considering phase transformation and plasticity shows a reduction in the K_σ value after the onset of yielding.



(a)



(b)

Figure 73 - Evolution of the stress concentration factor during loading for plates with different hole diameters: (a) 6.5% training, (b) 10% training

Results shown in Figure 73 indicate that plasticity leads to a reduction in the stress concentration factor due to stress redistribution caused by the plastic strain near the hole. This result is consistent with results obtained by other authors (HOSSEINI AND ASHRAFI, 2023). It can be noted that in comparison with the 6.5% training, the TR+PL results for the 10% training condition show a decrease in K_σ for hole diameters of 6, 9 and 12 mm after the plastic strain takes place. This behavior is associated with the yielding that occurs due to the larger stress levels reached for these three conditions.

The stress concentration evolution curves obtained from the numerical simulations shown in Figure 73, indicate an influence of the training strain on the K_σ factor value. Figure 65 shows that higher stress levels are observed for the 10% training level, and yielding occurs at a lower strain level. Additionally, the variation in K_σ is found to be comparatively smaller under this condition. This suggests that the training strain plays an important role in determining the mechanical behavior of the material, particularly in terms of stress distribution. At the end of loading stage, K_σ values for the TR+PL curves are consistently lower than those for the TR curves due to the effect of plasticity.

For the case considering phase transformation and plasticity (TR+PL), the 6.5% training shows final K_σ values at the end of the loading stage from 1.76 (D12 mm) to 1.98 (D3 mm), while for 10% training final K_σ values at the end of the loading stage go from 1.74 (D12mm) to 2.26 (D3 mm). For the case considering only phase transformation (TR), larger values are observed: between 2.5 and 2.7 for 6.5% training and from 2.3 to 2.4 for 10% training.

In the same way as observed for an elastic condition, the diameter of the hole influences the K_σ value, with larger diameters promoting lower K_σ values. The phase transformation promotes the reduction of the K_σ value in the beginning of the phase transformation process. A recovery of the K_σ value is observed when a larger portion of the part experiences phase transformation, followed by a subsequent reduction after yielding.

The results show that the training process can also affect the K_σ value, as the strain amplitude applied during training can modify the hysteresis and TRIP behaviors and, therefore, the stress distribution. When comparing the values obtained for 6.5% and 10% training strain, the smallest difference between the K_σ values is observed for the hole diameter of 12 mm (+1.2%), while the largest difference is observed for the diameter 3 mm (-12.4%).

It is important to mention that in displacement-controlled tests, the longitudinal force depends on specimen global stiffness. Also, the nominal stress is influenced by the remaining area (net area at the smaller cross section). Therefore, as the hole diameter increases the force necessary to reach a specific displacement is lower because of the lower global stiffness, but the net area is smaller, producing two concurrent effects. The results presented an increase in the maximum

nominal stress, as the hole diameter increases while the force decreases, indicating that the cross-sectional area has a greater influence.

Plasticity has a significant effect on the K_σ factor, with plastic strain leading to a reduction in the K_σ value. This reduction is attributed to material softening following yielding, which attenuates the increase in K_σ associated with phase transformation.

In addition to K_σ results presented in Figure 73, other criteria are analyzed. Figure 74 show K_ε and K_t results for 6.5% training and Figure 75 show the same results for 10% training.

Strain concentration factors (K_ε) provides a measure of how much the maximum strain exceeds the purely elastic prediction, due to the phase transformation process, which induces significantly higher deformation levels, while K_σ provides a measure of how the maximum stress differs from the purely elastic case, since the phase transformation process redistributes the stress field and reduces local peak values.

Numerical values related to strain concentration factors (K_ε) according to eq. 3 is presented, it can be noted that as to the the hole diameter increase, larger K_ε values are observed. This is due to the increase of maximum strain values associated to a small area for larger diameters. In the beginning the the load, the value is constant, after the values experiences a first increase, in a third momet the curve suffer another change in the slope that is related to beginning of plastic strain.

Considering its potential use in mechanical design, the Neuber criterion may be considered as appropriate, since it provides an intermediate estimate between the stress and strain concentration factors (K_σ and K_ε), this is consistent with Neuber´s original proposal (Neuber, 1961), and used in other inelastic materials (MEGGIOLARO *et al.*, 2016) for mechanical design.

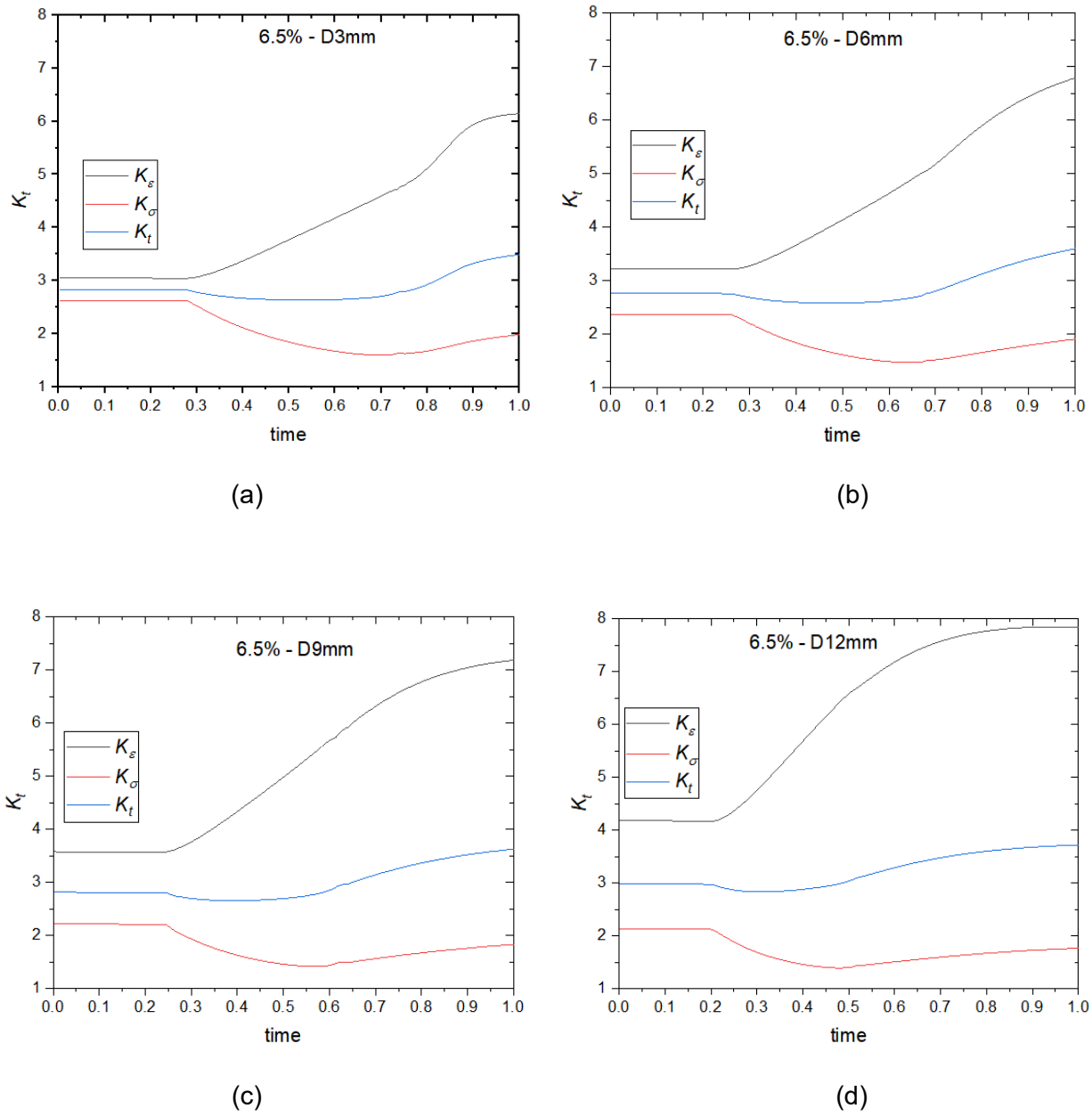


Figure 74 – Stress, strain and Neuber concentration factors for 6.5% training: a) D3 mm b) D6mm, c) D9mm, d) D12mm

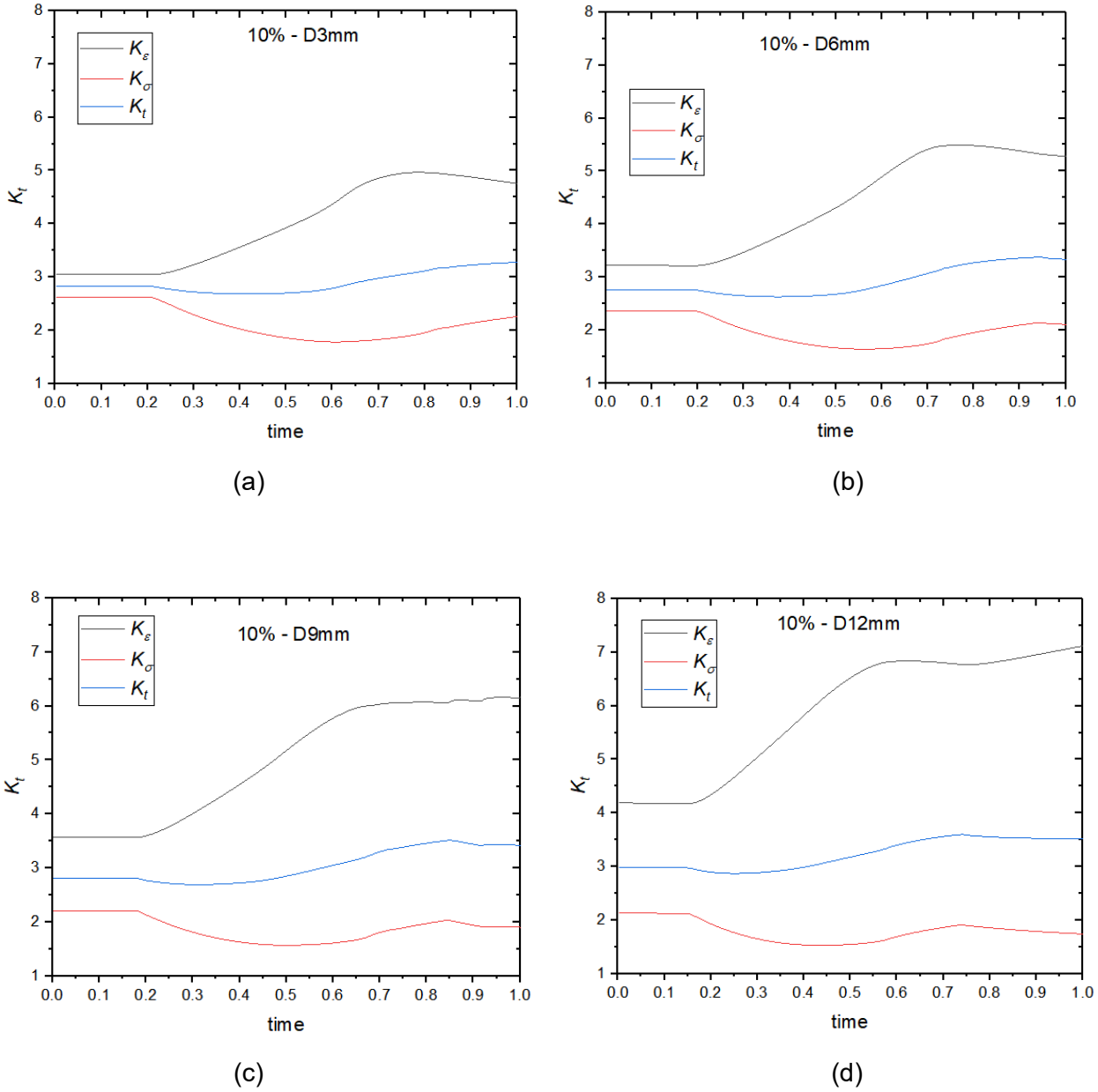


Figure 75 – Stress, strain and Neuber concentration factors for 10% training: a) D3 mm b) D6mm, c) D9mm, d) D12mm

6. CONCLUSION AND SUGGESTIONS FOR FUTURE WORKS

6.1. Conclusion

This thesis investigated, in a comprehensive manner, the effects of thermal treatment, mechanical training, and geometric discontinuities on the pseudoelastic behavior of thin shape memory alloy sheets. A combination of experimental techniques, including digital image correlation (DIC) and infrared thermography, with finite element method (FEM) numerical modeling based on advanced constitutive laws that incorporate stress-induced martensitic transformation and plasticity, enabled an assessment of the mechanisms governing energy dissipation, stress redistribution, and concentration phenomena under complex loading conditions.

The results demonstrated that thermal treatment and mechanical history have an important role in defining the critical transformation stresses and temperatures and the overall functional performance of pseudoelastic SMAs. In particular, differential scanning calorimetry revealed that short-duration heat treatments at 530 °C preserved the R-phase and led to the lowest austenite finish temperature, establishing favorable conditions for pseudoelasticity. Mechanical testing further showed that the maximum energy dissipation (5.8 MJ/m³), was achieved under the 530°C/10 min treatment combined with 6.5% training strain, confirming the possibility of optimizing thermomechanical performance by fine-tuning processing parameters.

The investigation of plates with holes has contributed to clarify the intricate role of geometric discontinuities in promoting local stress and strain fields. Experimental measurements highlighted strain localization and temperature evolution around holes due to the thermomechanical coupling associated to the exothermic/endothermic nature of phase transformation. The numerical results obtained were compared with experimental results, showing that the proposed model based on the finite element method was able to capture these location effects with good accuracy.

Regarding the different methodologies adopted, the stress concentration is one of interest. K_σ values exhibited a non-trivial evolution with four stages: 1) initially presents a value close to the classical elastic solution; 2) it decreases upon the onset of phase transformation due to stress redistribution; 3) increases again as larger regions underwent martensitic transformation; and 4) subsequently decreased once plasticity initiated. These findings confirm the strong interplay

between microstructural transformation mechanisms and macroscopic stress fields in SMA components with notches.

From a mechanical design perspective, the Neuber criterion is shown to be an appropriate and robust approach for the class of pseudoelastic SMA structures investigated in this thesis. By providing an intermediate estimate between the stress- and strain-based concentration factors (K_σ and K_ε), it captures the essential redistribution mechanisms associated with inelastic deformation and phase transformation. This finding is fully consistent with Neuber's original formulation (Neuber, 1961) and supports its extension to the design of SMA components containing geometric discontinuities.

The analysis of different hole diameters and training histories further emphasized the coupling between geometry, material history, and concentration effects. Larger holes promoted broader transformed regions and stronger heterogeneity in the stress field, while training history significantly influenced the stabilized response. Notably, the 6.5% training condition consistently resulted in lower final values of K_σ compared to the 10% condition, with reductions of up to 12.4% depending on the hole size. This observation highlights the practical relevance of improving training protocols to mitigate stress concentration and enhance structural reliability.

Finally, the methodological contributions of this work are equally significant. The integration of full-field experimental methods with advanced numerical modeling proved to be a powerful approach to characterize and predict the complex interplay of elasticity, phase transformation, and plasticity in pseudoelastic materials.

In summary, this dissertation proposed a robust experimental–numerical framework to analyze the pseudoelastic response of SMAs in the presence of stress concentrators and cyclic loading. The findings confirm that the mechanical behavior of these materials cannot be understood within the limits of classical elasticity and plasticity but require explicit consideration of phase transformation phenomena and their interactions with plastic strain. By advancing both the scientific understanding and the methodological tools available for the analysis of SMA components, this work provides a solid foundation for the safe and efficient design of energy-dissipative, actuation, and biomedical systems where reliability under cyclic conditions is critical.

6.2. Suggestions for future works

While this work has advanced the understanding of pseudoelastic response, stress concentration, and processing effects in thin SMA sheets, several open questions remain that provide opportunities for further research. A natural continuation of this work lies in the detailed microstructural characterization of transformation zones and plasticity-affected regions. Advanced techniques such as high-energy X-ray diffraction, transmission electron microscopy, and synchrotron-based tomography could be employed to directly correlate microstructural evolution with the experimentally observed strain fields. Such analyses would clarify the role of twin reorientation, defect accumulation, and local phase stability in governing stress redistribution around notches and discontinuities. Also, it is important to expand the experimental program to study the experimental dispersion of the results.

Another promising direction concerns the systematic investigation of fatigue under cyclic thermomechanical loading. The current work focused primarily on monotonic pseudoelastic behavior, yet the long-term reliability of SMA components in engineering applications is ultimately dictated by their fatigue resistance. Future studies should combine full-field experimental methods with multiscale modeling to capture the initiation and propagation of fatigue damage under realistic service conditions, including variable amplitude loading and coupled thermomechanical cycling. This would enable the establishment of fatigue life prediction models that explicitly account for transformation-induced plasticity and local stress concentrations.

The integration of fracture mechanics into the framework developed here remains a critical challenge. While this thesis demonstrated the strong effect of stress concentrators on phase transformation and stress redistribution, the progression from localized transformation to crack initiation and propagation has not been fully addressed. Future research should therefore investigate fracture processes in pseudoelastic SMAs using a combination of experimental methods, such as digital image correlation and infrared thermography, with fracture-based finite element formulations, including virtual crack closure techniques and strain energy density criteria. Such studies would allow for the development of design methodologies capable of predicting not only the onset of damage but also the evolution of cracks under coupled thermomechanical loading, thereby bridging the gap between material science and structural integrity in SMA-based systems.

The influence of thermomechanical coupling associated with the endothermic/exothermic nature of the phase transformation process in SMAs on the behavior of mechanical components

with stress concentrations is an important topic whose modeling presents several challenges due to the coupling of mechanical, thermal and phase transformation phenomena.

Additive manufacturing is a rapidly growing and highly important field for the manufacture of SMA mechanical components. The complex behavior of these alloys depends heavily on the manufacturing processes, especially the stages involving mechanical forming and heat treatments. Therefore, research into stress concentration in parts produced by this process is of great relevance.

Finally, it is important to extend the proposed methodology to the analysis of the shape memory effect in SMA materials subjected to thermomechanical loading cycles.

REFERENCES

ABAQUS. Abaqus user manuals. Version 2018.

ABOUTALEBI, M. R.; KARIMZADEH, M.; SALEHI, M. T.; ABBASI, S. M.; MORAKABATI, M. Influences of aging and thermomechanical treatments on the martensitic transformation and superelasticity of highly Ni-rich Ti-51.5 at.% Ni shape memory alloy. Thermochimica Acta, 2015. https://doi.org/10.1016/j.tca.2015.08.004.

ADEODATO, A.; VIGNOLI, L. L.; PAIVA, A.; MONTEIRO, L. L. S.; PACHECO, P. M. C. L.; SAVI, M. A. A shape memory alloy constitutive model with polynomial phase transformation kinetics. Shape Memory and Superelasticity, 2022. https://doi.org/10.1007/s40830-022-00382-1.

ADEODATO, A., VIGNOLI, L. L., SAVI, M. A., MONTEIRO, L. L. S. Adaptive piezoelectric energy harvester using a shape memory alloy stopper. Nonlinear Dynamics, 2025. https://doi.org/10.1007/s11071-025-11116-0

AHMAD, H.; HASHMI, A. W.; SINGH, J.; ARORA, K.; TIAN, Y.; IQBAL, F.; AL-DOSSARI, M.; KHAN, M. I. Innovations in additive manufacturing of shape memory alloys: Alloys, microstructures, treatments, applications. Journal of Materials Research and Technology, 2024. https://doi.org/10.1016/j.jmrt.2024.08.213

AHMED, A.; PRANTO, S. I.; FARUQ, M. H. A.; KASFIA, T. T.; RASHID, A. B. A comprehensive overview of shape memory alloys: Recent advances in fabrications, properties, and applications for next-generation smart systems. Next Materials, 2026. https://doi.org/10.1016/j.nxmate.2025.101441

ALSAWALHI, M. Y., LANDIS, C. M. On the fracture toughness of shape memory alloys. International Journal of Fracture, 2022. https://doi.org/10.1007/s10704-022-00648-w

ALTAS, E.; KHOSRAVI, F.; GOKKAYA, H.; ARAB MALEKI, V.; AKINAY, Y.; OZDEMIR, O.; BAYRAKTAR, O.; KANDAS, H. Finite element simulation and experimental investigation on the effect of temperature on pseudoelastic behavior of perforated Ni–Ti shape memory alloy strips. Smart Materials and Structures, 2022. https://doi.org/10.1088/1361-665X/ac4691

AMERICAN SOCIETY FOR TESTING AND MATERIALS. Standard test methods for tension testing of metallic materials. ASTM E8. West Conshohocken, PA: ASTM International, 2007.

AMERICAN SOCIETY FOR TESTING AND MATERIALS. Standard test method for tension testing of nickel-titanium superelastic materials. ASTM F2516. West Conshohocken, PA: ASTM International, 2022.

AMMAR, O.; HADDAR, N.; DIENG, L. Experimental investigation of the pseudoelastic behaviour of NiTi wires under strain- and stress-controlled cyclic tensile loadings. Intermetallics, 2017. https://doi.org/10.1016/j.intermet.2017.03.002.

ARGÔLO, A. L. L. Análise da influência do tratamento térmico no comportamento de molas helicoidais de liga com memória de forma. 2023. Dissertation (Mestrado em Engenharia Mecânica e Tecnologia dos Materiais) – Centro Federal de Educação Tecnológica Celso Suckow da Fonseca (CEFET/RJ), Rio de Janeiro, 2023 (*in Portuguese*).

ARMATTOE , K.M. Modélisation non-locale du comportement thermomécanique d'Alliages à Méemoire de Forme (AMF) avec prise en compte de la localisation et des effets de la chaleur latente lors de la transformation de phase : Application aux structures minces en AMF, Doctoral thesis – l'Université de Lorraine, Lorraine, 2014 (*in French*).

AURICCHIO, F.; TAYLOR, R. L. Shape-memory alloys: modeling and numerical simulations of the finite-strain pseudoelastic behavior. Computer Methods in Applied Mechanics and Engineering, 1997. https://doi.org/10.1016/S0045-7825(96)01147-4.

AURICCHIO, F., TAYLOR, R. L., LUBLINER J., "Shape-Memory Alloys: Macromodelling and Numerical Simulations of the Superelastic Behavior, Computer Methods in Applied Mechanics and Engineering, 1997. https://doi.org/10.1016/S0045-7825(96)01232-7

BÁRNIK, F.; SÁGA, M.; VAŠKO, M.; HANDRIK, M.; KOPAS, P.; ŠTALMACH, O.; DORČIAK, F. Measurement and comparison study of deformation using extensometer and 2D DIC technology. IOP Conference Series: Materials Science and Engineering, 2020. DOI: 10.1088/1757-899X/776/1/012065

BAXEVANIS, T.; LAGOUDAS, D. C. Fracture mechanics of shape memory alloys: review and perspectives. International Journal of Fracture. 2015. https://doi.org/10.1007/s10704-015-9999-z

BEN FRAJ, B.; ZGHAL, S. Correlation between hardness behavior, shape memory, and superelasticity in Ni-rich NiTi shape memory alloy. Journal of Materials Engineering and Performance, 2025. https://doi.org/10.1007/s11665-024-09313-w.

CASTRO, J. T. P.; MEGGIOLARO, M. A. Fatigue: techniques and sizing practices under actual service loads. Charleston: CreateSpace Independent Publishing Platform, 2009.

CATOOR, D.; MA, Z.; KUMAR, S. Cyclic response and fatigue failure of Nitinol under tension–tension loading. Journal of Materials Research, 2019. https://doi.org/10.1557/jmr.2019.254

CHEN, Q., KALPOE, T., JOVANOVA, J. Design of mechanically intelligent structures: Review of modelling stimuli-responsive materials for adaptive structures, Heliyon, 2024. https://doi.org/10.1016/j.heliyon.2024.e34026

CHEN, W.; XI, R.; JIANG, H.; LI, X.; DONG, G.; WANG, X. Superelasticity of geometrically graded NiTi shape memory alloys. Metals, 2023. https://doi.org/10.3390/met13091518.

CISSÉ, C.; ZAKI, W.; BEN ZINEB, T. A review of modeling techniques for advanced effects in shape memory alloy behavior. Smart Materials and Structures, 2016. https://doi.org/10.1088/0964-1726/25/10/103001.

CONGARD, Y., SAINT-SULPICE, L., PINO, L., BARATI, M. MORDENIZ, J., ARBAB CHIRANI, S., CALLOCH, S. Low cycle fatigue lifetime prediction of superplastic shape memory alloy structures: Application to endodontic instruments. Journal of the Mechanical Behavior of Biomedical Materials, 2023. https://doi.org/10.1016/j.jmbbm.2023.106122.

DELPUEYO, D.; JURY, A.; BALANDRAUD, X.; GRÉDIAC, M. Applying full-field measurement techniques for the thermomechanical characterization of shape memory alloys: a review and classification. Shape Memory and Superelasticity, 2021. https://doi.org/10.1007/s40830-021-00355-w.

DI LEONARDO, S.; PITARRESI, G.; BURRIESCI, G. Standard mechanical testing is inadequate for the mechanical characterization of shape-memory alloys: source of errors and a new corrective approach. Materials & Design, 2022. https://doi.org/10.1016/j.matdes.2022.110538.

DORNELAS, V. M. Modelagem constitutiva da fadiga em ligas com memória de forma D. Sc. Thesis, COPPE/UFRJ - Department of Mechanical Engineering. Rio de Janeiro, 2020. (in Portuguese).

DORNELAS, V. M.; DE OLIVEIRA, S. A.; SAVI, M. A. A macroscopic description of shape memory alloy functional fatigue. International Journal of Mechanical Sciences, 2020. https://doi.org/10.1016/j.ijmecsci.2019.105345

DORNELAS, V. M.; OLIVEIRA, S. A.; SAVI, M. A.; PACHECO, P. M. C. L. Numerical investigations of shape memory alloy fatigue. Metals, 2021a. https://doi.org/10.3390/met11101558.

DORNELAS, V. M.; DE OLIVEIRA, S. A.; SAVI, M. A.; PACHECO, P. M. C. L.; SOUZA, L. F. G. Fatigue on shape memory alloys: experimental observations and constitutive modeling. International Journal of Solids and Structures, 2021b. https://doi.org/10.1016/j.ijsolstr.2020.11.023

DOYLE, J. F., Modern experimental stress analysis, John Wiley & Sons, 2004

DUARTE, Brenno Tavares. Fabricação e caracterização de molas helicoidais de ligas com memória de forma. 2019. Dissertação (Mestrado em Engenharia Mecânica e Tecnologia dos Materiais) – Centro Federal de Educação Tecnológica Celso Suckow da Fonseca (CEFET/RJ), Rio de Janeiro, 2019 (*in Portuguese*).

FAN, Q. C.; ZHANG, Y. H.; WANG, Y. Y.; SUN, M. Y.; MENG, Y. T.; HUANG, S. K.; WEN, Y. H. Influences of transformation behavior and precipitates on the deformation behavior of Ni-rich NiTi alloys. Materials Science and Engineering: A, 2017. https://doi.org/10.1016/j.msea.2017.05.107.

FU, G.; LIU, X.; YI, X.; ZHANG, S.; CAO, X.; MENG, X.; GAO, Z.; WANG, H. Development of high-entropy shape-memory alloys: a review. Metals, 2023. https://doi.org/10.3390/met13071279.

GOLASIŃSKI, K. M.; MAJ, M.; PIECZYŃSKA, E. A.; TASAKI, W.; KIM, H. Y. Full-field deformation study of Ti–25Nb, Ti–25Nb–0.3O and Ti–25Nb–0.7O shape memory alloys during tension using digital image correlation. Metallurgical and Materials Transactions A, 2024. https://doi.org/10.1007/s11661-024-07414-8

GONZÁLES, G. L. G.; Medição de deformações elastoplásticas em regiões de concentração de tensões utilizando métodos sem malha e visão computacional. D. Sc. Thesis, PUC-Rio. Rio de Janeiro, 2014. (*in portuguese*)

GONZÁLES, G. L.; RODRIGUES, L. D.; FREIRE, J. L. Accurate Measurements of High Strain Gradients near Notches Using a Feature-Based DIC Algorithm. Journal of Mechanics Engineering and Automation, 2017. Doi: 10.17265/2159-5275/2017.01.004.C

GONZÁLEZ-SANZ, G.; GALÉ-LAMUELA, D.; ESCOLANO-MARGARIT, D.; BENAVENT-CLIMENT, A. Hysteretic behavior and ultimate energy dissipation capacity of large diameter bars made of shape memory alloys under seismic loadings. Metals, 2019. https://doi.org/10.3390/met9101099.

GU, X.; CAO, Y.; ZHU, J.; WANG, J.; ZHANG, W.; MOUMNI, Z. Shape optimization of SMA structures with respect to fatigue. Materials & Design, 2020. https://doi.org/10.1016/j.matdes.2019.108456.

HARTL, D. J.; LAGOUDAS, D C. Modeling of Stress Concentrations in SMA Components Considering Plastic and Viscoplastic Yielding. Structures, Structural Dynamics, and Materials Conference 2009.

HASAN, M. M.; BAXEVANIS, T. Actuation fatigue life prediction of notched shape memory alloy members. Journal of Applied Mechanics, 2019. https://doi.org/10.1115/1.4042994.

HASTUTI, K.; HAMZAH, E.; HASHIM, J. Effect of ageing temperatures on the transformation behaviour of Ti-50.7 at.% Ni shape memory alloy. Advanced Materials Research, 2014. https://doi.org/10.4028/www.scientific.net/AMR.845.108.

HE, Y. J. Interface propagation and energy dissipation in shape memory alloys. Scripta Materialia, 2023. https://doi.org/10.1016/j.scriptamat.2023.115420.

HIJAZI, J., KÄHLER, C. J. Influence of system components on the measurement uncertainty in two-dimensional digital image correlation. Journal of Testing and Evaluation. 2017. https://doi.org/10.1520/JTE20150437

HONG, H.; GENCTURK, B.; SAIIDI, M. S. Superelastic behavior of novel Ni–Ti–Co shape memory alloys for seismic applications. Smart Materials and Structures, 2024. https://dx.doi.org/10.1088/1361-665X/ad9369.

HOSSEINI, S. M.; ASHRAFI, M. J. Stress concentration in shape memory alloy sheets with circular cavities: effects of transformation, saturation, and plasticity. Journal of Strain Analysis for Engineering Design, 2023. https://doi.org/10.1177/03093247221113755.

International Digital Image Correlation Society (iDICs). (2018). Good Practices Guide for Digital Image Correlation. iDICs. https://doi.org/10.32720/idics/gpg.ed1

KANG, G.; KAN, Q.; YU, C.; SONG, D.; LIU, Y. Whole-life transformation ratchetting and fatigue of super-elastic NiTi alloy under uniaxial stress-controlled cyclic loading. Materials Science and Engineering: A, 2012. https://doi.org/10.1016/j.msea.2011.12.071.

JADHAV, M. R.; SINGH, S.; JOHN, P.; BHARGAW, H. N.; RAJAK, D. K. Advancements and recent trends in shape memory alloy actuators: position control and emerging applications. International Journal of Dynamics and Control, 2025. https://doi.org/10.1007/s40435-025-01615-8.

KAYA, I.; KARACA, H. E.; NAGASAKO, M; KAINUMA, R. Effects of aging temperature and aging time on the mechanism of martensitic transformation in nickel-rich NiTi shape memory alloys. Materials Characterization, 2020. https://doi.org/10.1016/j.matchar.2019.110034.

KANG, G., KAN, Q., YU, C., SONG, D., LIU, Y. Whole-life transformation ratchetting and fatigue of super-elastic NiTi Alloy under uniaxial stress-controlled cyclic loading, Materials Science and Engineering: A, 2012, https://doi.org/10.1016/j.msea.2011.12.071.

KARAKOC, O.; YEGIN, Y.; OZDOGAN, M.; SALMAN, M.; NAGABANDI, N.; YEGIN, C.; YURUKCU, Mesut; SARI, Mufrettin Murat. Chapter One - Smart and state-of-the-art materials in oil and gas industry. In: Advanced Materials and Sensors for the Oil and Gas Industry. Sustainable Materials for Transitional and Alternative Energy. Gulf Professional Publishing, 2021. https://doi.org/10.1016/B978-0-12-824379-4.00005-7

KONG, X.; ZHANG, J.; DING, H.; LIU, Q.; ZHOU, J.; QI, F.; WANG, P. Combined effect of annealing temperature and pre-deformation on the pseudoelastic behaviors of NiTi shape memory alloys. Journal of Materials Engineering and Performance, 2024. https://doi.org/10.1007/s11665-024-10077-6.

KUNDU, A.; BANERJEE, A. Coupled thermomechanical modelling of shape memory alloy structures undergoing large deformation. International Journal of Mechanical Sciences, 2022. https://doi.org/10.1016/j.ijmecsci.2022.107102

LAGOUDAS, D. C. Shape memory alloys: modeling and engineering applications. New York: Springer, 2008.

LEMAITRE, J., CHABOCHE, J. L., Mechanics of Solid Materials, Cambridge University Press, Cambridge, England, 1990.

LECCE, L. Shape memory alloy engineering for aerospace, structural and biomedical applications. Oxford: Elsevier, 2015.

LI, Y.; SHARIAT, B. S.; YANG, H.; LIU, Y. Influences of extrinsic factors on the Lüders-type deformation behaviour of NiTi. Materials Science and Engineering: A, 2023a. https://doi.org/10.1016/j.msea.2022.144418.

LI, Y.; SHARIAT, B. S.; YANG, H.; SARKAR, S.; ZHANG, J.; WANG, Y.; FAVIER, D.; LIU, Y. A mechanical criterion for Lüders-type deformation of polycrystalline NiTi. Acta Materialia, 2023b. https://doi.org/10.1016/j.actamat.2022.118604.

LOUCHE, H., SCHLOSSER, P., FAVIER, D., ORGÉAS, L. Heat Source Processing for Localized Deformation with Non-Constant Thermal Conductivity. Application to Superelastic Tensile Tests of NiTi Shape Memory Alloys, Experimental Mechanics, 2012. https://doi.org/10.1007/s11340-012-9607-3

MATUSZEWSKI, L. Application of Shape Memory Alloys in Pipeline Couplings for Shipbuilding. Polish Maritime Research, 2020. https://doi.org/10.2478/pomr-2020-0049

MEGGIOLARO, M. A.; CASTRO, J. T. P.; GÓES, R. C. O. Elastoplastic nominal stress effects in the estimation of the notch-tip behavior in tension. Theoretical and Applied Fracture Mechanics, 2016. https://doi.org/10.1016/j.tafmec.2016.03.004

MIYAZAKI, S., OTSUKA, K. SUZUKI, Y. Transformation pseudoelasticity and deformation behavior in a Ti-50.6at%Ni alloy, Scripta Metallurgica, 1981. https://doi.org/10.1016/0036-9748(81)90346-X.

MOHD JANI, J.; LEARY, M.; SUBIC, A.; GIBSON, M. A. A review of shape-memory alloy research, applications and opportunities. Materials & Design, 2014. https://doi.org/10.1016/j.matdes.2013.11.084

MOHAMMADGHOLIPOUR, A.; BILLAH, A. M. Mechanical properties and constitutive models of shape memory alloy for structural engineering: a review. Journal of Intelligent Material Systems and Structures, 2023. https://doi.org/10.1177/1045389X231185458.

MONTEIRO P. C. C., SAVI, M. A., NETTO, T. A., Pacheco P. M. C. L. A Phenomenological Description of the Thermomechanical Coupling and the Rate-dependent Behavior of Shape Memory Alloys. Journal of Intelligent Material Systems and Structures. 2009. https://doi.org/10.1177/1045389X09341199

MOTZKI, P., SEELECKE, S., Industrial Applications for Shape Memory Alloys, Encyclopedia of Smart Materials, 2019. DOI: 10.1016/B978-0-12-803581-8.11723-0

MURASAWA, G.; YONEYAMA, S.; MIYATA, K.; NISHIOKA, A.; KODA, T. Finite element analysis and experimental measurement of deformation behavior for NiTi plate with stress concentration part under uniaxial tensile loading. Strain, 2011. https://doi.org/10.1111/j.1475-1305.2009.00698.x.

NARGATTI K., AHANKARI S. Advances in enhancing structural and functional fatigue resistance of superelastic NiTi shape memory alloy: A Review. Journal of Intelligent Material Systems and Structures. 2021. doi:10.1177/1045389X211023582

NEUBER, H. Theory of stress concentration for shear-strained prismatical bodies with arbitrary nonlinear stress-strain law. Journal of Applied Mechanics, 1961.

OLIVEIRA, H. S.; DE PAULA, A. S. The influence of hysteresis loop in a NiTi shape memory oscillator behavior. Smart Materials and Structures, 2020. https://doi.org/10.1088/1361-665X/abb070.

OLIVEIRA, S. A.; DORNELAS, V. M.; SAVI, M. A.; PACHECO, P. M. C. L.; PAIVA, A. A phenomenological description of shape memory alloy transformation-induced plasticity. Meccanica, 2018. https://doi.org/10.1007/s11012-018-0836-0.

OLIVEIRA, S. A.; SAVI, M. A.; ZOUAIN, N. A three-dimensional description of shape memory alloy thermomechanical behavior including plasticity. Journal of the Brazilian Society of Mechanical Sciences and Engineering, 2016. https://doi.org/10.1007/s40430-015-0476-4

OTSUKA, K.; WAYMAN, C. M. Shape Memory Materials. Cambridge University Press, 1998.

PAIVA, V. E. L., Modern experimental techniques with an emphasis on infrared thermography to the assessment of fatigue components with dents. Doctoral thesis – Pontifical Catholic University of Rio de Janeiro, Rio de Janeiro, 2020.

PANDOLFI, G. S.; MARTINS, S. C.; BUONO, V. T. L.; SANTOS, L. A. Precipitation kinetics of Ti3Ni4 and multistage martensitic transformation in an aged Ni-rich Ni-Ti shape memory alloy. Journal of Materials Research and Technology, 2020. https://doi.org/10.1016/j.jmrt.2020.06.046.

PATIL, D., SONG, G., a review of shape memory material's applications in the offshore oil and gas industry, Smart Materials and Structures, 2017. DOI 10.1088/1361-665X/aa7706

PAUL, P. P., PARANJAPE, H. M., AMIN-AHMADI, P., PAGAN, D. C., CHUMLYAKOV, Y. I., BRINSON, C. Heterogeneity and inelasticity of deformation in a notched martensitic NiTi shape memory alloy specimen. Acta Materialia, 2020. https://doi.org/10.1016/j.actamat.2020.05.019

PÉREZ, J. A., COPPIETERS, S., DEBRUYNE. D. Influence of the paint coating thickness in digital image correlation experiments. International Journal of Computer, Electrical, Automation, Control and Information Engineering, 2015.

PHILLIPS, F.R. Effect of Phase Transformation on Stress Redistribution and Damage Evolution During Actuation Fatigue in Shape Memory Alloys. PhD Dissertation, Texas A & M University. 2018.

PHILLIPS, F. R.; WHEELER, R. W.; GELTMACHER, A. B.; LAGOUDAS, D. C. Evolution of internal damage during actuation fatigue in shape memory alloys. International Journal of Fatigue, 2019. https://doi.org/10.1016/j.ijfatigue.2018.12.019.

PIECZYSKA, E. A.; TOBUSHI, H.; TAKEDA, K.; STRÓŻ, D.; RANACHOWSKI, Z.; KULASIŃSKI, K.; KÚDELA Jr., S.; LUCKNER, J. Martensite transformation bands studied in TiNi shape memory alloy by infrared and acoustic emission techniques. Kovove Mater., 2012. DOI: 10.4149/km_2012_5_309

PILKEY, W. D. Peterson's stress concentration factors. New York: John Wiley & Sons, 1997.

RAMOS, A. D.O., ARAÚJO, C. J., OLIVEIRA, H. M. R.; MACÊDO, G. A.; LIMA, A. G. B. An experimental investigation of the superelastic fatigue of NiTi SMA wires. Journal of the Brazilian Society of Mechanical Sciences and Engineering, 2018. DOI: 10.1007/s40430-018-1101-0

RANGASWAMY, S.; CHEKOTU, J. C.; GILLICK, T.; HUGHES, C.; NICHOLL, J.; EASTON, D.; ŞİMŞİR, C.; BRABAZON, D. Evaluating residual stress in additively manufactured nitinol shape memory alloy. npj Advanced Manufacturing, 2025. https://doi.org/10.1038/s44334-025-00027-y

REZAEE-HAJIDEHI, M., NEGHABI, M., STUPKIEWICZ, S. A Note on Thermomechanical Coupling Effects in the Indentation of Pseudoelastic Shape Memory Alloys. Shape Memory and Superelasticity, 2025. https://doi.org/10.1007/s40830-025-00569-2

ROMANOWICZ, P.J.; SZYBIŃSKI, B.; WYGODA, M. Application of DIC Method in the Analysis of Stress Concentration and Plastic Zone Development Problems. Materials, 2020. https://doi.org/10.3390/ma13163460

SGAMBITTERRA, E.; MAGARÒ, P.; NICCOLI, F.; FURGIUELE, F.; MALETTA, C. Fatigue crack growth in austenitic and martensitic NiTi: modeling and experiments. Shape Memory and Superelasticity, 2021. https://doi.org/10.1007/s40830-021-00327-0.

SHARIAT, B. S.; BAKHTIARI, S.; YANG, H.; LIU, Y. Computational and experimental analyses of martensitic transformation propagation in shape memory alloys. Journal of Alloys and Compounds, 2019. https://doi.org/10.1016/j.jallcom.2019.06.139.

SHARIAT, B. S.; LI, Y.; YANG, H.; WANG, Y.; LIU, Y. *On the Lüders band formation and propagation in NiTi shape memory alloys.* Journal of Materials Science & Technology, 2022. https://doi.org/10.1016/j.jmst.2021.11.028

SHARIAT, B. S.; LIU, Y. Variation of Poisson's ratio of NiTi during pseudoelastic deformation. Shape Memory and Superelasticity, 2023. https://doi.org/10.1007/s40830-023-00464-8.

SHARIAT, B. S.; LIU, Y.; RIO, G. Finite element computational modelling and experimental investigation of perforated NiTi plates under tension. Materials Research Bulletin, 2013. https://doi.org/10.1016/j.materresbull.2013.05.022

SHARIAT, B. S.; LIU, Y.; RIO, G. Numerical modelling of pseudoelastic behaviour of NiTi porous plates. Journal of Intelligent Material Systems and Structures, 2014a. https://doi.org/10.1177/1045389X13505783.

SHARIAT B S., LIU Y., RIO G. Pseudoelastic behaviour of perforated NiTi shape memory plates under tension Intermetallics, 2014b. https://doi.org/10.1016/j.intermet.2014.02.016

SHAW, J.A., CHURCHILL, C.B. AND IADICOLA, M.A. Tips and tricks for characterizing shape memory alloy wire: part 1—differential scanning calorimetry and basic phenomena. Experimental Techniques, 2008. https://doi.org/10.1111/j.1747-1567.2008.00410.x.

SHAYANFARD, P., ALARCON, E., BARATI, M., MAHTABI, M. J., KADKHODAEI, M., ARBAB CHIRANI, S., ŠANDERA, P. Stress raisers and fracture in shape memory alloys: review and ongoing challenges. Critical Reviews in Solid State and Materials Sciences, 2021a. https://doi.org/10.1080/10408436.2021.1896475

SHAYANFARD, P.; HELLER, L.; ŠANDERA, P.; ŠITTNER, P. Experimental and numerical investigation of thermomechanical cycling of notched NiTi shape memory ribbon using SMA model accounting for plastic deformation. Journal of Materials Research and Technology, 2021b. https://doi.org/10.1016/j.jmrt.2021.08.132.

SILVA, B. F.; SOUZA, L. F. G.; AGUIAR, R. A. A.; PACHECO, P. M. C. L. Analysis of stress concentration in pseudoelastic thin sheets using the finite element method. In: COBEM 2023. Proceedings…, 2023. DOI: 10.26678/ABCM.COBEM2023.COB2023-0759.

SILVA, B. F.; SOUZA, L. F. G.; AGUIAR, R. A. A.; PACHECO, P. M. C. L. Análise por elementos finitos do fator de concentração de tensão em uma chapa fina pseudoelástica com transformação

de fase e plasticidade. In: CONEM 2024a. Anais…, 2024a. (*in Portuguese*). DOI: 10.26678/ABCM.CONEM2024.CON24-1178.

SILVA, B. F.; SOUZA, L. F. G.; AGUIAR, R. A. A.; PACHECO, P. M. C. L. Analysis of stress concentration in pseudoelastic plates using digital image correlation (DIC) and finite element method. In: MECSOL 2024. Proceedings…, 2024b. DOI:10.26678/ABCM.MECSOL2024.MSL24-0101.

SILVA, B. F.; SOUZA, L. F. G.; AGUIAR, R. A. A.; PACHECO, P. M. C. L. Analysis of stress concentration in pseudoelastic thin sheets using the finite element method. Journal of the Brazilian Society of Mechanical Sciences and Engineering, 2025a. https://doi.org/10.1007/s40430-025-05715-6

SILVA, B. F.; SOUZA, L. F. G.; AGUIAR, R. A. A.; PACHECO, P. M. C. L. Analysis of stress concentration in pseudoelastic plates using digital image correlation (DIC) and finite element method. Latin American Journal of Solids and Structures, 2025b. https://doi.org/10.1590/1679-7825/e8703

SILVA, J. D.; MARTINS, S. C.; LOPES, N. I. A.; RESENDE, P. D.; SANTOS, L. A.; BUONO, V. T. L. Effects of aging treatments on the fatigue resistance of superelastic NiTi wires. Materials Science and Engineering: A, 2019. https://doi.org/10.1016/j.msea.2019.04.037.

SIMOES, M.; MARTÍNEZ-PAÑEDA, E. Phase field modelling of fracture and fatigue in shape memory alloys. Computer Methods in Applied Mechanics and Engineering, 2021. https://doi.org/10.1016/j.cma.2020.113504.

SITTNER, P., LIU, Y., NOVAK, V. On the origin of Lüders-like deformation of NiTi shape memory alloys, Journal of the Mechanics and Physics of Solids, 2005. https://doi.org/10.1016/j.jmps.2005.03.005.

SONG, D.; KANG, G.; KAN, Q.; YU, C.; ZHANG, C. The effect of martensite plasticity on the cyclic deformation of super-elastic NiTi shape memory alloy. Smart Materials and Structures, 2013. https://doi.org/10.1088/0964-1726/23/1/015008.

SUTTON, M. A., ORTEU, J. J., SCHREIER, H. W. Image Correlation for Shape, Motion and Deformation Measurements: Basic Concepts, Theory and Applications. Springer. 2009. https://doi.org/10.1007/978-0-387-78747-3.

VOLLMER, M.; MÖLLMANN, K.-P. Infrared Thermal Imaging: Fundamentals, Research and Applications. Wiley-VCH, 2010.

XIAO Y., JIANG, D., Constitutive modelling of transformation pattern in superelastic NiTi shape memory alloy under cyclic loading, International Journal of Mechanical Sciences, 2020, https://doi.org/10.1016/j.ijmecsci.2020.105743.

XIAO, Y.; ZENG, P.; LEI, L. Effect of double-edge semi-circular notches on the mechanical response of superelastic NiTi shape memory alloy: experimental observations. Journal of Strain Analysis for Engineering Design, 2016. https://doi.org/10.1177/0309324716661460.

XU, L.; SOLOMOU, A.; BAXEVANIS, T.; LAGOUDAS, D. Finite Strain Constitutive Modeling For Shape Memory Alloys Considering Transformation-Induced Plasticity And Two-Way Shape Memory Effect. International Journal of Solids and Structures. 2021. https://doi.org/10.1016/j.ijsolstr.2020.03.009

YAMAZAKI, T.; MONTAGNOLI, A. L.; YOUNG, M. L.; TAKEUCHI, I. Tuning the temperature range of superelastic Ni-Ti alloys for elastocaloric cooling via thermal processing. Journal of Physics: Energy, 2023. https://doi.org/10.1088/2515-7655/accd21.

YILDIRIM, M., CANDAN, Z.; Smart materials: The next generation in science and engineering, Materials Today: Proceedings, 2023. https://doi.org/10.1016/j.matpr.2023.10.116.

YOU Y., WANG J., SU X., GUO X., MOUMNI Z., ZHANG W. 2020 Materials Today Communications https://doi.org/10.1016/j.mtcomm.2020.101137

ZHANG, X.L., WANG, S., JIANG, Y., HUANG, J., WANG, S.P., ZHANG, Q.Q, LI, Q., GUO, Y.Q.; ZHANG, Z.H. Influence of building directions on the impact properties of NiTi fabricated via laser powder bed fusion. 2024. Journal of Materials Research and Technology. https://doi.org/10.1016/j.jmrt.2023.12.160.

ZHANG, Y.; CHAI, X.; JU, X.; ZHU, J.; MOUMNI, Z.; ZHANG, W. The upper bound of low cycle fatigue life of pseudoelastic polycrystalline NiTi shape memory alloys. Smart Materials and Structures, 2022. https://doi.org/10.1088/1361-665X/ac8a2d.

ZHENG, Y.; JIANG, F.; LI, L.; YANG, H.; LIU, Y. Effect of ageing treatment on the transformation behaviour of Ti–50.9 at.% Ni alloy. Acta Materialia, 2008. https://doi.org/10.1016/j.actamat.2007.10.020.

ZHU, P.; STEBNER, A. P.; BRINSON, C. A numerical study of the coupling of elastic and transformation fields in pore arrays in shape memory alloy plates to advance porous structure design and optimization. Smart Materials and Structures, 2013. https://doi.org/10.1088/0964-1726/22/9/094009.

ZHU, P.; STEBNER, A. P.; BRINSON, C. Plastic and transformation interactions of pores in shape memory alloy plates. Smart Materials and Structures, 2014. https://doi.org/10.1088/0964-1726/23/10/104008.

ZITOUNI, I.; ABUZAID, W.; EGILMEZ, M.; ALKHADER, M. Experimental assessment of the functional fatigue in biocompatible Ti67Zr19Nb11.5Sn2.5 shape memory alloy in the vicinity of drilled holes. Journal of Materials Research and Technology, 2023. https://doi.org/10.1016/j.jmrt.2023.10.143.

APPENDIX 1 – LIST OF PUBLICATIONS

Academic journal papers

Silva B.F., Souza L.F.G., Aguiar, R.A.A., Pacheco P.M.C.L., Analysis of stress concentration in pseudoelastic thin sheets using the finite element method, Journal of the Brazilian Society of Mechanical Sciences and Engineering. 2025. *(https://doi.org/10.1007/s40430-025-05715-6*).

Silva B.F., Souza L.F.G., Aguiar, R.A.A., Pacheco P.M.C.L., Analysis of stress concentration in pseudoelastic plates using digital image correlation (DIC) and finite element method. Latin American Journal of Solids and Structures. *(https://doi.org/10.1590/1679-7825/e8703*).

Conference proceeding papers

Silva B. F., Souza L. F. G., Aguiar, R. A. A., Pacheco P. M. C.L., (2023) Analysis of stress concentration in pseudoelastic thin sheets using the finite element method, Proceedings COBEM 2023. DOI://10.26678/ABCM.COBEM2023.COB2023-0759

Silva B. F., Souza L. F. G., Aguiar R. A. A., Pacheco P. M. C. L., (2024) Análise por Elementos Finitos do Fator de Concentração de Tensão em uma Chapa Fina Pseudoelástica com Transformação de Fase e Plasticidade, Proceedings CONEM 2024, (*in Portuguese*). DOI://10.26678/ABCM.CONEM2024.CON24-1178.

Silva B. F., Souza L. F. G., Aguiar R. A. A., Pacheco P. M. C. L., (2024) Analysis of stress concentration in pseudoelastic plates using digital image correlation (DIC) and finite element method, Proceedings Mecsol 2024. DOI://10.26678/ABCM.MECSOL2024.MSL24-0101.

Silva B. F., Souza L. F. G., Aguiar R. A. A., Pacheco P. M. C. L. COB-2025-1437 - Stress concentration factors of pseudoelastic thin sheets with geometric discontinuities, Proceedings COBEM 2025

SILVA, B. F.; Souza, L. F. G., AGUIAR, R. A. A. ; PACHECO, P. M. C. L. Investigation of the influence training on the thermomechanical behavior of pseudoelastic NiTi thin plates using digital image correlation and thermography. *In*: XXII B-MRS Meeting, 2024.

SILVA, B. F.; Souza, L. F. G. ; AGUIAR, R. A. A. ; PACHECO, P. M. C. L. . Análise experimental do efeito de tratamentos térmicos no efeito de pseudoelasticidade em placas finas de liga com memória de forma. *In*: Congresso Brasileiro de Engenharia e Ciência dos Materiais (CBECiMat), 2024. (*in portuguese*).